Chaos Synchronization in Time-Delayed Coupled Networks

Dissertation zur Erlangung des
naturwissenschaftlichen Doktorgrades
der Bayerischen Julius-Maximilians-Universität Würzburg

vorgelegt von

Dipl.-Phys. Steffen Zeeb

aus Ulm

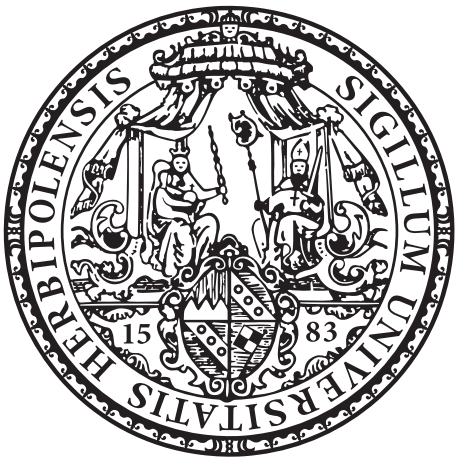

Würzburg 2013

Eingereicht am: 22.05.2013
bei der Fakultät für Physik und Astronomie

1. Gutachter: Prof. Dr. Wolfgang Kinzel
2. Gutachter: Prof. Dr. Björn Trauzettel
der Dissertation

1. Prüfer: Prof. Dr. Wolfgang Kinzel
2. Prüfer: Prof. Dr. Björn Trauzettel
3. Prüfer: Prof. Dr. Jean Geurts
im Promotionskolloquium

Tag des Promotionskolloquiums: 16.07.2013

Doktorurkunde ausgehändigt am:

Zusammenfassung

Die vorliegende Arbeit befasst sich mit der Untersuchung verschiedener Aspekte der Chaos Synchronisation von Netzwerken mit zeitverzögerten Kopplungen. Ein Netzwerk aus identischen chaotischen Einheiten kann vollständig und isochron synchronisieren, auch wenn der Signalaustausch einer starken Zeitverzögerung unterliegt.

Im ersten Teil der Arbeit werden Systeme mit mehreren Zeitverzögerungen betrachtet. Dabei erstrecken sich die verschiedenen Zeitverzögerungen jeweils über einen weiten Bereich an Größenordnungen. Es wird gezeigt, dass diese Zeitverzögerungen im Lyapunov Spektrum des Systems auftreten; verschiedene Teile des Spektrums skalieren jeweils mit einer der Zeitverzögerungen. Anhand des Skalierungsverhaltens des maximalen Lyapunov Exponenten können verschiedene Arten von Chaos definiert werden. Diese bestimmen die Synchronisationseigenschaften eines Netzwerkes und werden insbesondere wichtig bei hierarchischen Netzwerken, d.h. bei Netzwerken bestehend aus Unternetzwerken, bei welchen Signale innerhalb des Unternetzwerkes auf einer anderen Zeitskala ausgetauscht werden als zwischen verschiedenen Unternetzwerken. Für ein solches System kann sowohl vollständige als auch Unternetzwerksynchronisation auftreten. Skaliert der maximale Lyapunov Exponent mit der kürzeren Zeitverzögerung des Unternetzwerkes dann können nur die Elemente des Unternetzwerkes synchronisieren. Skaliert der maximale Lyapunov Exponent allerdings mit der längeren Zeitverzögerung kann das komplette Netzwerk vollständig synchronisieren. Dies wird analytisch für die Bernoulli Abbildung und numerisch für die Zelt Abbildung gezeigt.

Der zweite Teil befasst sich mit der Attraktordimension und ihrer Änderung am Übergang zur vollständiger Chaos Synchronisation. Aus dem Lyapunov Spektrum des Systems wird die Kaplan-Yorke Dimension berechnet und es wird gezeigt, dass diese am Synchronisationsübergang aus physikalischen Gründen einen Sprung haben muss. Aus der Zeitreihe der Dynamik des Systems wird die Korrelationsdimension bestimmt und anschließend mit der Kaplan-Yorke Dimension verglichen. Für Bernoulli Systeme finden wir in der Tat eine Diskontinuität in der Korrelationsdimension. Die Stärke des Sprungs der Kaplan-Yorke Dimension wird für ein Netzwerk aus Bernoulli Einheiten als Funktion der Netzwerkgröße berechnet. Desweiteren wird das Skalierungsverhalten der Kaplan-Yorke Dimension sowie der Kolmogoroventropie in Abhängigkeit der Systemgröße und der Zeitverzögerung untersucht. Zu guter Letzt wird eine Verstimmung der Einheiten, d.h., ein „parameter mismatch“, eingeführt und analysiert wie diese das Verhalten der Attraktordimension ändert.

Im dritten und letzten Teil wird die lineare Antwort eines synchronisierten chaotischen Systems auf eine kleine externe Störung untersucht. Diese Störung bewirkt eine Abweichung der Einheiten vom perfekt synchronisierten Zustand. Die Verteilung der Abstände zwischen zwei Einheiten dient als Maß für die lineare Antwort des Systems. Diese Verteilung sowie ihre Momente werden numerisch und für Spezialfälle auch analytisch berechnet. Wir finden, dass im synchronisierten Zustand, in Abhängigkeit der Parameter des Systems, Verteilungen auftreten können die einem Potenzgesetz gehorchen und dessen Momente divergieren. Als weiteres Maß für die lineare Antwort wird die Bit Error Rate einer übermittelten binären Nachricht verwendet. The Bit Error Rate ist durch ein Integral über die Verteilung der Abstände gegeben. In dieser Arbeit wird sie vorwiegend numerisch untersucht und wir finden ein komplexes, nicht monotones Verhalten als Funktion der Kopplungsstärke. Für Spezialfälle weist die Bit Error Rate eine „devil's staircase“ auf, welche mit einer fraktalen Struktur in der Verteilung der Abstände verknüpft ist. Die lineare Antwort des Systems auf eine harmonische Störung wird ebenfalls untersucht. Es treten Resonanzen auf, welche in Abhängigkeit von der Zeitverzögerung unterdrückt oder verstärkt werden. Eine bi-direktional gekoppelte Kette aus drei Einheiten kann eine Störung vollständig heraus filtern, so dass die Bit Error Rate und auch das zweite Moment verschwinden.

Abstract

In this thesis we study various aspects of chaos synchronization of time-delayed coupled chaotic maps. A network of identical nonlinear units interacting by time-delayed couplings can synchronize to a common chaotic trajectory. Even for large delay times the system can completely synchronize without any time shift.

In the first part we study chaotic systems with multiple time delays that range over several orders of magnitude. We show that these time scales emerge in the Lyapunov spectrum: Different parts of the spectrum scale with the different delays. We define various types of chaos depending on the scaling of the maximum exponent. The type of chaos determines the synchronization ability of coupled networks. This is, in particular, relevant for the synchronization properties of networks of networks where time delays within a subnetwork are shorter than the corresponding time delays between the different subnetworks. If the maximum Lyapunov exponent scales with the short intra-network delay, only the elements within a subnetwork can synchronize. If, however, the maximum Lyapunov exponent scales with the long inter-network connection, complete synchronization of all elements is possible. The results are illustrated analytically for Bernoulli maps and numerically for tent maps.

In the second part the attractor dimension at the transition to complete chaos synchronization is investigated. In particular, we determine the Kaplan-Yorke dimension from the spectrum of Lyapunov exponents for iterated maps. We argue that the Kaplan-Yorke dimension must be discontinuous at the transition and compare it to the correlation dimension. For a system of Bernoulli maps we indeed find a jump in the correlation dimension. The magnitude of the discontinuity in the Kaplan-Yorke dimension is calculated for networks of Bernoulli units as a function of the network size. Furthermore the scaling of the Kaplan-Yorke dimension as well as of the Kolmogorov entropy with system size and time delay is investigated. Finally, we study the change in the attractor dimension for systems with parameter mismatch.

In the third and last part the linear response of synchronized chaotic systems to small external perturbations is studied. The distribution of the distances from the synchronization manifold, i.e., the deviations between two synchronized chaotic units due to external perturbations on the transmitted signal, is used as a measure of the linear response. It is calculated numerically and, for some special cases, analytically. Depending on the model parameters this distribution has power law tails in the region of synchronization leading to diverging moments. The linear response is also

quantified by means of the bit error rate of a transmitted binary message which perturbs the synchronized system. The bit error rate is given by an integral over the distribution of distances and is studied numerically for Bernoulli, tent and logistic maps. It displays a complex nonmonotonic behavior in the region of synchronization. For special cases the distribution of distances has a fractal structure leading to a devil's staircase for the bit error rate as a function of coupling strength. The response to small harmonic perturbations shows resonances related to coupling and feedback delay times. A bi-directionally coupled chain of three units can completely filter out the perturbation. Thus the second moment and the bit error rate become zero.

Acknowledgements

First of all, I would like to thank my supervisor Prof. Dr. Wolfgang Kinzel very much for accepting me as his PhD-student and giving me the opportunity to do research in the very exciting field of chaos theory. He always had time for me and patiently answered my questions whenever I popped into his office. I am particularly grateful for his understanding and acceptance of my very spontaneous holiday trip to Madagascar in order to take care of a woman, for which I had to cancel a conference participation.

Many thanks also to Nelly for helping with the bureaucracy as well as for always being in a good mood and having time for a nice and funny chat.

I am also very grateful to the rest of the TP3 group for the inspiring and stimulating scientific as well as non-scientific discussions. In particular, I would like to thank Otti not only for thoroughly proofreading my thesis but also for entertaining me in the office and trying to teach me how to treat a (Belgian) woman.

Last but not least very special thanks to all my friends and in particular to my family who always supported me and cheered me up during the occasionally hard times of my PhD. It is always nice to be home where I can enjoy the ease and comfort of a supporting place and where I can recharge my batteries.

Würzburg
April 2013

Steffen Zeeb

Contents

Chapter 1

Introduction

Dynamical systems which are coupled in some way can synchronize their properties [1]. Oscillators, for example, can synchronize their periodic motion, i.e., their phase and/or their frequency.

Synchronization of coupled oscillators was first described and investigated by Huygens in the 17th century. While observing two clocks which were suspended at the same wooden beam he realized that they synchronized their phases and frequencies. The wooden beam served as a connection which transmitted the tiny oscillations of the clocks, hence coupling the clocks.

Synchronization is ubiquitous in nature. It occurs in all kind of subjects, from chemistry over biology and medicine to physics and engineering. For example the circadian rhythm of mammals including human beings is synchronized to the Earth's 24 hour period. In engineering synchronization is often deliberately used for frequency stabilization in electric circuits. Even in finance it plays a role in the synchronization of economic activities. Synchronization also typically occurs in complex networks as a collective behavior of the network elements [2–7]. Complex networks are present in nature as well as in technology and are of very much importance especially in our highly interconnected world. Typical examples are food webs, the internet and social networks with millions of different elements. These elements can form subgroups with a hierarchy, yielding a complex structure. The dynamical units of such networks can synchronize giving rise to a collective behavior. For example, in neuroscience it is well known that neurons can synchronize their firing patterns. The natural pacemaker cells of the human heart, controlling the electrical signals causing the heart to pump, also synchronize. In Southeast-Asia fireflies synchronize the phases of their flashes until eventually a whole population of fireflies flashes in unison.

There exists various types of synchronization. Besides phase and frequency synchronization, complete synchronization where all system properties are synchronized is also possible. If the states of the systems are identical at all times one speaks of identical synchronization, whereas for generalized synchronization the states of the systems are related by some functional form. For many applications the coupling signals are transmitted with a time delay which is much larger than the internal time

scales of the individual oscillators. Nevertheless it is possible for the dynamical systems to synchronize without any time shift (isochronal or zero-lag synchronization). If the states of the synchronized systems do not coincide at the same time, but one systems lags behind the other system one speaks of achronal or lag synchronization.

It is surprising that not only oscillating system can synchronize but that synchronization is also possible for chaotic systems [8, 9]. Chaos was first observed in numerical simulations by Lorenz who studied a simplified mathematical model for atmospheric convection in 1963 [10]. He discovered that the deterministic system, which he was investigating, showed an irregularly oscillating behavior for a wide range of parameters. The trajectories settled onto a strange attractor. For the Lorenz equations this attractor is called Lorenz attractor and it resembles the two wings of a butterfly. The characteristic property of chaos is the sensitive dependence of the system's dynamics on the initial conditions which is also popularly referred to as butterfly effect. The sensitive dependence on initial conditions was already mentioned by Henri Poincaré in a particular case of the three-body problem in 1890 [11]. Small deviations are exponentially amplified leading to an unpredictable dynamics on long time scales in practice. Hence, one would naively think that synchronization cannot occur in chaotic systems. However, it is possible for coupled chaotic systems that deviations transversal to the synchronization manifold are reduced while deviations within the manifold are amplified, leading to a synchronized chaotic dynamics. This was first shown by Pecora and Carroll in 1990 [12].

Chaos synchronization is of fundamental interest in nonlinear dynamics, with applications in neural networks, coupled lasers, electronic networks, traffic dynamics, genetic circuits and secure communication to name a few [13–18]. A particularly interesting phenomenon in this context is the zero lag synchronization of chaotic units, despite the long interaction delays [19–23]. This phenomenon can be applied for chaos based cryptography [24]. Communication by synchronized chaotic electronic circuits [25–27] as well as by synchronized chaotic lasers [28, 29] have been demonstrated in the laboratory. Secure communication with chaotic lasers has even been realized in a commercial fiber-optic network over a 120 km distance [30]. The standard devices used in optical chaos synchronization are semiconductor lasers with optical feedback. By re-injecting parts of the output light back into the cavity, with the help of an external mirror, the laser can become chaotic, i.e., the amplitude and phase show a chaotic dynamics. The dynamics of the chaotic laser intensity can, to a good approximation, be described by a system of delayed coupled differential equations, the so-called Lang-Kobayashi equations [31]. Many of the effects which occur for coupled lasers modeled by the Lang-Kobayashi equations, also occur for much simpler systems described by coupled maps. In this thesis we study such maps and try to obtain generic results for chaos synchronization which are also valid for more complex systems such as chaotic lasers.

1.1 Outline

The thesis is divided into two sections. In Chapters 2 and 3 the background theory is presented. It is then applied in Chapters 4, 5 and 6 to investigate various aspects of chaos synchronization of time-delayed coupled chaotic maps. No special knowledge of chaos theory is assumed. All concepts of chaos theory which are of relevance in this context are introduced in the two theory chapters.

In Chapter 2, the basic concepts of chaos theory are presented. The mathematical/physical meaning of the term "chaos" is defined. Lyapunov exponents, as a quantitative measure of chaos, are explained and a chaotic attractor and its dimension is defined. Also, some simple chaotic systems are presented.

Chapter 3 deals with more advanced concepts of chaos theory focusing on chaos synchronization of networks. In particular, the master stability function method, the main tool for analyzing the synchronization properties of a chaotic network, is presented. The theory is illustrated by a simple system of two coupled maps for which analytical as well as numerical results are shown.

In Chapter 4, chaotic systems with multiple delays on different time scales are studied. A single Bernoulli map with different self-feedback is analyzed analytically and the obtained insights are then applied to a network of networks with different delays between subnetworks and within a subnetwork. A network of tent maps is investigated numerically.

Chapter 5 discusses the attractor dimension at the transition to complete chaos synchronization. Two definitions of the dimension of a chaotic attractor are studied. The Kaplan-Yorke dimension is determined from the spectrum of Lyapunov exponents and is compared to the correlation dimension, which is obtained from analyzing the systems dynamics. For Bernoulli networks the scaling of the Kaplan-Yorke dimension as well as of the Kolmogorov entropy with system size and time delay is investigated. The investigations of the attractor dimension are finally extended to systems with parameter mismatch.

In Chapter 6 the linear response of synchronized chaotic systems to small external perturbations is studied. On the basis of two coupled chaotic units different quantities for measuring the linear response to noisy signals, such as the second moment and the bit error rate, are defined and studied. Thereafter the investigation of the linear response is extended to more complicated models, in particular to a chain of three units and a four units network.

Finally, Chapter 7 gives a summary of the results and discusses potential topics for future research.

Chapter 2

Basic Theory – Introduction to Chaos Theory

In this chapter we aim to derive some of the basic concepts of chaos theory which we can build on in later chapters.

In the first section we give a definition of a chaotic system. In the following sections some basic notions are introduced. In particular, the *Lyapunov exponent*, which gives a quantitative measure of chaos, is explained and a *strange* or *chaotic attractor* and its dimension is defined. Also, some simple chaotic systems are presented.

This chapter is a very condensed review about the main important principles of chaos theory. A more comprehensive introduction to the basic concepts can be found in the book of Strogatz [32] and, on a more advanced level, in the book of Schuster and Just [8].

2.1 Definition of Chaos

In contrast to everyday language a chaotic system is by no means a "messy" system which cannot be handled or investigated mathematically. It is rather a dynamical system which mathematical treatment is quite complicated and for which one cannot make any long term predictions. There is no universally accepted mathematical definition but a mathematical not rigorous definition of chaos which captures the three key ingredients is the following:

"Chaos is *aperiodic* long-term behavior in a *deterministic* system that exhibits *sensitive dependence on initial condition*." [32]

Even though the system is deterministic in principle, i.e., the system's future is fully determined by its initial conditions with no random elements involved, in practice its behavior cannot be predicted accurately in the long term. This is due to the nonlinearities which cause the system to be highly sensitive to the initial conditions such that small initial differences eventually yield very different outcomes. In more mathematical terms, two initially close-by trajectories separate exponentially fast with time. By aperiodic behavior it is meant that the system will not settle down

to a fixed point nor will eventually repeat its dynamics. This will be explained in more detail in the section about chaotic attractors, see Section 2.3. These properties of chaotic systems are making long term-predictions impossible in general.

2.2 Lyapunov Exponents

The sensitive dependence on initial conditions of chaotic systems, which causes two initially nearby trajectories to separate exponentially fast with time, can be described in a more quantitative way.

Consider two trajectories which are initially separated by a distance $\delta(0)$. An exponentially fast separation means that the distance for future times $\delta(t)$ evolves according to

$$|\delta(t)| \sim |\delta(0)|e^{\lambda t}\,, \tag{2.1}$$

where the exponent λ is usually called the (largest) Lyapunov exponent (LE). For $\lambda > 0$ the trajectories separate exponentially fast and the system has a chaotic behavior.

For higher dimensional systems there is not only one LE but for each system's dimension there is a corresponding LE. This set of LEs is called LE spectrum. Thus an infinitesimal sphere in phase space describing the initial uncertainty of a state will become distorted into an ellipsoid with the k-th LE determining the evolution of the k-th principle axis of the ellipsoid. In most cases the evolution of the ellipsoid is dominated by the largest LE and it is therefore sufficient to only consider this exponent and neglect the smaller ones when investigating the stability of a system.

In the following we will derive an analytical expression for the LE in case of maps. Analytically computing the largest LE or the whole spectrum of LEs can only be done in a few, very rare cases. In general we have to rely on numerical simulations to compute a system's LEs spectrum. An algorithm to accomplish this task is presented subsequently.

2.2.1 Lyapunov Exponents of Iterated Maps

We start with a discrete map which reads as

$$x_{t+1} = f(x_t)\,, \tag{2.2}$$

and consider an initial perturbation δx_0 such that it is

$$x_1 + \delta x_1 = f(x_0 + \delta x_0)\,. \tag{2.3}$$

Linearizing equation (2.3) we find for the pertubation

$$\delta x_1 = f'(x_0)\delta x_0\,. \tag{2.4}$$

Iterating this equation further we eventually obtain

$$\delta x_t = f'(x_{t-1})\, f'(x_{t-2}) \ldots f'(x_0)\, \delta x_0 = \prod_{t=0}^{t-1} f'(x_t)\, \delta x_0 \,. \tag{2.5}$$

The LE is defined as the mean exponential divergence or convergence of a sequence

$$|\delta x_t| \approx e^{\lambda t}\, |\delta x_0| \,, \tag{2.6}$$

with $t \to \infty$ and $|\delta x_0| \to 0$. Hence we find for the LE

$$\lambda = \lim_{t\to\infty} \frac{1}{t} \sum_{i=0}^{t-1} \ln |f'(x_i)| \,. \tag{2.7}$$

If the probability distribution $\rho(x)$ of state x is know the LE can be obtained from following formula:

$$\lambda = \int \ln |f'(x)|\, \rho(x)\, \mathrm{d}x \,. \tag{2.8}$$

2.2.2 Numerical Computation of Lyapunov Exponents

In general we do not know the probability distribution $\rho(x)$ and therefore have to rely on numerical simulations to obtain the LE. Also, the computation of the whole LE spectrum of a system has usually to be done by means of numerical simulations.

To numerically obtain the spectrum of LEs of a dynamical system of the form[1]

$$\frac{\mathrm{d}}{\mathrm{d}t} x(t) = f(x) \,, \tag{2.9}$$

which has the following variational equation

$$\frac{\mathrm{d}}{\mathrm{d}t} \delta x(t) = Df(x)\, \delta x(t) \,, \tag{2.10}$$

a Gram-Schmidt orthonormalization procedure according to Farmer can be used [33]. In presenting the algorithm I closely follow the PhD thesis of Flunkert [34].

The Gram-Schmidt procedure is depicted in Figure 2.1 for a system of dimension two. In order to compute the n many leading LEs n orthonormalized initial perturbations must be chosen (black arrows in left sketch). These perturbations are subjected to the system's dynamics and evolve according to the LEs of the (eigen-)directions (red arrows) the perturbations have components in. This evolution of the perturbations is dominated by the largest LE[2]. Thus eventually most of the perturbations

[1] The algorithm is presented for the more general case of differential equation but is the same for iterated maps. For maps simply replace the differential equation and the variational equation with its discrete counterparts, equations (2.2) and (2.4).

[2] To be more precise for all perturbations which have a component in the direction of the largest LE.

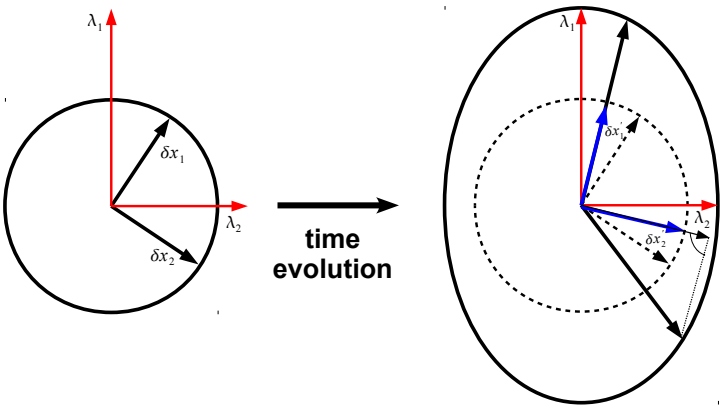

FIGURE 2.1: Illustration of the Gram-Schmidt procedure.

will align in the direction of the largest LE (black solid arrows in right sketch). After an appropriate time the perturbation vectors have to be realigned (so that they will eventually align in the directions of the n leading LE) and renormalized (so that they do not become infinity). The blue arrows have been orthogonalized with respect to the upper black solid arrow and have eventually been normalized. With these new perturbation vectors the procedure is repeated. After sufficient iterations the perturbation vectors will eventually align in the (eigen-)directions of the LEs. Keeping track of the growth rate of the perturbation vectors between succeeding orthonormalization processes yields the LEs.

The precise algorithm for numerically computing the spectrum of LEs is as follow [35]:

1. In order to obtain the first n LEs, choose $i = 1, 2, \cdots, n$ orthonormal perturbation vectors $\delta\vec{x}_i(0)$
2. Simulate the system equation (2.9) and the variational equation (2.10) for each $\delta\vec{x}_i(0)$ over an appropriate period t
3. Orthogonalize the resulting perturbation vectors $\delta\vec{x}_i(t)$ using a Gram-Schmidt procedure to obtain the vectors $\overline{\delta\vec{x}_i(t)}$ (no normalization).
4. An estimate for the i-th LE is given by $\lambda_i = \frac{1}{t}\ln\frac{|\overline{\delta\vec{x}_i(t)}|}{|\delta\vec{x}_i(0)|} = \frac{1}{t}\ln|\overline{\delta\vec{x}_i(t)}|$
5. Normalize $\overline{\delta\vec{x}_i(t)}$ and start from 2 with these vectors
6. Calculate the mean for each λ_i

2.3 Chaotic Attractor and its Dimension

The long-term behavior of a dynamical system is determined by the type of the attractor of the system (in case that the trajectories are not going to infinity). After a

transient phase the state of a system will approach an attractor which has a dimension which is in general smaller than the initial phase space. An attractor is loosely speaking a region in phase space which attracts all system's trajectories in its vicinity. A mathematical more precise definition can, for example, be found in reference [36] or [37].

As classical attractors there exist fixed points, limit cycles and quasiperiodic attractors. In contrast to these classical attractors, on a strange or chaotic attractor[3] the trajectories exhibits sensitive dependence on initial conditions. Nevertheless all neighboring trajectories converge to the strange attractor. Thus the trajectories are confined to a bounded region of the phase space, the attractor, yet they separate exponentially fast (at least initially) without being periodic. This seemingly contradiction is explained by a stretching and folding mechanism.[4] Since trajectories cannot intersect in the phase space the dimension of the phase space must be larger than two in order for this stretching and folding mechanism to happen. Thus chaos can only occur in dynamical systems with a phase space dimension larger than two. Note that this restriction is not valid for maps where trajectories are not lines in phase space but where the points can "jump around" wildly in phase space.

A dimension can be assigned to these various attractors. A fixed point has the dimension zero, a limit cycle the dimension one and a quasiperiodic attractor the dimension two or larger. Chaotic attractors do not have an integer dimension but a fractal dimension. There exists numerous definitions for the dimension of a chaotic attractor which should all yield the correct integer dimension for classical problems. These definition can be mainly split in two groups the so-called *metric dimensions* and the *dimension of the natural measure*.

For the metric dimensions some kind of metric is needed, i.e., a definition of space where the distance of two points is defined. The dimension of the natural measure needs beyond that some kind of probability distribution which weights the density of trajectories in the different regions of the attractor. The most common metric dimensions are the box (or capacity) and the Hausdorff dimension. Typical dimensions of the natural measure are information, pointwise and correlation dimension.

Another definition of dimension which conceptually neither fits to the metric dimension nor the dimension of the natural measure is the *Kaplan Yorke (KY)* dimension. Sometimes it is also referred to as Lyapunov dimension. It focuses on the dynamical properties of the attractor (temporal mean values of the divergence/convergence of nearby trajectories) whereas the former two definitions focus on the statistical properties (spatial mean values in the phase space). They are related by the ergodic theory.

[3] The term strange attractor was first introduced by Ruelle and Taken in 1971 [38].

[4] A simple example illustrates the separation of an initially dense set onto a vast but limited region very well. Imagine a dough with a small blob of food coloring. The dough gets flatten, folded over and rolled out again. This process is repeated several times until eventually the blob is spread out over the whole dough. A similar mechanism causes the trajectories on the chaotic attractor to be separated exponentially fast while at the same time being confined to a bounded region.

The practical meaning of the dimension of an attractor is that it characterizes the attractor and its underlying dynamics (periodic, chaotic...) and that it yields the number of necessary parameters to describe the system.

In the following we will explain the information, correlation and the KY dimension in more detail since we will use these definitions later in this work. A good and more comprehensive review of the various definitions of dimension can be found in reference [39].

2.3.1 Information Dimension

The information dimension D_I is a generalization of the box dimension D_B. The box dimension is defined by the scaling of the number of boxes $N(\xi)$ of n-dimensional cubes, which are needed to cover the entire attractor, with its edge length ξ. It is $N(\xi) \sim \xi^{-D_B}$.

The information dimension takes into account the relative probability p_i of the cubes used to cover the attractor, i.e., the natural measure of the attractor. First, we introduce the information function

$$I(\xi) = \sum_{i=1}^{N(\xi)} p_i \log \frac{1}{p_i} \,, \tag{2.11}$$

which in information theory is "the amount of information necessary to specify the state of a system to within an accuracy ξ, or equivalently, it is the information obtained in making a measurement that is uncertain by an amount ξ" [39]. The information dimension is then defined as

$$D_I = \lim_{\xi \to 0} \frac{I(\xi)}{\log 1/\xi} \,. \tag{2.12}$$

Note, for equal probabilities $p_i = \frac{1}{N(\xi)}$ it follows $I(\xi) = \log N(\xi)$ and hence $D_I = D_B$. Whereas in general it is $D_I \leq D_B$.

2.3.2 Correlation Dimension

The correlation dimension was introduced by Grassberger and Procaccia [40, 41] and is the definition which is generally used in practical applications. Unless most other definitions which are mostly of theoretical use this definition offers a feasible method for computing the attractor dimension numerically.

The correlation function $C(\xi)$ gives the probability that two arbitrary points of a given time series $\mathbf{x}$ have a spatial distance less or equals ξ. It is given by

$$C(\xi) = \frac{2}{N(N-1)} \sum_{i=1}^{N} \sum_{j=i+1}^{N} \Theta(\xi - |\mathbf{x}_i - \mathbf{x}_j|) \,, \tag{2.13}$$

where Θ is the Heaviside step function and $\mathbf{x}_i$ and $\mathbf{x}_j$ are two arbitrary points of the time series of length N.

The correlation function scales like a power law for small ξ, $C(\xi) \sim \xi^{D_C}$, and defines the correlation dimension D_C by

$$D_C = \lim_{\xi \to 0} \lim_{N \to \infty} \frac{\partial \ln C(\xi, N)}{\partial \ln \xi} \,. \tag{2.14}$$

The correlation dimension sets a lower bound on the different definitions of the attractor dimension. In particular, it is

$$D_C \leq D_I \leq D_B \,. \tag{2.15}$$

2.3.3 Kaplan-Yorke Dimension

Almost every initial condition in the basin of an attractor has the same LEs λ_i, thus the spectrum of LEs can be seen as a property of the attractor. Therefore we can associate the spectrum of LEs of an attractor with its dimension. Kaplan and Yorke were the first who draw this connection between the LE spectrum and the dimension of an attractor [42].

Considering a discrete spectrum $\lambda_1 \geq \lambda_2 \geq \ldots$, the KY dimension[5], D_{KY}, is defined as the largest number M for which the sum of LEs is still positive plus an interpolation term which yields the fractal part of the dimension,

$$D_{KY} = M + \frac{\sum_{k=1}^{M} \lambda_k}{|\lambda_{M+1}|} \,. \tag{2.16}$$

In their original work Kaplan and Yorke conjectured that the KY dimension is equals the capacity dimension which has later on be disproved by means of some counterexamples. Nowadays it is conjectured that for a typical attractor the KY dimension is equals the information dimension [43, 44], i.e.,

$$D_{KY} = D_I \,, \tag{2.17}$$

which is commonly referred to as the *Kaplan-Yorke conjecture*. Note that "typical" is used since there exists non-generic examples for which the KY conjecture does not hold [40]. But the validity of the KY conjecture is generally restored when small perturbations are added to these non-generic examples.

Kolmogorov entropy

From the Lyapunov spectrum we can also calculate the *Kolmogorov entropy*, K, which quantifies the predictability of the system [45]. It is defined as the sum over all positive LEs

$$K = \sum_i \lambda_i \quad \text{for } \lambda_i > 0 \,. \tag{2.18}$$

[5] The KY dimension is sometimes also called Lyapunov dimension.

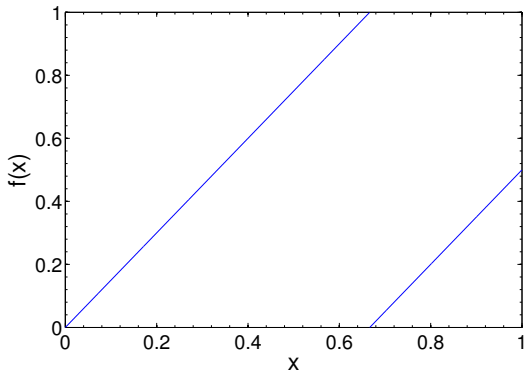

FIGURE 2.2: Bernoulli map with $a = 1.5$

The smaller the Kolmogorov entropy, the more predictable the system. In other words, K is a measure for the chaoticity of the system. The more chaotic the system is the shorter the time span is for which accurate prediction can be made. The prediction time is $t \sim 1/K$.

2.4 Simple Chaotic Systems

In the following we will present some simple chaotic systems, namely discrete maps of the form

$$x_{t+1} = f(x_t)\,. \tag{2.19}$$

The huge advantage of a map is that its simulation needs much less computational power than the simulation of continuous flows. The current state is mapped to a future state by a simple rule, whereas for flows differential equations have to be integrated by, for example, a Runge-Kutta method which is a computationally intensive task.

2.4.1 The Bernoulli Map

The Bernoulli map is given as

$$f(x) = (a\,x) \mod 1\,, \tag{2.20}$$

and is chaotic for $a > 1$. A plot of the map is shown in Figure 2.2.

The Bernoulli map is a very popular chaotic model because of its simplicity. In the derivation of its derivative the discontinuity can be neglected and hence the derivative can be considered as constant [46]

$$f'(x) = a\,. \tag{2.21}$$

This allows for an analytical treatment in contrast to most other chaotic models.

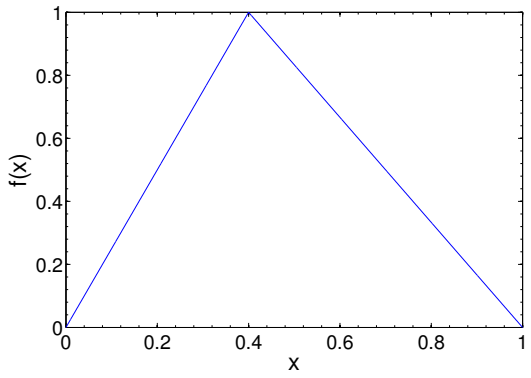

FIGURE 2.3: Tent map with $a = 0.4$

The LE of the map is obtained from equation (2.7) and yields

$$\lambda = \ln a \,. \tag{2.22}$$

Thus the LE is positive, and hence the Bernoulli map becomes chaotic, for $a > 1$. A convenient choice for the parameter a for the Bernoulli map is $a = 1.5$ since for small values of a the map is only weakly chaotic and for values $a > 2$ there is more than one discontinuity in the interval $[0, 1]$.

2.4.2 The Tent Map

The tent map is given as

$$f(x) = \begin{cases} \frac{1}{a}\, x & \text{for } 0 \le x < a \\ \frac{1}{1-a}\,(1-x) & \text{for } a \le x \le 1 \end{cases} \,. \tag{2.23}$$

For the map to be chaotic we have to choose the parameter a to be $0 < a < 1$. A typical plot of the map is shown in Figure 2.3.

For a single Tent map the values of x are uniformly distributed among all possible values $0 \le x \le 1$. Therefore, with the probability of a we are on the left branch of the map, which increases with a constant slope of value a, and with the probability $a - 1$ on the right branch, which decreases with a constant slope of value $a - 1$. Substituting this probability distribution $\rho(x)$ for the tent map into equation (2.8) we obtain the following LE,

$$\lambda = -a \ln a - (1-a) \ln (1-a) \,. \tag{2.24}$$

It is positive for $0 < a < 1$.

2.4.3 The Logistic Map

The logistic map is given as

$$f(x) = a\, x(1-x) \,, \tag{2.25}$$

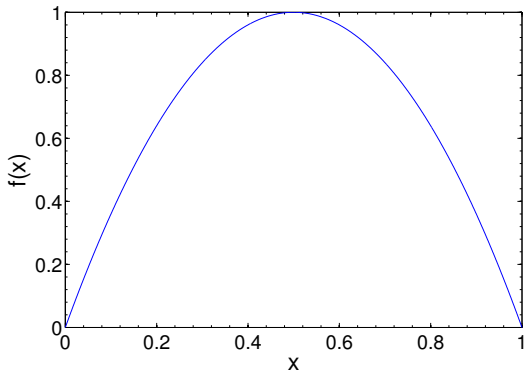

FIGURE 2.4: Logistic map with $a = 4$

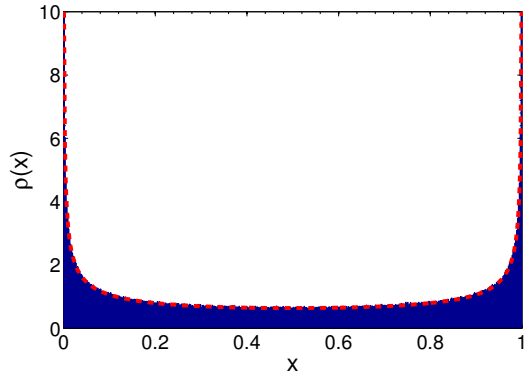

FIGURE 2.5: Probability distribution $\rho(x)$ for the logistic map with $a = 4$ (dashed red curve) together with a normalized histogram of the map for $l = 10^6$ time steps.

where the parameter a is typical set to $a = 4$ to ensure that the map is chaotic. For other choices of a we might run into one of the various periodic windows of the logistic map.

For $a = 4$ an analytical expression for the probability density $\rho(x)$ of the state x can be derived which reads [45]

$$\rho(x) = \frac{1}{\pi\sqrt{x(1-x)}} \,. \tag{2.26}$$

Figure 2.4 shows a plot of the map and Figure 2.5 shows the distribution $\rho(x)$ together with a histogram obtained from simulations of the dynamics of the logistic map.

Chapter 3

Advanced Theory – Chaos Synchronization

After having introduced some basic concepts of chaos theory and some simple chaotic systems we focus on *chaos synchronization* in this chapter.

We start by presenting a general model of a network consisting of identical chaotic units. This is the basic model which will be considered in different aspects throughout the thesis. A network of identical units can in principle completely synchronize. The stability of synchronization is analyzed mainly by means of the *master stability function* method. It is also shown how the synchronization of a network can be measured in numerical simulations. These methods are then applied to a system of coupled maps to illustrate the theory. Finally, sub Lyapunov exponents and the concept of weak and strong chaos are introduced.

3.1 Networks

A network is composed of nodes and links connecting these nodes. Since we are interested in chaos synchronization the nodes represent chaotic units such as the ones presented in the previous chapter. The topology of the network is given by the *adjacency matrix*. Its eigenvalues determine the synchronization properties of the network, as we will see later in this chapter.

The systems which we investigate in this work are networks composed of identical units which can send signals via links, i.e., they are coupled in some way. One can for example think of lasers which are connect via glass fibers [30]. The coupling strength shall be adjustable and is described by some coupling parameters. The signal which is sent from one unit to another generally has a finite travel time. Thus there is usually a time delay present in the system.

The dynamics of the ith unit with the dynamical variable $x_i(t)$ in such a network

composed of N units is given by the following differential equation

$$\dot{x}_i(t) = \eta_0 F[x_i(t)] + \eta_s F[x_i(t-\tau_s)] + \sigma \sum_j^N G_{ij} H[x_j(t-\tau_c)] \ . \tag{3.1}$$

The dynamic variable $x_i(t)$ can in general be multi-dimensional. The function $F[x]$ specifies the internal dynamics of the units and the function $H[x]$ couples the time-delayed variable of the connected units. The topology of the network, i.e., which units are coupled and their coupling strength, is given by the adjacency matrix G_{ij}. We choose the row sum of G_{ij} to be constant, $\sum_j G_{ij} = 1$, with $G_{ii} = 0$ and all other entries non negative. Thus the adjacency matrix only defines the coupling between different units and every unit normalizes its input from all other units. The first part on the left hand side of equation (3.1) describes the local dynamics of the unit and is weighted with the parameter η_0, the second part gives the self-feedback with strength η_s and the third part the external coupling where σ determines the strength of the coupling. In this way we are able to adjust the delay times and the coupling strength of the external- and the self-coupling independently. All external delay times, τ_c, and all self-feedback times, τ_s are identical, respectively.

Equation (3.1) is motivated from systems of coupled chaotic semiconductor lasers. A laser with delayed feedback is modeled by the Lang-Kobayashi equations [31] which, for a network of lasers, can be written in the form of equation (3.1). The systems variable $x_i(t)$ is then a three dimensional vector containing the real and imaginary part of the electric field and the charge carrier inversion of the ith laser.

Figure 3.1 shows a ring network of four coupled units with self-feedback which is described by equation (3.1) and for which the adjacency matrix looks as follows

$$G = \begin{pmatrix} 0 & 0 & 0 & 1 \\ 1 & 0 & 0 & 0 \\ 0 & 1 & 0 & 0 \\ 0 & 0 & 1 & 0 \end{pmatrix} \ . \tag{3.2}$$

A matrix with nonnegative entries and row sum equals one is called *stochastic matrix* and has some specific properties.

Perron-Frobenius-Theorem Every stochastic square matrix with real nonnegative entries has the real eigenvalue $\gamma_0 = 1$ and for every other eigenvalue, γ_i, it is $|\gamma_i| \leq 1$ [47].

3.2 Synchronization in Networks

The various interacting units of a network can synchronize [1, 7, 9]. There exists numerous kinds of possible synchronization patterns such as complete synchronization where all states of the system coincides or cluster synchronization where the system is clustered in groups which are synchronized independently from one another. We can

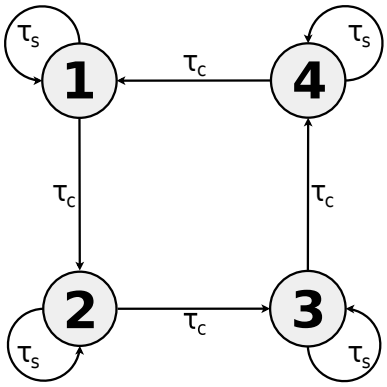

FIGURE 3.1: Ring network of four identical units with uni-directional coupling and self-feedback.

also distinguish between isochronal (equal in time) and achronal (different in time) synchronization and different synchronization types such as identical or generalized synchronization. For identical synchronization the states of the synchronized units are identical whereas for generalized synchronization there is a functional relation between the states.

In the following we will focus on complete isochronous synchronization. A network of identical chaotic units with time-delayed couplings can synchronize to a common chaotic trajectory without any time shift between these units which in this case is also referred to as zero lag synchronization [48–52].

The completely synchronized state $s(t) = x_1(t) = x_2(t) = \ldots$ is a solution of the system's equations (3.1) of the network presented in the previous section. The dynamics of the completely synchronized system is reduced to the dynamics of a single unit and is given by

$$\dot{s}(t) = \eta_0 F[s(t)] + \eta_s F[s(t-\tau_s)] + \sigma H[s(t-\tau_c)] \ . \tag{3.3}$$

In other words the dynamics of the synchronized system is confined to the synchronization manifold (SM) and is independent of the topology of the network, e.g., the number of units and their couplings. We consider only networks where this equation has chaotic solutions for sufficiently large values of σ, i.e., equation (3.3) yields at least one positive LE.

Note that the coupling scheme with $\sum_j G_{ij} \neq 0$ which we have chosen is called invasive coupling since in case of complete synchronization the system's dynamics is still rendered by the coupling of the units. The influence of the coupling terms with time delay τ_c is present in the synchronized case due to the non vanishing sum of $\sum_j G_{ij} \neq 0$. Hence the dynamics of the synchronized system differs from the dynamics of a single isolated unit of the network. In contrast, for a diffusive coupling, where $\sum_j G_{ij} = 0$, the dynamics of the synchronized system is identical to the dynamics of an isolated unit of the system.

The existence of a synchronized solution does not necessarily mean that the

system synchronizes or keeps synchronized in practice. Therefore the stability of the synchronized state is of much importance. The synchronization is stable if small perturbations to the synchronized state do not affect the synchronization of the system, i.e., if small perturbations from the SM are damped. The synchronization is unstable if small perturbations increases with time and eventually destroy the synchronization. The stability of the synchronization of networks of identical units, in particular with regard to coupling strengths, can be analyzed by means of a master stability function.

3.2.1 Master Stability Function

The master stability function method was introduced by Pecora and Carroll [53] to determine the stability of a completely synchronized state of a system in a general approach, without having to define the details of the setup or the particular coupling. The idea is to do a linear stability analysis of the system around the SM and decouple the resulting equations by diagonalizing the coupling matrix. Eventually a single equation for each eigenmode of the system is obtained determining its stability. It was originally applied to networks of identical units without any delays but has in the meantime been extended to systems with delayed couplings [54] and with non identical units [55, 56].

In order to investigate the stability of the completely synchronized state we examine how small perturbations, $\delta x_i(t)$, from the synchronized state evolve with time, whether they will decay, such that the synchronized state is stable or whether the perturbations will grow, such that the system eventually desynchronizes, i.e., the synchronization is unstable.

Linearizing the system's equations (3.1) around the synchronized state, s, i.e., for $x_i(t) = s(t) + \delta x_i(t)$, we obtain

$$\begin{aligned}\delta\dot{x}_i(t) = \eta_0\, DF[s(t)]\ \delta x_i(t) + \eta_s\, DF[s(t-\tau_s)]\ \delta x_i(t-\tau_s) \\ + \sigma \sum_j^N G_{ij}\, DH[s(t-\tau_c)]\ \delta x_j(t-\tau_c)\,. \end{aligned} \tag{3.4}$$

This is a system of N coupled linear differential equations with time delayed feedback and time dependent coefficients. The adjacency matrix, G, can be diagonalized such that the set of equations decouple. Each of the resulting equations is associated with an eigenvector, $\vec{y}_l$, of the adjacency matrix and its corresponding eigenvalue γ_l, with $l = 1, \ldots, N$.

Any arbitrary infinitesimal perturbation $\delta\vec{x}$ of the synchronized trajectory can be decomposed into the eigenvectors of the system, i.e., $\delta\vec{x} = \sum_k \xi_k\, \vec{y}_k$ with ξ_k being the amplitude in the direction of the kth mode. The equations for the amplitudes read

$$\begin{aligned}\dot{\xi}_k(t) = \eta_0\, DF[s(t)]\, \xi_k(t) + \eta_s\, DF[s(t-\tau_s)]\ \xi_k(t-\tau_s) \\ + \sigma\, \gamma_k\, DH[s(t-\tau_c)]\, \xi_k(t-\tau_c)\,. \end{aligned} \tag{3.5}$$

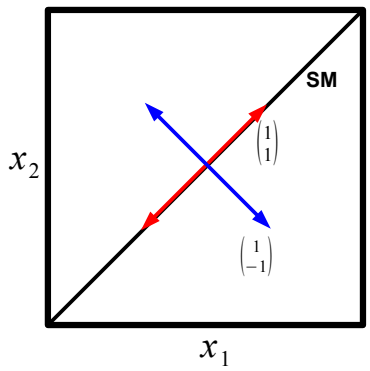

FIGURE 3.2: Synchronization manifold with eigenmodes of a system of two mutually coupled units.

This is know as the master stability function where the coupled system equations have been transformed to uncoupled equations by diagonalizing the coupling matrix. Each of the resulting equations describes a perturbation in the direction of one of the eigenmodes of the system. Choosing the row sum of the coupling matrix as $\sum_j G_{ij} = 1$ ensures that the largest eigenvalue of G is $\gamma_1 = 1$ corresponding to the so-called longitudinal eigenmode of form $\vec{y} = (1, 1, \ldots, 1)^T$ describing perturbation within the SM. All other eigenmodes with eigenvalues $\gamma_l, l = 2, ..., N$ correspond to perturbations transversal to the SM and are therefore called transversal eigenmodes.

Example: A network of two mutually coupled units has the adjacency matrix $G = \begin{pmatrix} 0 & 1 \\ 1 & 0 \end{pmatrix}$ with the eigenvalues $\gamma_1 = 1$ and $\gamma_2 = -1$ and the corresponding eigenvectors $\vec{y}_1 = \begin{pmatrix} +1 \\ +1 \end{pmatrix}$ and $\vec{y}_2 = \begin{pmatrix} +1 \\ -1 \end{pmatrix}$. A perturbation in the direction of the first mode, $\vec{y}_1$, perturbs both units in the same way and therefore the system stays synchronized. Whereas a perturbation in direction of the second mode, $\vec{y}_2$, destroys the synchronization since the units are perturbed in opposite directions, i.e., perpendicular to the SM. This is depicted in Figure 3.2 where the diagonal line is the SM on which it is $x_1 = x_2$.

Solving the master stability function, equation (3.5), for example by a Gram-Schmidt orthonormalization procedure as described in Section 2.2.2, it yields a whole spectrum of LEs for each eigenvalue γ_k of G. For time continuous chaotic systems with time delayed couplings (including self-feedback for a single unit) the system is infinite dimensional and has a continuous spectrum of LEs. In the chaotic regime, perturbations within the SM increase exponentially fast, i.e., the linearized dynamics has to be unstable for $\gamma_1 = 1$. Thus a chaotic system has (at least) one positive longitudinal LE. For the synchronization to be stable, all perturbations transversal to the SM must decay exponentially fast, i.e., the master stability function must

yield only negative LEs for all transversal eigenvalues. Thus the maximum LEs of each mode k determines whether a perturbation in the direction of this mode decays or grows, i.e., whether the synchronization is stable or not.

For systems with constant coefficients in equation (3.5), i.e., $DF[x], DH[x] = const$, a polynomial equation of degree $\tau + 1$ (with $\tau = \max(\tau_s, \tau_c)$) can be derived. For these systems the LE spectrum can be obtained analytically by finding the roots of the polynomial equation. A typical example is the Bernoulli map where $f'(x) = a$. The derivation of the polynomial equation for Bernoulli systems is discussed in Section 3.4.

In general we consider networks where the delay times, τ_s and τ_c, are much larger than any other time scale of the system [57]. In this limit, $\tau_s = \tau_c \to \infty$, one can show that the SM of the network, described by equation (3.1), is stable for

$$|\gamma_{max}| < \exp(-\lambda_{max}\,\tau)\,, \tag{3.6}$$

with $|\gamma_{max}|$ the transversal eigenvalue of G with the largest absolute value and λ_{max} the maximum LE of the SM, equation (3.3) [58, 59]. Equation (3.6) relates the network's ability to synchronize to an eigenvalue gap, $1-|\gamma_{max}|$, between the largest eigenvalue of the coupling matrix G, $\gamma_1 = 1$, and the largest absolute transversal eigenvalue. In case of $|\gamma_{max}| < 1$ the system can synchronize if the chaos is sufficiently small, that is, in the limit $\lambda_{max} \to 0$. Since λ_{max} depends on the coupling strength σ, equation (3.6) determines the critical coupling σ_c where chaos synchronization appears.

Note that although the master stability method is a universal stability standard it is a weak criteria for the stability of synchronization. Unstable periodic orbits or locally unstable areas on the attractor can cause the system to be temporally unsynchronized, when there is noise or parameter mismatch, by burst away from the SM known as attractor bubbling [60–64].

3.3 Quantifying Synchronization in Simulations

In the previous chapter we derived a method to compute the stability of the synchronized state analytically. All LEs corresponding to perturbations transversal to the SM were required to be negative in order for the synchronization to be stable. The master stability function method is primarily a theoretical method to determine the stability and it is mainly important because it relates the stability properties to the network's topology, i.e., the eigenvalues of the adjacency matrix. In most cases we are unfortunately not able to solve the master stability equation due to the time dependent coefficients. Only for simple systems we can determine the stability by applying the master stability function method, as we will see in Section 3.4. For more complex systems we have to rely on numerical simulation and therefore need to develop other criteria for the stability of the synchronized state. In principle we could determine the LE spectrum of the system numerically, as described in Section 2.2.2, but this is a rather computationally powerful task. In the following we will

present two simple criteria to measure the synchronization of two units numerically, namely the cross correlation and the synchronization probability.

3.3.1 Cross Correlation

One measure for the synchronization of two units is their cross correlation. Computing cross correlations is a standard method from time series analysis to estimate the degree to which two time series, x_t and y_t with $t = 0, \ldots, n$, are correlated. It is defined as the mean of the product of the deviation of the two quantities from their means, normalized by their standard deviations such that it becomes a dimensionless quantity, i.e,

$$C_\tau = \frac{\langle (x_t - \langle x \rangle)\,(y_{t-\tau} - \langle y \rangle) \rangle}{\sigma_x \sigma_y} = \frac{\langle x_t y_{t-\tau} \rangle - \langle x \rangle \langle y \rangle}{\sigma_x \sigma_y}\,, \tag{3.7}$$

with the standard deviation $\sigma_x = \sqrt{\langle x^2 \rangle - \langle x \rangle^2}$ and an optional shift τ between the two time series. For $C = 1$ the units are completely synchronized, for $C = -1$ completely anti-synchronized and for $C = 0$ totally uncorrelated.

3.3.2 Synchronization Probability

Another measure for the synchronization of two units is the synchronization probability, ϕ. It measures the fraction of time for which the two trajectories, x_t and y_t, are closer than some threshold Θ, i.e., $|d_t| = |y_t - x_t| < \Theta$. The synchronization probability is normalized by the total length n of the time series and reads

$$\phi = \frac{\#\,|d_t| < \Theta}{n}\,. \tag{3.8}$$

Thus $\phi = 1$ means that the trajectories of the two units are closer than the threshold, Θ, for all times and are therefore considered as completely synchronized. In contrast for $\phi = 0$ the units are completely unsynchronized since the trajectories never get closer than the threshold.

A reasonable choice for the threshold, Θ, is crucial for obtaining correct results. Choosing the threshold too large will yield synchronization where the system is not actually synchronized. The synchronization probability is in particular a good synchronization criterion for systems with noise or small parameter mismatch. In such systems the trajectories never coincide perfectly but deviate approximately by the magnitude of the noise or the parameter mismatch, respectively. Setting the threshold to around the strength of the noise or parameter mismatch, respectively, will suppress this effect when investigating the synchronization.

3.3.3 Numerical Simulations – General Remarks

When simulating chaotic systems we start from random initial conditions. In general the system goes through a transient phase until it settles into its long term behavior.

When computing different quantities of the system such as the cross-correlation, the synchronization probability or the LE spectrum, we have to discard the transient behavior in order to obtain accurate results. If not stated otherwise we choose the initial conditions to be random but close together $\delta < 10^{-6}$ such that the system is nearly synchronized. This ensures that the transient phase and hence the run time before the system settles into its long term behavior is short. In principle, completely arbitrary initial conditions can be used but the transient phase can, in this case, be rather long. For all simulations, if not stated otherwise, the first 10^6 iterations are discarded which from experience is more than sufficient to ensure that the system has settled to its long term behavior.

3.4 Chaos Synchronization of Coupled Iterated Maps

In Section 3.1 we presented networks of continuous systems described by coupled differential equations. For a numerical investigation we need to integrate the differential equation, for example, by a Runge-Kutta method which is a computationally intensive task. Iterated maps, in contrast, are much easier to analyze numerically. The current state is mapped to a future state by a simple iterative rule. Therefore we will in general investigate networks of iterated maps with time-delayed coupling rather than coupled differential equations in this work. Note that in some respects chaotic maps have different properties compared to chaotic flows, for example for phase synchronization [65], but with regard to complete synchronization maps and flows are very similar. Many of the results, presented in this thesis, are also observed in numerical simulations of chaotic differential equations.

Similarly to equation (3.1) which describes a network of continuous units, we can state an equation for networks of iterated maps such as these presented in Section 2.4. The dynamics of such a unit i in state x_t^i at time t in a network composed of N units is given by

$$x_{t+1}^i = (1-\epsilon) f(x_t^i) + \epsilon\kappa f(x_{t-\tau_s}^i) + \epsilon(1-\kappa) \sum_j^N G_{ij} f(x_{t-\tau_c}^j) \,. \tag{3.9}$$

The function $f(x)$ specifies the internal chaotic dynamics of the units. We either choose the Bernoulli, tent or logistic map, described in Section 2.4. G_{ij} is the adjacency matrix, defined as before. The coupling constants are chosen such that the dynamics of the units is confined to the unit interval, where ϵ weights the internal dynamics to the delayed dynamics and κ determines the ratio between self-feedback and external interaction. For example, by setting $\kappa = 0$ the self-feedback in the system is turned off and by setting $\kappa = 1$ all units become decoupled.

The synchronized state

$$s_{t+1} = (1-\epsilon) f(s_t) + \epsilon\kappa f(s_{t-\tau_s}) + \epsilon(1-\kappa) f(s_{t-\tau_c}) \,, \tag{3.10}$$

is a solution of the system's equations and determines the SM. Similar to Section 3.2.1, perturbations of the SM can be associated with the eigenvalues γ_k of the

coupling matrix G determining the topology of the network. The amplitude ξ_t^k of each mode obeys the linear master stability function

$$\xi_{t+1}^k = (1-\epsilon) f'(s_t)\, \xi_t^k + \epsilon\kappa f'(s_{t-\tau_s})\, \xi_{t-\tau_s}^k + \epsilon(1-\kappa)\, \gamma_k f'(s_{t-\tau_c})\, \xi_{t-\tau_c}^k \,. \quad (3.11)$$

In general, this equation cannot be solved analytically due to the time dependent coefficients. But for Bernoulli maps, where $f'(x) = a = const$, we can do further analytics.

Note that by construction the system is chaotic for all values of ϵ since the largest LE of the longitudinal spectrum, the spectrum determining the dynamics of the SM, is always positive.

3.4.1 Analytical Results

We assume that the perturbation in direction of the eigenmodes, i.e. the amplitudes ξ_t^k, are either exponentially decaying or increasing. Thus we use as an ansatz

$$\xi_t^k = z_k^t\, \xi_0^k \,, \quad (3.12)$$

with z_k a complex number of the form

$$z_k = e^{\lambda_k + i\omega_k} \,. \quad (3.13)$$

A perturbation in direction of the kth eigenmode decays exponentially fast if

$$|z_k| < 1 \,, \quad (3.14)$$

or equivalent

$$\lambda_k = \ln|z_k| < 0 \,, \quad (3.15)$$

where λ_k is the LE corresponding to the kth eigenmode.

Substituting $f'(x) = a$ into the master stability equation (3.11) and using the ansatz (3.12) we obtain the polynomial equation

$$z_k^{\tau_c+1} - (1-\epsilon)\, a\, z_k^{\tau_c} - \epsilon\kappa\, a\, z_k^{\tau_c-\tau_s} - \epsilon(1-\kappa)\, a\, \gamma_k = 0 \,, \quad (3.16)$$

where $\tau_c > \tau_s$ was assumed. We are able to (numerically) solve this polynomial equation with respect to z_k for different eigenvalues γ_k. For each γ_k equation (3.16) yields $\tau_c + 1$ many solutions for z_k. Hence, we obtain a spectrum of LEs for each eigenvalue.

For the simple cases of $\tau_c = \tau_s = 0$ and $\tau_c = \tau_s = 1$ and also in the limit $\tau \to \infty$ the roots of the polynomial can be obtained analytically [49, 66, 67]. Hence the parameter space (ϵ, κ) for which all transversal LEs associated with the eigenvalue γ_k are negative, $\lambda_k = \ln|z_k| < 0$, can be determined. Complete synchronization is stable if the transversal LE spectra are negative for all eigenvalues $\gamma_k, k = 2, ..., N$. If only a few LE spectra are negative there can occur stable sub-lattice synchronization

depending on the structure of the eigenmodes [67]. Results for systems with multiple delay times can be found in [58].

In the following we assume identical delay times, $\tau_c = \tau_s = \tau$. In the limit $\tau \to \infty$, the critical coupling, for which the kth LE spectrum is negative, is given by

$$\frac{-1 - a\,\epsilon + a - a\epsilon\gamma_k}{a\epsilon(1-\gamma_k)} < \kappa < \frac{1 + a\,\epsilon - a - a\epsilon\gamma_k}{a\epsilon(1-\gamma_k)}\,, \tag{3.17}$$

see reference [46]. Solving this expression for ϵ we obtain (in case that $\gamma_k \in \mathbb{R}$)

$$\epsilon_c = \begin{cases} \frac{a-1}{a\kappa(1-\gamma_k)+a(1+\gamma_k)} & \text{for } \kappa \leq \frac{\gamma_k}{\gamma_k - 1} \\ \frac{a-1}{a(1-\gamma_k)(1-\kappa)} & \text{for } \kappa > \frac{\gamma_k}{\gamma_k - 1}\,. \end{cases} \tag{3.18}$$

Without any self-feedback, $\kappa = 0$, this reduces to

$$\epsilon_c = \frac{a-1}{a(1-|\gamma_k|)}\,, \tag{3.19}$$

such that the critical coupling is directly related to the eigenvalue gap $1 - |\gamma_k|$. ϵ_c becomes smaller for larger eigenvalue gaps. For $\epsilon > \epsilon_c$ the corresponding LE spectrum is negative and perturbations in this direction are exponentially damped.

Figure 3.3 shows the area of negative LE spectrum for different eigenvalues γ. All tuples (ϵ, κ) which lie within the area determined by the two lines (lower and upper bound on κ, see equation (3.17)) yield a negative LE spectrum.

Note, a network of two mutually coupled chaotic units has the transversal eigenvalue $\gamma = -1$ and can never synchronize without self-feedback, i.e., for $\kappa = 0$. A master-slave setup of two uni-directional coupled units, however, has the transversal eigenvalue $\gamma = 0$ and can always synchronize without self-feedback for a sufficiently large coupling constant ϵ. The adjacency matrix of three mutually coupled units has the two-fold degenerated eigenvalue $\gamma = -0.5$. Hence, the system can synchronize without self-feedback only if the units are not too chaotic, i.e., if the parameter a is small enough, compare Figure 3.3(a) and Figure 3.3(b).

In the limit $\tau = 0$, the coupling constants of the system's equations (3.9), ϵ and κ, can be reduced to a single parameter. Using the substitution $\alpha = \epsilon(1-\kappa)$ the systems equations become

$$x^i_{t+1} = (1-\alpha) f(x^i_t) + \alpha \sum_j^N G_{ij} f(x^j_t)\,, \tag{3.20}$$

which corresponds to setting $\kappa = 0$ in the original equations. By this reduction of parameters it is sufficient to discuss this simple case with only one coupling constant to cover all possible combinations of ϵ and κ. The coupling for which all perturbations in the k-th eigendirection are damped is determined by

$$\frac{a-1}{a(1-\gamma_k)} < \alpha < \frac{a+1}{a(1-\gamma_k)}\,, \tag{3.21}$$

see reference [46].

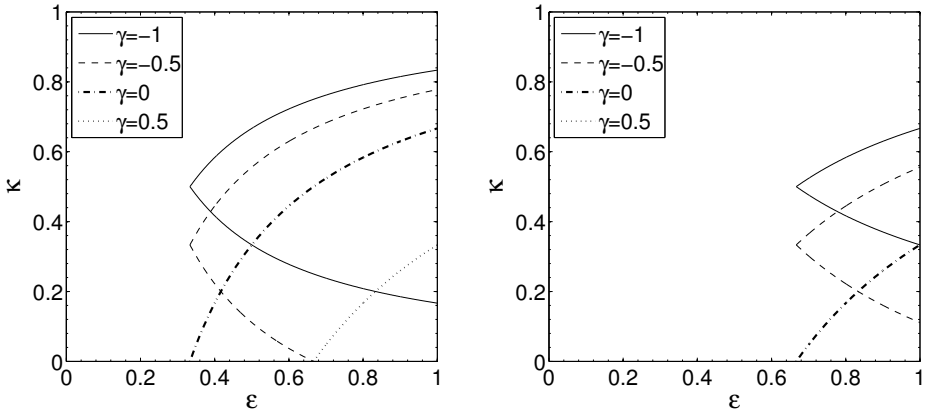

(a) $a = 1.5$ (b) $a = 3$

FIGURE 3.3: Analytical results for the parameter range where the associated LE spectrum is negative in the limit $\tau \to \infty$ for different eigenvalues γ and two different parameters a of the Bernoulli map.

3.4.2 Numerical Results

For systems consisting of tent or logistic maps we are not able to solve the master stability function analytically due to the fluctuating coefficients. Hence, we have to rely on numerical simulations to determine the region of stable synchronization.

Figure 3.4 and Figure 3.5 show the cross correlation and synchronization probability for two mutually coupled tent maps and for three all-to-all coupled logistic maps, respectively. The region of synchronization is in both cases similar to the one of coupled Bernoulli maps, compare Figure 3.3 where $\gamma = -1$ corresponds to two mutually coupled units and $\gamma = -0.5$ to three all-to-all coupled units. For the logistic maps there exists, besides the main synchronization area, a region of synchronization at $\epsilon \approx 0.18$. This represents periodic windows of the logistic map.

By comparing the analytical results for Bernoulli maps, which were obtained in the limit of large delays $\tau \to \infty$, with results from numerical simulations we find that the numerical results resemble the analytical ones very well already for $\tau = 50$. In general we choose $\tau = 100$, which is a good approximation for the large delay limit. This is depicted in Figure 3.6 which shows C and Φ obtained from simulations together with the analytical results for the synchronization region.

3.5 Lyapunov Exponents – Advanced Topics

In the previous chapter we introduced the LE as a quantifier for the chaoticity of a system. If the LE is positive two nearby trajectories separate exponentially fast and the system is chaotic. In general, a system has a whole spectrum of LEs, in particular a system with time delays. In terms of chaos synchronization all transversal LEs must be negative in order for the SM to be stable. Very often it is useful to con-

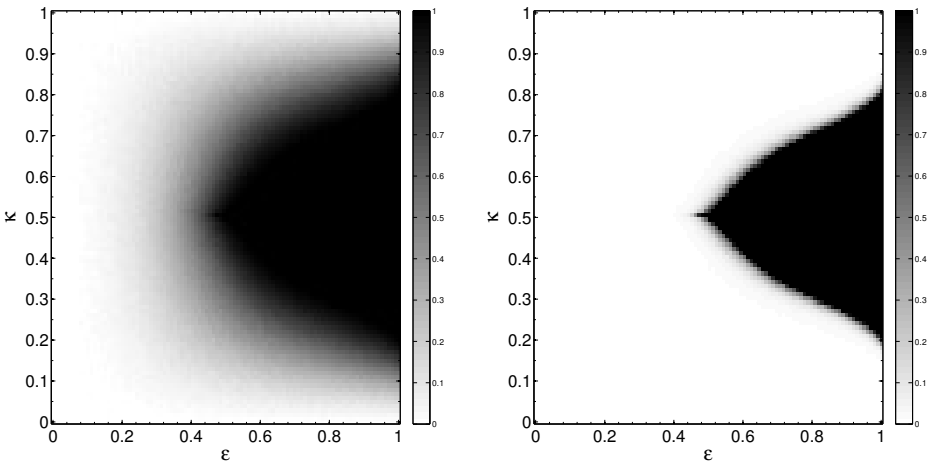

(a) Cross correlation C (b) Synchronization probability ϕ

FIGURE 3.4: Synchronization region for two mutually coupled tent maps with $a = 0.86$ and $\tau = 100$. Threshold for the computation of the synchronization probability was set to $\Theta = 0.001$.

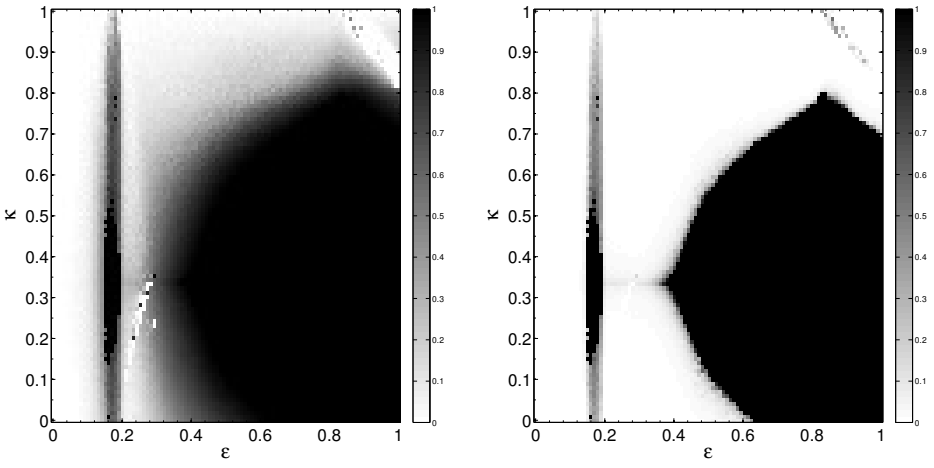

(a) Cross correlation C (b) Synchronization probability ϕ

FIGURE 3.5: Synchronization region for three all-to-all coupled logistic maps with $a = 4$ and $\tau = 100$. Threshold for the computation of the synchronization probability was set to $\Theta = 0.001$.

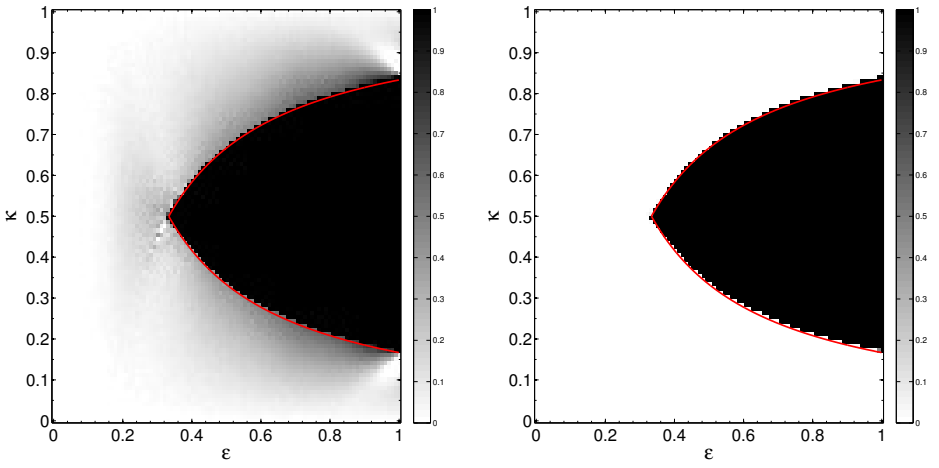

(a) Cross correlation C (b) Synchronization probability ϕ

FIGURE 3.6: Synchronization region for two mutually coupled Bernoulli maps with $a = 1.5$. Shown are the numerically obtained cross correlation C and synchronization probability Φ for $\tau = 100$ together with the analytical results for the limit $\tau \to \infty$ (red line). Threshold for the synchronization probability was set to $\Theta = 0.001$.

sider different parts of the system and their contributions to the stability of the SM separately by the so-called *sub-LE*. This concept enables us to distinguish between so-called *strong* and *weak* chaos in networks and to classify the synchronizability of coupled chaotic units.

3.5.1 Lyapunov Spectrum

For networks of coupled units described by equations (3.1) and (3.9), respectively, the master stability function method, presented in Section 3.2.1, yields a method to determine the evolution of perturbations associated to the different eigenvalues γ_k of the adjacency matrix G. For Bernoulli maps it is possible to derive a polynomial equation of degree $\tau + 1$ (equation (3.16)). Finding the roots of this equation one obtains $\tau + 1$ many LEs for each eigenmode. But in general we cannot solve the master stability function due to the non-constant coefficients. Instead, we have to use a numerical orthogonalization method according to Gram-Schmidt, as described in Section 2.2.2. The system's equations (3.1) and (3.9), respectively, are linearized around the chaotic trajectory and simulated for a set of orthogonal perturbation vectors which have to be re-orthogonalized after an appropriate amount of time. The Lyapunov spectrum is computed from the change in magnitude of the perturbation vectors.

Figure 3.7 shows an example for a triangle of all-to-all coupled Bernoulli units with $\gamma_1 = 1$ and $\gamma_2 = \gamma_3 = -1/2$. The transversal spectrum is two-fold degenerated since the transversal eigenvalue has the multiplicity two. The system is chaotic for all values of ϵ since the largest LE of the γ_1 spectrum is always positive. The transition

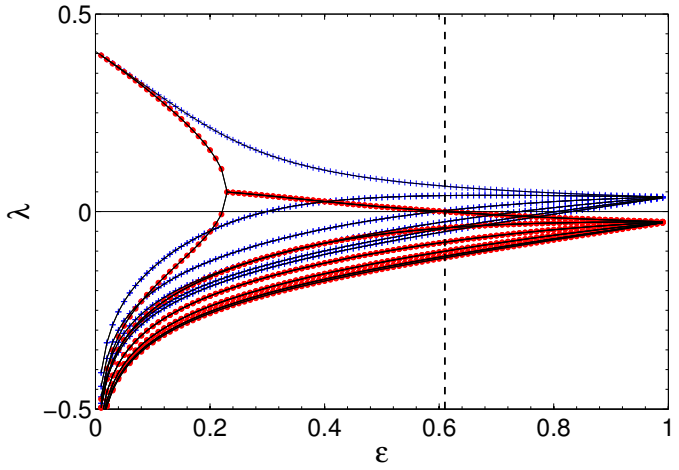

FIGURE 3.7: Lyapunov spectra vs. coupling strength ϵ for a system of three all-to-all coupled Bernoulli maps with the parameters $a = 1.5$, $\kappa = 0$ and $\tau = 10$. The blue crosses show the longitudinal spectrum associated with $\gamma_1 = 1$ and the red dots show the transversal spectrum associated with $\gamma_2 = \gamma_3 = -1/2$. Both spectra were obtained by solving the polynomial equations derived from the master stability function. The black solid lines show the Lyapunov spectrum computed by Gram-Schmidt from simulations of the full system. The vertical dashed line indicates ϵ_c where to its right the system is synchronized.

to chaos synchronization occurs at ϵ_c where the maximum LE of the transversal $\gamma_{2,3}$ spectrum crosses the value zero. The spectra are obtained from solving the polynomial equation derived from the master stability function as well as by a Gram-Schmidt method from simulations of the full system. Both methods compute the spectrum in completely different ways but yield the same results.

The LE spectrum clusters into bands for ϵ-values close to 1. This can be understood as follows. For $\epsilon = 1$ and $\kappa = 0$, the systems equations (3.9) are given by

$$x^i_{t+1} = \sum_{j=1}^{N} G_{ij} f(x^j_{t-\tau}) \,. \tag{3.22}$$

Since the state at time $t+1$ is only influenced by the state at time $t-\tau$, the system is effectively given by $\tau + 1$ uncoupled identical systems of the form

$$\tilde{x}^l_{\theta+1} = \sum_{j} G_{lj} f(\tilde{x}^j_{\theta}) \,. \tag{3.23}$$

Each of these $\tau + 1$ systems is N-dimensional and gives rise to N LEs. Since there are $\tau + 1$ identical systems, each of these N exponents is $\tau + 1$ times degenerated. This holds as long as each effective system evolves on the same chaotic attractor, and thus does not rely on synchronization. For $\epsilon < 1$ the first term in equation (3.9) leads to a coupling between these effective systems and thus removes the degeneracy.

Approximated Master Stability Function

When numerically computing the LEs with the Gram-Schmidt method from the full system's equations we cannot distinguish between the spectra corresponding to different eigenvalues γ_k. Depending on the number j of different initial perturbations we obtain the largest j many LEs of the system. Only with the master stability function method it is possible to decompose the system into its various eigenmodes and compute the respective LE spectra separately, such that the LEs can be grouped into bands according to the eigenvalues. But the master stability function, equation (3.5) and (3.11), is only defined in the synchronized regime $x_t^i = x_t^j = s_s$ where all derivatives, $f'(x^l)$ with $l = 1, \ldots, N$, yield the same value, $f'(s)$. For the unsynchronized system we generally need to evaluate the linearized equations of the full system.[1] However, we can use the master stability function as a first approximation. Instead of substituting s_t, as in the synchronized case, we substitute the dynamics of a single unit, such that s_t and $s_{t-\tau}$ are replaced by x_t^i and $x_{t-\tau}^i$, respectively. For the coupling term we can either substitute the dynamics of the same unit - option 1 - or of a different unit - option 2. Hence for a system of two coupled units we obtain[2]

$$(1) \quad \xi_{t+1}^k = (1-\epsilon) f'(x_t^1)\, \xi_t^k + \epsilon\kappa f'(x_{t-\tau_s}^1)\, \xi_{t-\tau_s}^k + \epsilon\,(1-\kappa)\,\gamma_k f'(x_{t-\tau_c}^1)\, \xi_{t-\tau_c}^k\,, \tag{3.24}$$

$$(2) \quad \xi_{t+1}^k = (1-\epsilon) f'(x_t^1)\, \xi_t^k + \epsilon\kappa f'(x_{t-\tau_s}^1)\, \xi_{t-\tau_s}^k + \epsilon\,(1-\kappa)\,\gamma_k f'(x_{t-\tau_c}^2)\, \xi_{t-\tau_c}^k\,. \tag{3.25}$$

We, now, use these equations, instead of the linearized equations of the full system, to compute the LE spectrum with a Gram-Schmidt procedure. Close to the transition we expect the spectra obtained from these approximated master stability functions to resemble the true spectra very well. Surprisingly, the results obtained from equation (3.24) (option 1) are in good agreement with the true spectra not only close to the synchronization transition but for all values of ϵ. In contrast, the spectra obtained from equation (3.25) (option 2) agree with the true spectra only close to the synchronization transition (and for complete synchronization). A comparison of the different spectra is shown for the tent map in Figure 3.8. The blue and red lines are obtained using the Gram-Schmidt procedure from simulating the master stability function which is strictly only valid for the synchronized regime. The black line is obtained using the Gram-Schmidt procedure on the full system's equations and therefor yields the correct results not only for the synchronized but also for the unsynchronized regime. Within the synchronized regime the results match up to numerical accuracy, whereas outside of synchronization the results of the two methods deviate since the master stability function approach is no longer valid.

[1] Only for Bernoulli networks, where the coefficients are constant and in particular independent of the systems trajectory, the master stability function still holds in the desynchronized regime.

[2] Instead of using the dynamics of the first unit, $f'(x^1)$, we can also use the dynamics of the second unit. Both versions yield the same LE spectrum.

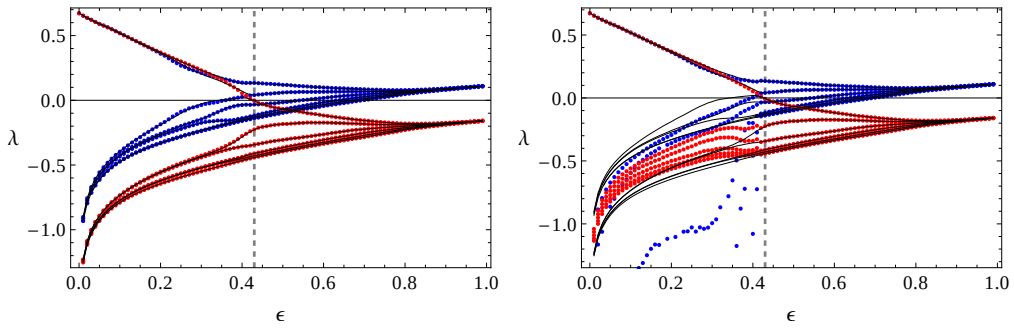

(a) Option (1) (b) Option (2)

FIGURE 3.8: Lyapunov spectra vs. coupling strength ϵ for a system of two mutually coupled tent maps with the parameters $a = 0.4$, $\kappa = 0.4$ and $\tau = 5$. The blue crosses show the longitudinal spectrum associated with $\gamma_1 = 1$ and the red dots show the transversal spectrum associated with $\gamma_2 = -1$ computed by Gram-Schmidt from simulations of the master stability function. The black solid lines show the Lyapunov spectrum computed by Gram-Schmidt from simulations of the full system. The vertical dashed line indicates ϵ_c where to its right the system is synchronized.

3.5.2 Sub Lyapunov Exponents

A perturbation from the SM of system (3.1) evolves according to the linearized equations (3.4). These linearized equations determine the stability of the SM and yield the system's spectrum of LEs.

As we will see in the following section, it is useful to consider a reduced form of these equations which only consist of the instantaneous part. The sub-LE λ_0 is defined as the LE describing the evolution of a perturbation $\delta x_i^0(t)$ according to the reduced equation

$$\delta \dot{x}_i^0(t) = \eta_0 \, DF[s(t)] \; \delta x_i^0(t) \, . \tag{3.26}$$

Since there is is no delay term present the sub-LE is sometimes also called local or instantaneous exponent [58, 59].

The sub-LE should not be confused with the LE of a single isolated unit. Although, there does not appear a delayed coupling term in equation (3.26), it includes the synchronized state $s(t)$ of the full system determined by equation (3.3). The synchronized system's trajectory is affected by the coupling of the units and is different to the one of a single unit due to the invasive coupling scheme of the system. Hence, the influence of the network is present in the synchronized trajectory and is, in particular, imprinted on the sub-LE.

For a network of Bernoulli units the linearized equations do not depend on the trajectory since $f'(x) = a$. In this case, the sub-LE is identical to the LE of the corresponding isolated units. Consider, for example, a network of Bernoulli units

described by

$$x_{t+1}^i = (1-\epsilon) f(x_t^i) + \epsilon\kappa f(x_{t-\tau}^i) + \epsilon(1-\kappa) \sum_j^N G_{ij} f(x_{t-\tau}^j) \,. \tag{3.27}$$

The sub-LE is determined from the reduced linearized equation

$$\delta x_{t+1}^i = (1-\epsilon) f'(s_t) \delta x_t^i \,, \tag{3.28}$$

and it yields

$$\lambda_0 = \ln |(1-\epsilon)\ a| \,. \tag{3.29}$$

Note that for this setup in the limit $\tau \to \infty$, the sub-LE agrees with the true maximum system's LE for $\epsilon < \epsilon_{crit} = 1 - 1/a$. In this parameter range the sub-LE is positive. For $\epsilon > \epsilon_{crit}$ the sub-LE becomes negative and deviates from the maximum system's LE [3].

Using the sub-LE it is possible to characterize the chaotic behavior and the synchronizability of a network by distinguishing between weak and strong chaos, as explained in the following section.

3.5.3 Strong and Weak Chaos

Strong and weak chaos is defined in the limit of large time delays by the scaling behavior of the maximum LE, λ_{max}, of the system. For strong chaos the maximum LE is independent of the delay whereas for weak chaos it scales inversely with the delay, $\lambda_{max} \sim 1/\tau$ [59]. In both cases, all other exponents scale inversely with the delay.

The type of chaos determines the synchronization properties of the system. A necessary condition for chaos synchronization is that the system is in the regime of weak chaos. A network can synchronize for weak chaos if the eigenvalue gap of the coupling matrix is sufficiently large compared to the product of the maximum LE and the delay time, compare equation (3.6). Synchronization is not possible for strong chaos.

Strong/weak chaos is determined by the sign of the sub-LE. In case of strong chaos the sub-LE is positive, $\lambda_0 > 0$, and a good approximation for the maximum LE, $\lambda_{max} \approx \lambda_0$. For weak chaos the sub-LE is negative, $\lambda_0 < 0$.

In the previous section we derived the sub-LE for a network of Bernoulli maps, see equation (3.29). It is independent of τ and approximates the true maximum exponent very well for $\epsilon < \epsilon_{crit} = 1 - 1/a$ where it is positive. In this parameter range the system is in the regime of strong chaos, whereas for $\epsilon > \epsilon_{crit}$ the sub-LE is negative and the system is in the weak chaos regime.

Note that Lepri was the first who investigated the scaling of the LE spectrum for time delayed systems using iterative maps [68]. He studied a similar equation to equation (3.27) and reported the existence of a maximum LE which is independent of the delay for certain parameters and referred to it as anomalous exponent.

[3] For a derivation of the maximum LE of this system see reference [66].

Chapter 4

Chaotic Networks with Multiple Time Delays

So far we have only considered networks with an identical time delay between all units. However, in realistic systems various different time delays may be present. Therefor we focus on systems with multiple delays in this chapter. In particular, we investigate networks of chaotic maps with multiple delays on different time scales and extend the concepts of weak and strong chaos of systems with a single delay to such hierarchical networks. The scaling behavior of the system's LE spectrum is explained and it is related to the synchronization properties of hierarchical networks.

The investigation is restricted to systems of chaotic maps. But the obtained results on the extension of strong/weak chaos to multiple delays should also be valid for chaotic flows, since strong/weak chaos occurs in continuous as well as in discrete time-delayed systems.

We start by discussing a single unit with multiple delays, where analytic results are derived for the Bernoulli map and the tent map is studied numerically. The investigation is then extended to hierarchical networks with multiple delays such as a network of a network, where the delay within the subnetworks is smaller than the delay between different subnetworks.

The discussion on chaotic networks with multiple delays presented here is based on reference [69] and closely follows the structure of this paper.

4.1 Single Unit with Multiple Delays

As explained in the previous chapter, the LEs give a quantitative measure for the chaos in a network. We can, in particular, classify a chaotic system with a large time delay τ into strong and weak chaos by the scaling behavior of its maximum LE λ_{max}. For strong chaos the maximum LE is independent of the delay and it approaches a positive constant, whereas for weak chaos it scales inversely with the delay, $\lambda_{max} = 1/\tau$. A chaotic network with a large time delay can only synchronize if it is in the weak chaos regime and if equation (3.6) is fulfilled, i.e., if the eigenvalue

gap of the coupling matrix (determined by the topology of the network) is sufficiently large compared to $\tau \cdot \lambda_{max}$. For strong chaos complete chaos synchronization is not possible.

In the following we extend the concepts of weak and strong chaos of systems with a single delay to systems with multiple delays which differ by several orders of magnitude. We particularly focus on the scaling of the full LE spectrum, in contrast to the single delay system where we mainly studied the maximum exponent.

Let us start by investigating the simplest chaotic system with multiple delays, a single chaotic map with N feedback delays of different orders of magnitudes $1 \ll \tau_1 \ll \tau_2 \ll \ldots \ll \tau_N$, which is given by

$$x_{t+1} = (1-\epsilon) f(x_t) + \epsilon \sum_{k=1}^{N} \kappa_k f(x_{t-\tau_k}) \,. \tag{4.1}$$

The coupling strength ϵ weights the instantaneous dynamics to the delayed dynamics and the coupling κ gives the strength of the various self-feedbacks. In order for the system dynamics to be confined to the range $[0,1]$ we put the following constraints on the coupling constant: $\epsilon \in [0,1]$ and $\sum_{k=1}^{N} \kappa_k = 1$.

A perturbation δx_t along the trajectory s_t evolves according to the linearized equation

$$\delta x_{t+1} = (1-\epsilon) f'(s_t) \delta x_t + \epsilon \sum_{k=1}^{N} \kappa_k f'(s_{t-\tau_k}) \delta x_{t-\tau_k} \,, \tag{4.2}$$

from which the LE spectrum can be calculated, see Section 2.2. Similar to the linearized equation of the SM discussed in the previous chapter, equation (3.11), the coefficients $f'(s_t)$ are generally time dependent, such that we cannot evaluate equation (4.2) further but have to rely on numerical simulations for determining the LE spectrum. Only for Bernoulli maps with $f'(x_t) = a$ the coefficients are constant and analytical results can be obtained.

4.1.1 Constant Coefficients

The results on constant coefficients presented in this section, were mainly obtained by Otti D'Huys and were published in reference [69]. They show the basic principles which also occur for fluctuating coefficients discussed in the following section and are included here for the sake of completeness.

For Bernoulli maps we can derive a polynomial equation from which the LEs can be computed. Similar to Section 3.4.1, by substituting $f'(x_t) = f' (= a)$ into equation (4.2) and using the ansatz

$$\delta x_t = z^t \, \delta x_0 \,, \tag{4.3}$$

for the growth or decay of a perturbation, we obtain

$$z = (1-\epsilon) f' + \epsilon f' \sum_{k=1}^{N} \kappa_k z^{-\tau_k} \,. \tag{4.4}$$

The characteristic multipliers z determine the system's LEs by

$$\lambda = \ln |z| \,. \tag{4.5}$$

A whole spectrum of exponents denoted by Λ is obtained due to the delay which renders the system high dimensional.

For a single delay system in the long-delay limit the maximum multiplier is independent of the delay for strong chaos, while the remaining multipliers scale with the delay. The delay-independent multiplier is approximated by the first term of equation (4.4)

$$z_0 = (1-\epsilon)f' \,, \tag{4.6}$$

with $|(1-\epsilon)f'| > 0$. For further details see Section 3.5.3. For systems with multiple delays of different orders of magnitudes we can assume the different multipliers to be related to different delays. That means, the multipliers can be grouped in a strongly unstable multiplier which is independent of the delay, a spectrum of multipliers scaling approximately with τ_1, a spectrum scaling with τ_2 and so on.

In analogy to the approximation of the strongly unstable multiplier we can derive the multipliers which approximately scale with τ_1 by inserting the ansatz

$$z = e^{i\omega + \gamma_1/\tau_1} \,, \tag{4.7}$$

with $\gamma_1 > 0$ into equation (4.4) and neglecting all terms of order $e^{-\gamma_1\tau_2/\tau_1}$ and higher. The characteristic polynomial for the τ_1-multipliers yields

$$e^{i\omega} = (1-\epsilon)f' + \epsilon\kappa_1 f' e^{-i\omega\tau_1 - \gamma_1} \,, \tag{4.8}$$

with the roots of this equation being located on the curve

$$\gamma_1(\omega) = \ln|\epsilon\kappa_1 f'| - \ln|e^{i\omega} - (1-\epsilon)f'| \,. \tag{4.9}$$

The number of roots increases linearly with τ_1 since the imaginary parts of these roots differ by approximately $\Delta\omega \approx 2\pi/\tau_1$. In the following we refer to the spectrum of LEs associated with these multipliers as the τ_1-spectrum or Λ_1. Note that the τ_1-spectrum corresponds to the pseudo-continuous spectrum for steady states of single-delay systems [70].

To obtain the multipliers (approximately) scaling with τ_2 we use a similar ansatz as before

$$z = e^{i\omega + \gamma_2/\tau_2} \,, \tag{4.10}$$

with $\gamma_2 > 0$. Substituting this into equation (4.4) and neglecting all terms of order $e^{-\gamma_2\tau_3/\tau_2}$ and higher, the characteristic polynomial for the τ_2-multipliers yields

$$e^{i\omega} = (1-\epsilon)f' + \epsilon\kappa_1 f' e^{-i\omega\tau_1} + \epsilon\kappa_2 f' e^{-i\omega\tau_2 + \gamma_2} \,. \tag{4.11}$$

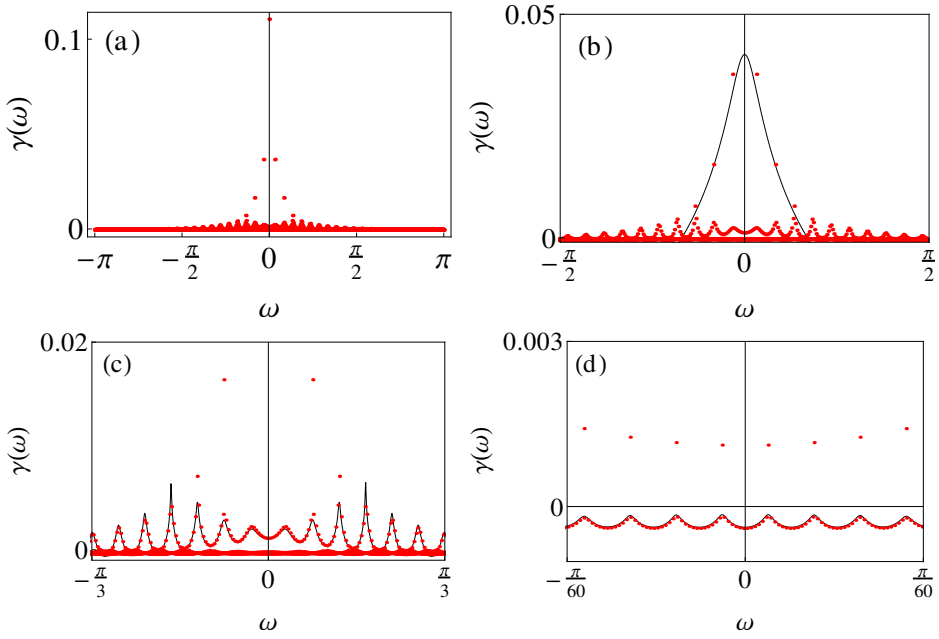

FIGURE 4.1: The spectrum of characteristic multipliers of a Bernoulli map subject to three feedback delays. The different panels are zooms. Red dots are results obtained form numerically solving equation (4.4) and the black lines are the analytic approximations for long delays $\gamma_1(\omega)/\tau_1$ (panel (b)), $\gamma_2(\omega)/\tau_2$ (panel (c)) and $\gamma_3(\omega)/\tau_3$ (panel (d)). Parameters are $a = 3$, $\epsilon = 0.63$, $\kappa_1 = 0.3$, $\kappa_2 = 0.6$, $\kappa_3 = 0.1$, $\tau_1 = 40$, $\tau_2 = 500$ and $\tau_3 = 6000$. Courtesy of Otti D'Huys.

The roots of this equation lie on the curve

$$\gamma_2(\omega) = \ln|\epsilon\kappa_2 f'| - \ln|e^{i\omega} - (1-\epsilon)f' - e^{-i\omega\tau_1}\epsilon\kappa_1 f'| \,. \tag{4.12}$$

and are associated with the τ_2-spectrum of LE. This spectrum scales inversely with the delay τ_2 and the number of exponents in this spectrum scales linearly with τ_2.

In an analogous way, we can obtain higher order spectra Λ_k scaling inversely with τ_k. For each delay of the system we obtain a corresponding spectra. Only the spectra Λ_N related to the longest delay time τ_N can have stable multipliers, all other spectra consist of only unstable ones.

The spectrum of LEs obtained from numerically solving equation (4.4) is compared to the analytical long delay approximations $\gamma_k(\omega)$ in Figure 4.1. The LE spectra are well approximated by the analytical curves for the long-delay limit and we can clearly distinguish the different scaling properties of the LEs, including one strongly unstable multiplier. Moreover, the shorter delay τ_1 appears as a modulation parameter in the τ_2-spectrum, while the τ_3-spectrum shows oscillations with periodicities of both $2\pi/\tau_1$ and $2\pi/\tau_2$.

4.1.2 Fluctuating Coefficients

We showed in the previous section that the LE spectrum of a Bernoulli system, for which the coefficients in the linearized equation (4.2) are constant, is composed of various partial spectra related to different delays. In the general case the coefficients are time-dependent since $f'(x)$ usually depends on the trajectory x. An analytical treatment is therefor not possible. However, the LE spectrum can be computed numerically from the linearized equation using a Gram-Schmidt orthogonalization procedure, as explained in Section 2.2.2. We find that the LE spectrum of systems with fluctuating coefficients shows the same scaling behavior as the Bernoulli system.

In analogy to weak and strong chaos discussed in the previous chapter, the LE spectra of the different orders τ_k are numerically obtained from integrating a reduced form of the linearized equation (4.2). The sub-LE, λ_0, is defined by the evolution of the auxiliary perturbation δx^0 according to

$$\delta x^0_{t+1} = (1-\epsilon) f'(s_t) \delta x^0_t \,, \tag{4.13}$$

and the λ_1-spectrum is obtained from the evolution of a perturbation according to

$$\delta x^1_{t+1} = (1-\epsilon) f'(s_t) \delta x^1_t + \epsilon \kappa_1 f'(s_{t-\tau_1}) \delta x^1_{t-\tau_1} \,, \tag{4.14}$$

where an additional term containing the τ_1 dependency is present. In both equations s_t denotes the dynamics of the full system determined by equation (4.1). By adding further delay terms this can be continued computing the τ_2- ... τ_N-spectrum.

Note that when computing the τ_k-spectrum from the reduced linearized equation according to a Gram-Schmidt procedure, we also obtain all positive exponents of the partial spectra with smaller order, i.e., all positive exponents of the τ_l-spectra with $l < k$. That is because the additional terms in the reduced equation are each separated by a time scale from its preceding order and for the exponential explosion of a perturbation, which dynamics is on the time scale of τ_i, any terms on a longer time scale τ_j with $j > i$ is negligible. In the definition of the τ_k-spectrum we exclude all positive exponents already included in spectra of smaller order. Hence, the partial spectra do not overlap and each τ_k-spectrum scales inversely with its distinct delay τ_k.

τ_k-chaos

The most important quantity describing a chaotic system is the maximum LE, λ_{max}. It defines the type of chaos in the system. If it does not vary with any of the system's time delays we speak of strong chaos. In the strong chaos regime the sub LE λ_0 is positive and a good approximation for λ_{max}. While the maximum LE exponent is independent of the delays, all delay times may be present in the total LE spectrum for systems in strong chaos, i.e., the first few positive exponents vary with τ_1, the following few positive exponents with τ_2 and so on.

If λ_{max} scales with any of the delays we speak of weak chaos and λ_0 is negative. We can further sub-divide weak chaos into τ_1-chaos where the maximum LE scales

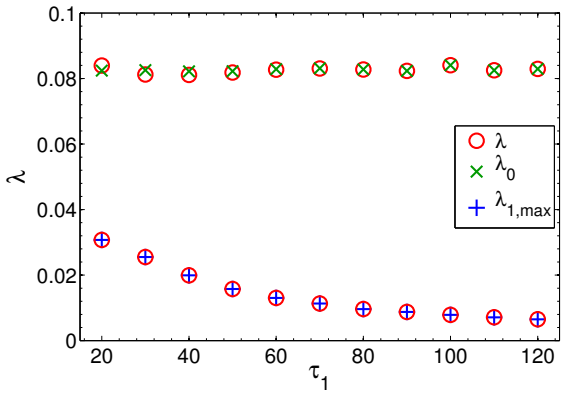

FIGURE 4.2: Lyapunov exponents of a tent map in the strong chaos regime for different feedback delays τ_1 and fixed feedback delay $\tau_2 = 500$. Shown are the two largest LEs of the full spectrum (λ), the maximum exponent of the τ_1-spectrum ($\lambda_{1,max}$) as well as the sub LE λ_0. The other parameters are $a = 0.4$, $\epsilon = 0.4$, $\kappa_1 = 0.7$ and $\kappa_2 = 0.3$.

with $1/\tau_1$. For τ_1-chaos (at least) the maximum LE of the τ_1-spectrum is positive, i.e., it is $\lambda_{1,max} > 0$, and $\lambda_{1,max}$ is a good approximation for λ_{max}. If $\lambda_{max} \propto 1/\tau_2$ we speak of τ_2-chaos and it is $\lambda_{1,max} < 0$ but $\lambda_{2,max} > 0$. For τ_2-chaos the maximum LE is approximated by $\lambda_{2,max}$. Consequently τ_k-chaos is defined by the scaling of λ_{max} with $1/\tau_k$.

Note that although the maximum LE scales with $1/\tau_k$ for τ_k-chaos, the total spectrum may be composed of several other positive LEs scaling with a different, i.e, longer, delay.

Tent Map System

In the following we demonstrate the separation of the total LE spectrum into different partial spectra for a tent map subject to two different feedbacks. The dynamics of this setup is given by

$$x_{t+1} = (1-\epsilon) f(x_t) + \epsilon\,\kappa\, f(x_{t-\tau_1}) + \epsilon\,(1-\kappa) f(x_{t-\tau_2})\,. \tag{4.15}$$

For the strongly chaotic regime, Figure 4.2 compares the total LE spectrum with the sub-LE and the maximum LE of the τ_1-spectrum for varying time delays τ_1 but fixed delay τ_2. For a large enough τ_1 the maximum LE λ_{max} is well approximated by the sub-LE λ_0 and both exponents are independent of the delay τ_1. In contrast, the second largest LE of the total spectrum, $\lambda_{(2)}$, scales inversely with τ_1. This exponent is perfectly approximated by the maximum exponent of the τ_1-spectrum, $\lambda_{1,max}$.

For the same setup, the first $k = 25$ LEs of the total spectrum together with LEs of the τ_1-spectrum and the sub-LE are shown in Figure 4.3. λ_{max} is well separated from the rest of the spectrum and is approximated by λ_0. The next few positive exponents of total spectrum $\lambda_{(2)}, \cdots, \lambda_{(7)}$ coincide with the τ_1-spectrum. As the

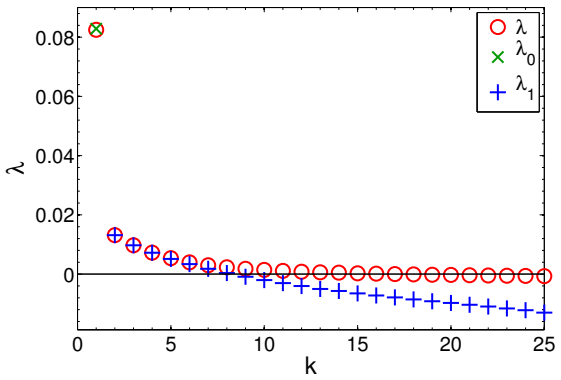

FIGURE 4.3: Lyapunov exponents of a tent map with two feedbacks $\tau_1 = 60$ and $\tau_2 = 500$ in the strong chaos regime. Shown are the first $k = 25$ LEs of the full (λ) and the sub (λ_1) Lyapunov spectra as well as the sub LE λ_0. The other parameters are $a = 0.4$, $\epsilon = 0.4$, $\kappa_1 = 0.7$ and $\kappa_2 = 0.3$.

exponents of the full spectrum approaches zero the τ_1-spectrum starts to deviate from the full spectrum.

The scaling behaviour of the LE spectrum of a system in strong chaos is depicted in Figure 4.4. The largest exponents (except for the maximum one) scale inversely with τ_1 and coincide with the τ_1-spectrum. For a discrete system the total number of LEs increases linearly with the delay. Hence the number of exponents scaling inversely with τ_1 also increase linearly with the delay. By plotting $\lambda_k\tau_1$ vs. k/τ_1, where k denotes the kth exponent of the spectrum, for different delays τ_1 the spectrum converges to a curve for all exponents scaling inversely with τ_1, see Figure 4.4(a). The curves diverge when the exponents no longer scale with τ_1. These smaller exponents are approximated by the τ_2-spectrum and scale inversely with $1/\tau_2$. This scaling can be highlighted, similar to the τ_1-scaling, by plotting $\lambda_k\tau_2$ vs. k/τ_2 for varying τ_2. When plotting the total LE spectra in this way, all smaller exponents of the spectra converge to a curve and, hence, scale inversely with τ_2. This is depicted in Figure 4.4(b).

4.2 Networks with Multiple Delays

When studying the synchronization properties of networks of networks the concepts of strong and various τ_k-chaos typically become relevant. In these networks at least two different time scales are generally present. Typically, signals are exchanged with a short time delay τ_1 between the nodes within a subnetwork, whereas a signal needs a much larger time τ_2 to travel between the different subnetworks.

Systems with multiple delays and their synchronizations properties have been studied extensively. For a network where the different time delays have a special integer ratio, resonances occur which, depending on the ratio, either stabilize or inhibit chaos synchronization [52] and for networks with a distribution of delays

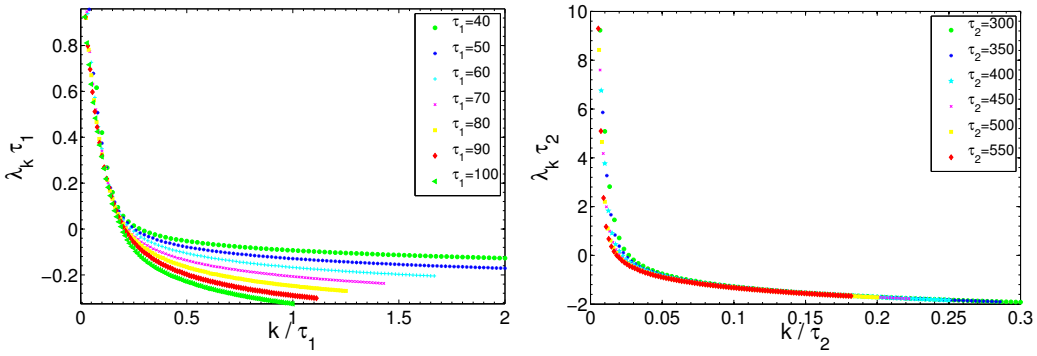

(a) τ_1-scaling for fixed τ_2 (b) τ_2-scaling for fixed τ_1

FIGURE 4.4: Lyapunov spectrum of a tent map with two delayed feedbacks. Shown are the LEs λ_k with $k = 2 - 100$ for different values of the feedback delays. The left panel shows the scaling of positive exponents with τ_1 for fixed $\tau_2 = 500$. The curves diverge as the smaller exponents scale with τ_2. The right panel shows the τ_2-scaling of the smaller exponents for fixed $\tau_1 = 30$. Other parameters are $a = 0.4$, $\epsilon = 0.4$, $\kappa_1 = 0.8$ and $\kappa_2 = 0.2$.

complex behavior is expected to be suppressed [71–73].

Here we study hierarchical networks of chaotic units where the time scales between the inter-subnetwork connections are separated from the intra-subnetwork dynamics. Such hierarchical networks can be described by

$$x_{t+1}^{jm} = (1-\epsilon) f(x_t^{jm}) + \epsilon\kappa \sum_l A_{jl}^{(m)} f(x_{t-\tau_1}^{lm}) + \epsilon(1-\kappa) \sum_{sk} B_{jk}^{(ms)} C_{ms} f(x_{t-\tau_2}^{ks}) \,, \tag{4.16}$$

where matrix $A^{(m)}$ gives the coupling topology within the m-th subnetwork and matrix C gives the coupling topology of the total network, i.e., the matrix component C_{ms} determines whether the m-th subnetwork is coupled to the s-th subnetwork. Matrix $B^{(ms)}$ describes the type of coupling between the subnetworks, i.e., which unit of the m-th subnetwork is coupled to which unit of the s-th subnetwork. In the following we assume all matrices to have a row sum equal to 1, such that all units receive the same amount of input, both within and from outside the subnetwork. This restriction ensures that complete synchronization is a solution of the system's equations (4.16). Moreover, we restrict the B-matrices to have identical rows, so that each node within a subnetwork receives the same input from outside the subnetwork.

Example: Figure 4.5 shows a network of four globally coupled identical subnetworks. Each subnetwork consists of four units which are bidirectionally coupled with

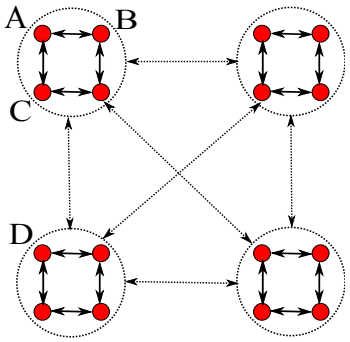

FIGURE 4.5: Network of four globally coupled subnetworks consisting of four nodes each.

their nearest neighbors in a ring setup such that matrix $A^{(m)}$ yields

$$A^{(m)} = \frac{1}{2}\begin{pmatrix} 0 & 1 & 0 & 1 \\ 1 & 0 & 1 & 0 \\ 0 & 1 & 0 & 1 \\ 1 & 0 & 1 & 0 \end{pmatrix} , \tag{4.17}$$

for all subnetworks m. The coupling between different subnetworks is of mean field type and is given by

$$B^{(ms)} = \frac{1}{4}\begin{pmatrix} 1 & 1 & 1 & 1 \\ 1 & 1 & 1 & 1 \\ 1 & 1 & 1 & 1 \\ 1 & 1 & 1 & 1 \end{pmatrix} , \tag{4.18}$$

for all combinations of m and s. The all-to-all coupling of the subnetworks is described by

$$C = \frac{1}{3}\begin{pmatrix} 0 & 1 & 1 & 1 \\ 1 & 0 & 1 & 1 \\ 1 & 1 & 0 & 1 \\ 1 & 1 & 1 & 0 \end{pmatrix} . \tag{4.19}$$

The network equation (4.16) gives rise to stable complete synchronization if the coupling parameters are chosen correctly. The stability is determined by a master stability approach similar to Section 3.2.1. The master stability function reads

$$\delta x_{t+1} = (1-\epsilon) f'(s_t)\delta x_t + \epsilon\kappa f'(s_{t-\tau_1})\delta x_{t-\tau_1} + \sigma_C \epsilon(1-\kappa) f'(s_{t-\tau_2})\delta x_{t-\tau_2} , \tag{4.20}$$

with σ_C the eigenvalues of the coupling matrix C and s_t the completely synchronized state. Complete synchronization is only possible if all corresponding LEs are negative. In the previous section we showed that, for a system with two different time

scales, all transversal LEs may be negative in the τ_2-chaotic regime only. The system completely synchronizes only for τ_2-chaos, if the necessary condition $|\sigma_C| \leq e^{-\lambda_{\max}\tau_2}$ is fulfilled.

Besides complete synchronization, where all units of the network are synchronized, cluster synchronization, where all units of a single subnetwork are synchronized but not the different subnetworks with each other, is also possible. The stability of a cluster synchronized state s_t^m is determined by the master stability function of a subnetwork, which reads

$$\delta x_{t+1} = (1-\epsilon) f'(s_t^m)\delta x_t + \sigma_A^{(m)} \kappa\epsilon f'(s_{t-\tau_1}^m)\delta x_{t-\tau_1} \,, \tag{4.21}$$

with ${\sigma_k}^{(m)}$ the eigenvalues of the connection matrix $A^{(m)}$ of the m-th subnetwork. Since we only investigate networks for which all nodes within a subnetwork receive the same input from outside the subnetwork, equation (4.21) has no explicit dependency on the inter-subnetwork delay τ_2 and it resembles the master stability function of a network with a single delay. But, in contrast to a network with a single delay, the dynamics of the cluster synchronized state s_t^m depends on the units outside the subnetwork. Thus the synchronization properties of a subnetwork still implicitly depend on the long delay τ_2. For stable cluster synchronization all transversal LEs of equation (4.21) must be negative. In the strongly chaotic regime equation (4.21) yields at least one positive transversal LE and hence no cluster synchronization is possible. We can illustrate this without any calculations. For strong chaos the maximum transversal LE of the full system is positive and roughly equals λ_0. λ_0 is approximately obtained when neglecting the last term in equation (4.21), compare equation (4.13). Hence, the master stability function of a subnetwork yields a positive maximum exponent approximately equals λ_0 for strong chaos, see discussion in the previous section. In the τ_1-chaotic regime stable cluster synchronization is possible and the first exponents of the total LE spectrum are approximately obtained from equation (4.21). Stable synchronization in the m-th subnetwork depends on the coupling architecture $A^{(m)}$ and occurs if $|\sigma_A^{(m)}| < e^{-\lambda_{max}\tau_1}$. For τ_2-chaos all nodes of a subnetwork synchronize completely irrespective of the coupling topology.

In summary, in the τ_1-chaotic regime the short delay connections determine the synchronization pattern in a subnetwork, while there is no synchronization induced by the long delay connections. In the τ_2-chaotic regime each subnetwork acts as a single node, and the synchronization pattern between these nodes is determined by the long delay connectivity.

Simulations of a network of four globally coupled subnetworks, introduced in the example above and depicted in Figure 4.5, have been performed using tent maps for the dynamics of the individual units. Results for the cross correlation of several different network elements and the different (sub-) LE λ_{max}, $\lambda_{1,max}$ and λ_0 are shown in Figure 4.6 as a function of the coupling strength ϵ. With increasing coupling ϵ the system undergoes a transition from strong to τ_1- to τ_2-chaos. For strong chaos all cross correlations are small. As ϵ increases, the correlations increase and the maximum LE decreases. When λ_0 becomes negative, i.e., in the τ_1-chaotic regime,

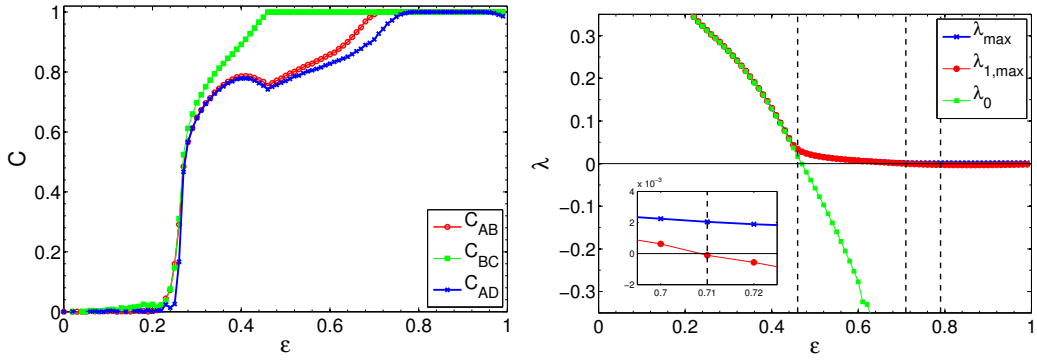

(a) Cross correlations (b) Lyapunov exponents

FIGURE 4.6: Cross correlations (left) and Lyapunov exponents (right) for a hierarchical network of tent maps depicted in Figure 4.5 as a function of the total coupling strength ϵ. Shown are the cross correlations between nodes A and B, B and C and A and D and the maximum LE $\lambda_{\max}$ together with $\lambda_{1,\max}$ as well as the sub-LE λ_0. The dashed lines indicate the synchronization transitions. The parameters are $a = 0.4$, $\kappa = 0.5$, $\tau_1 = 50$, and $\tau_2 = 500$.

sublattice synchronization occurs within the subnetworks. The diagonal elements of the ring in a subnetwork, node B and C in Figure 4.5, synchronize, having a cross correlation $C_{BC} = 1$. Note that the small difference between the transition points $\lambda_0 = 0$ and $C_{BC} = 1$ in Figure 4.6 is caused by numerical inaccuracy. Sublattice synchronization is governed by equation (4.21), with a transversal eigenvalue $\sigma_A = 0$. This equation also determines complete cluster synchronization in a subnetwork. The maximum LE determining complete cluster synchronization is obtained for the transversal eigenvalue $\sigma_A = -1$. When $\lambda_{1,max}$ becomes negative the subnetwork completely synchronizes and it is $C_{AB} = C_{BC} = 1$. As the inset in Figure 4.6 shows these two points agree perfectly in the simulations. Increasing the coupling ϵ further the whole network eventually synchronizes and it is $C_{AD} = C_{AB} = C_{BC} = 1$.

Chapter 5

Attractor Dimension at the Synchronization Transition

In this chapter we apply the theoretical knowledge on chaotic attractors and chaos synchronization of coupled units which we have gained in the previous chapters. In particular, we investigate the attractor dimension at the transition to complete synchronization in a network of chaotic units with time-delayed couplings. We determine the KY dimension from the spectrum of LEs for iterated maps and for two coupled semiconductor lasers.

Various systems display a change or discontinuity in their statistical properties, e.g. information transfer and statistical complexity, at the emergence of collective behavior such as the transition to chaos synchronization [74]. But, typically the LEs are continuous when crossing the transition to synchronization. Hence quantities derived from the spectrum of LEs seem to be continuous. However, in this chapter we show that the attractor dimension of a chaotic system with time delay is discontinuous at the transition to synchronization.

In the first section we state the problem and argue that the KY dimension must be discontinuous at the transition. The KY dimension is computed for iterated maps and compared to the correlation dimension in the following section. Section 3 shows results for two coupled semiconductor lasers. Networks of chaotic units are investigated in Section 4. The magnitude of the discontinuity in the KY dimension is calculated as a function of the network size. Furthermore the scaling of the KY dimension as well as of the Kolmogorov entropy with system size and time delay is investigated. Finally, the KY dimension for systems with parameter mismatch is computed.

Parts of the research presented in this chapter have been published in reference [75]. The numerical simulations on semiconductor lasers presented in Section 5.3 have been conducted by Thomas Dahms (TU Berlin).

5.1 Discontinuous Kaplan-Yorke Dimension

As discussed in Chapter 3 a network of identical units can, for an appropriate coupling strength, synchronize to a common chaotic trajectory without any time shift between the units. In this chapter we are mainly interested in the transition to synchronization and how the dimension of the system's chaotic attractor is changed at the transition. We consider a network of N identical nonlinear units similar to equation (3.1) presented in Section 3.1. For simplicity we neglect the self-feedback. This does not change the problem which we want to illustrate in the following but it improves the readability and prevents of focusing the readers attention to unimportant technical details.

The system equations are given by the time delayed differential equations

$$\dot{x}_i(t) = F[x_i(t)] + \sigma \sum_{j=1}^{N} G_{ij}\, H[x_j(t-\tau)] \ . \tag{5.1}$$

As before, the SM $x_i(t) = s(t)$ given by

$$\dot{s}(t) = F[s(t)] + \sigma H[s(t-\tau)] \ , \tag{5.2}$$

is a solution of this network and its stability is determined by the following master stability function

$$\dot{\xi}_k(t) = DF[s(t)]\, \xi_k(t) + \sigma\gamma_k DH[s(t-\tau)]\, \xi_k(t-\tau) \ . \tag{5.3}$$

The master stability function determines the systems's LEs. For each eigenvalue γ_k a whole spectrum of LEs is obtained. All parameters and variables have the same meaning as in Chapter 3.

By changing the control parameter of the system, i.e., the coupling strength σ, the system exhibits a transition from an unsynchronized to a synchronized state. At the synchronization transition the dynamics becomes restricted to the SM. For a synchronized system the systems's trajectories only explore the phase space associated with the SM. The attractor is therefor embedded in the SM and all dimensions of the phase space perpendicular to the SM do not contribute to the attractor dimension. Figure 5.1 depicts the contraction of the attractor to the SM for an increasing coupling strength.

The dimension of a chaotic attractor is not uniquely defined. The various definitions have been introduced and have been explained in Section 2.3. In the following we consider the KY dimension, D_{KY}, and the correlation dimension, D_C. The KY dimension is computed from the full system's LE spectrum which is composed of the spectra of all eigenvalues γ_k. It is given by

$$D_{KY} = M + \frac{\sum_{l=1}^{M} \lambda_l}{|\lambda_{M+1}|} \ . \tag{5.4}$$

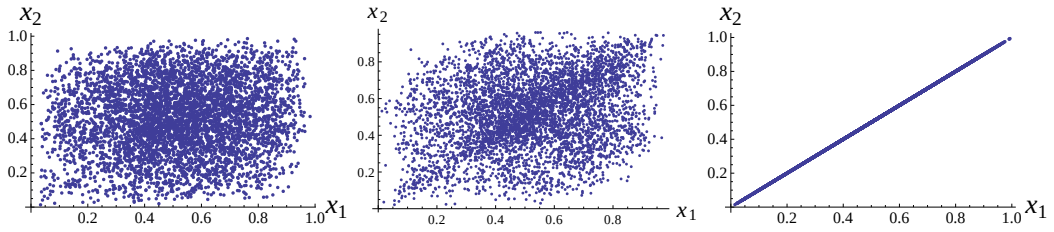

FIGURE 5.1: Sketch of the system's attractor for two coupled units for increasing coupling strength (from left to right). The high dimensional space due to the time delay is projected into the plane where the diagonal $x_1 = x_2$ denotes the synchronization manifold.

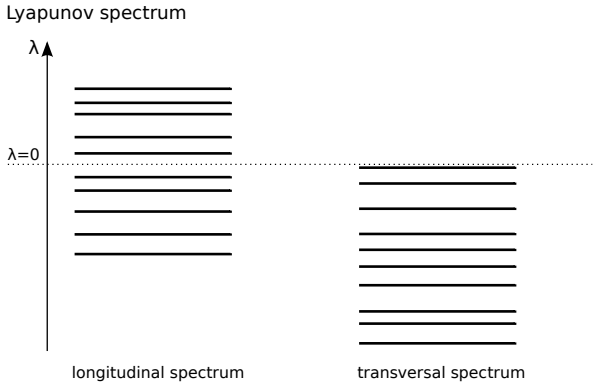

FIGURE 5.2: Sketch of the Lyapunov exponent spectrum close to the synchronization transition. Each bar represents a Lyapunov exponent. The spectrum is grouped into a longitudinal and a transversal part.

where the LE are ordered in decreasing order and M is defined as the largest number for which the sum of LEs is still positive.

For stable synchronization the LE spectrum associated with the longitudinal eigenvalue $\gamma_1 = 1$ has in general positive as well as negative LEs, but all transversal eigenvalues yield only negative LEs. Close to the synchronization transition the maximum LE of (at least) one of these transversal Lyapunov spectra approaches the value zero, as it is depicted in Figure 5.2 and also in Figure 3.7. Consequently, close to the transition these spectra contribute to the KY dimension since negative exponents close to zero are counted as well.

However, this cannot be true. In case of stable synchronization the trajectory of the network, determined by equation (5.2), is completely restricted to the SM. Two neighboring trajectories inside the SM deviate solely from each other according to equation (5.3) with $\gamma_1 = 1$. No transversal eigenvalue contributes to the system's dynamics. By taking all LEs into account when computing the KY dimension, we would consider the phase space outside the SM as well. But this space is not explored by any systems's trajectory and hence does not contribute to the attractor

dimension. We suggest that in case of complete synchronization the definition of the KY dimension, which was originally not meant for such complex systems, needs to be adjusted. The sum in equation (5.4) must only run over the LEs of the γ_1 spectrum since only the longitudinal LE spectrum can contribute to the KY dimension.

In contrast, for the unsynchronized system the phase space perpendicular to the SM is explored as well and the attractor generally stretches across this space. Thus, in the desynchronized regime all eigenvalues contribute to the attractor dimension and all LEs must be taken into account when computing the KY dimension. In this case, the perturbations cannot be decomposed into the eigenmodes of the coupling matrix G since the coefficients of the linearized equations of equation (5.1) depend on each single node. But close to a supercritical transition we expect that the LEs are continuous as a function of σ and the structure of the LEs is still similar to the one inside the SM, as it is for example the case in Figure 3.7.

This implies that the KY dimension must be discontinuous at the transition to chaos synchronization, since for the unsynchronized regime all LEs whereas for the synchronized regime only the longitudinal spectrum needs to be taken into account.

From the LE spectrum we can also calculate the Kolmogorov entropy which has been explained in detail in Section 2.3. It is defined as the sum over all positive LEs

$$K = \sum_l \lambda_l \,, \quad \text{for } \lambda_l > 0 \,. \tag{5.5}$$

Since only positive LEs contribute, the entropy is always defined with the complete spectrum of LEs, hence it does not show a jump at the transition to chaos synchronization. Nevertheless, at the transition at least one additional band of LEs contributes to the entropy and we expect a discontinuous derivative of $K(\sigma)$

The jump in the dimension of the chaotic attractor and the kink in the entropy are general results which should hold for any chaotic network at the transition to chaos synchronization. In the following section the attractor dimensions D_{KY} and D_C as well as the entropy K are calculated for networks of iterated maps. Both dimensions are compared with each other to check whether our theoretical arguments, which lead to the conclusion that the attractor dimension must jump at the transition, hold.

5.2 Iterated Maps

The previous general statement holds not only for differential equations but also for networks of iterated maps with time-delayed coupling. In the following, we investigate the system of coupled maps presented in Section 3.4. We assume the self-feedback and the coupling delay to be identical, $\tau_s = \tau_c = \tau$, such that the system's equations read

$$x^i_{t+1} = (1-\epsilon) f(x^i_t) + \epsilon\kappa f(x^i_{t-\tau}) + \epsilon(1-\kappa) \sum_j^N G_{ij} f(x^j_{t-\tau}) \,. \tag{5.6}$$

The synchronized state is given by

$$s_{t+1} = (1-\epsilon) f(s_t) + \epsilon f(s_{t-\tau}) \,. \tag{5.7}$$

and its stability is determined by the master stability function

$$\xi^k_{t+1} = (1-\epsilon) f'(s_t)\, \xi^k_t + [\epsilon\kappa + \epsilon(1-\kappa)\,\gamma_k]\, f'(s_{t-\tau})\, \xi^k_{t-\tau} \,. \tag{5.8}$$

All variables and parameters have the usual meaning.

For each mode with eigenvalue γ_k one obtains $\tau + 1$ many LEs. The spectrum is in general obtained by a Gram-Schmidt orthogonalization method. In addition, for Bernoulli maps the LE spectrum can also be obtained by solving the according polynomial equation derived from the master stability function due to the constant coefficients. For more details see Section 3.4.1 and 3.5.1.

5.2.1 2 Units System

For the beginning we restrict our investigations to a system of two mutually coupled maps, such that equation (5.6) reduces to

$$x^i_{t+1} = (1-\epsilon) f(x^i_t) + \epsilon\kappa f(x^i_{t-\tau}) + \epsilon(1-\kappa) f(x^j_{t-\tau}) \,, \tag{5.9}$$

with $i, j \in \{1, 2\}$. This setup has the transversal eigenvalue $\gamma_1 = 1$ and the longitudinal eigenvalue $\gamma_2 = -1$, as it was shown in Section 3.4.

Kaplan-Yorke Dimension

The KY dimension for two mutually coupled Bernoulli and tent maps, respectively, is shown in Figure 5.3. The upper curve shows the KY dimension obtained from the complete set of LEs, i.e., the transversal as well as the longitudinal spectrum is taken into account when evaluating equation (5.4). The lower curve uses only the LE spectrum of the SM which is obtained from simulating a single unit. As discussed in the previous section, for physical reasons the lower curve is valid in the synchronized region whereas in the desynchronized region the upper curve is valid. Thus the KY dimension jumps to a lower value when the parameter ϵ is increased above ϵ_c. Note that the total system's dimension gives an upper bound to the KY dimension. If the dynamics is highly chaotic the full phase space is explored by a typical trajectory on the attractor and hence the chaotic attractor stretches out over the full phase space. For the desynchronized system it is $2(\tau + 1)$ and for the SM it is $\tau + 1$.

So far the discontinuous behavior depends merely on theoretical arguments and their interpretation, namely that we have to neglect the transversal LE spectrum in the synchronized regime. With the method used above it is not possible to decide whether in the synchronized case the physically meaningful KY dimension is obtained from the full or only from the longitudinal spectrum. But the qualitative prediction - a jump in the attractor dimension at the synchronization transition - should be valid for any measure of the dimension of the chaotic attractor. Thus, we compute the correlation dimension of the system in the following to compare it to the KY dimension and to check whether the dimension indeed jumps as we argue.

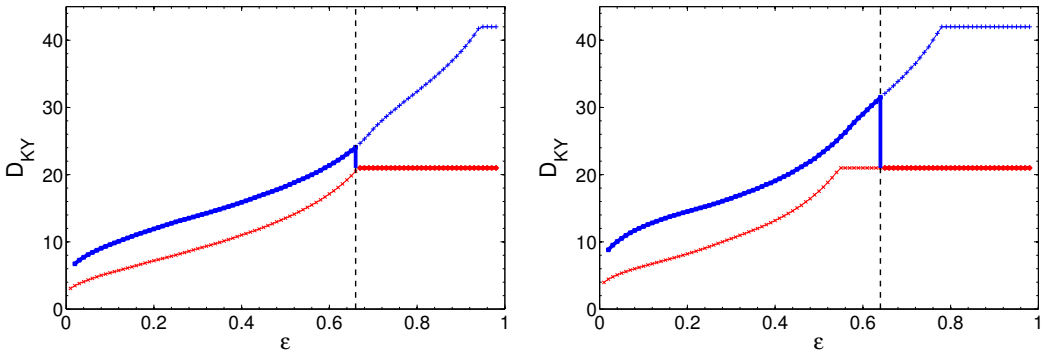

(a) Bernoulli maps (b) Tent maps

FIGURE 5.3: KY dimension D_{KY} with respect to the coupling strength ϵ for a system of two mutually maps. The upper blue line shows D_{KY} of the full system, the lower red line shows D_{KY} of the SM. The vertical dashed line indicates ϵ_c where to its right the system is synchronized. The parameters are $\kappa = 0.25$, $\tau = 20$, $a = 1.5$ for the Bernoulli map and $a = 0.4$ for the tent map, respectively.

Time series analysis – Correlation dimension

The Correlation dimension is computed from a time series of the system, i.e., from the system's trajectories x_t^1 and x_t^2. The transient phase is discarded by only recording the values of the time series after some fixed initial time. For analyzing the time series the TISEAN package of Kantz and Schreiber is used [76]. In particular, the correlation function $C(\xi)$ is computed which scales as a power law $C(\xi) \propto \xi^{D_C}$ with the exponent being the correlation dimension (see Section 2.3).

Figure 5.4 shows a typical plot for the correlation function $C(\xi, m)$ and the correlation dimension D_C where m is the embedding dimension of the auxiliary phase space. For not too small and not too large values of ξ, the correlation function scales clearly according to a power law. To obtain the dimension a straight line is fitted to different correlation functions of different embedding dimensions in a double-logarithmic plot and at the same time the results are cross-checked in plots of the local slopes of the correlation function $d(\xi) = \partial \ln C(\xi)/\partial \ln \xi$ in which the power law behavior corresponds to a plateau. Fitting a horizontal line to the plateau in the local slope is the more reliable approach even though the plateau can be hard to determine. In any case, the correlation function and the local correlation dimension have to be interpreted very carefully and the authors of the TISEAN package strongly discourage from using automatic tools for evaluating the data. For more details on how to compute the correlation dimension the reader is referred to reference [76, 77].

Note that this method allows a reliable calculation of the correlation dimension for small attractor dimensions, i.e., for small values of the delay τ, only - at least for a feasible amount of computation time. For larger system's attractors a longer time series is needed in order for the correlation dimension to be correctly determined. A

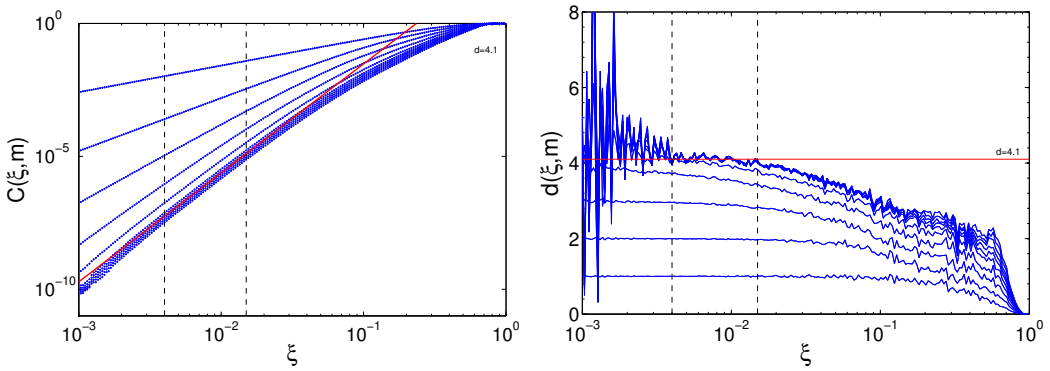

FIGURE 5.4: Correlation function $C(\xi)$ (left) and local slope $d(\xi)$ (right) for different embedding dimensions m (different curves) computed from a time series of a system of two mutually coupled tent maps. The time delay is $\tau = 5$, the length of the time series is $l = 10^6$ and the other parameters are $a = 0.4$, $\epsilon = 0.45$ and $\kappa = 0.35$. Vertical dashed lines indicate the range which was used for the fit.

longer time series increases the computational time and the needed memory capacity for its analysis enormously. The dimension D which can be accurately computed scales approximately with the length N of the time series by $D < 2 \log N$ which means that for an attractor of dimension $D = 20$ a time series of length $N = 10^{10}$ has to be analyzed. Hence, systems with large delays, such as $\tau = 50$, become impractical to solve.

As Figure 5.4 shows, the extrapolation of the slope to low values of the radius ξ is difficult. Hence our values for the correlation dimension give a lower bound to the actual correlation dimension; due to the limited computational power it was not possible to analyze very small values of the distance ξ with an appropriate accuracy.

It is convenient to plot the dimension as a function of κ since the SM, given by equation (5.7), is independent of κ and only changes with the coupling strength ϵ. Thus, the longitudinal LE spectrum and the quantities computed from it such as the Kolmogorov entropy and the KY dimension of the SM are also independent of κ. Figure 5.5 shows results for the correlation as well as the KY dimension. The KY dimension is larger than the correlation dimension in agreement with known theoretical inequalities. For the Bernoulli map the correlation dimension displays a clear jump at the transition to synchronization, in agreement with our theoretical prediction. For the tent map, however, the discontinuity is not clearly visible from our results. As stated above, for small distances ξ the correlation function $C(\xi)$ shows large fluctuations due to the limited statistics. From our results of Figure 5.4 we cannot rule out that the local slopes might not be saturated yet. Thus the obtained results only serve as a lower bound which, according to our results, seems to increase with longer trajectories and better statistics. Consequently, the results of Figure 5.5 do not rule out a discontinuous behavior of the attractor dimension. In any case, the synchronization transition is clearly visible in the discontinuous slope of the correlation dimension.

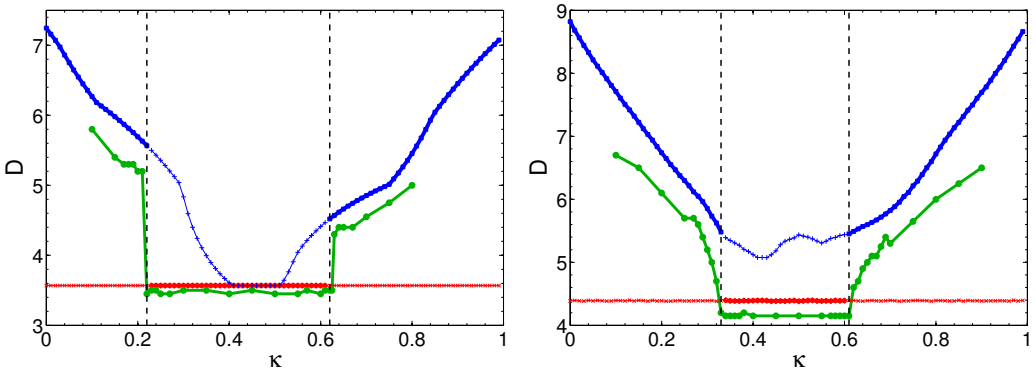

(a) Bernoulli maps (b) Tent maps

FIGURE 5.5: Attractor dimension vs. coupling strength κ for a system of two mutually coupled units. The time delay is $\tau = 5$. The upper blue line shows D_{KY} of the full system, the lower red line shows D_{KY} of the SM corresponding to γ_1 and the green curve in between shows D_C. The vertical dashed lines indicate κ_c. The parameters are $\tau = 5$, $\epsilon = 0.45$, $a = 1.5$ for the Bernoulli map and $a = 0.4$ for the tent map, respectively.

One may argue, that the KY dimension only describes the dimension of typical attractors, see reference [39], and that the sensitivity of the SM to detuning points towards a non-typical attractor. But our theoretical argument - that for synchronization only the transversal spectrum must contributes to the KY dimension - is further confirmed by the fact that for the synchronized system the correlation dimension follows closely the KY dimension only if the transversal spectrum is omitted. Otherwise the KY dimension yields much larger results. The correlation dimension is well defined for the SM and it seems that the corrected KY dimension describes the SM correctly. Hence on top of our theoretical reasoning our numerical results show that in order for the two different definitions of an attractor dimension to coincide we have to exclude the transversal LE spectrum from contributing to the KY dimension for the synchronized state. The completely synchronized state is in some way special.

Note that, in general it may not be obvious which LEs contribute to the KY dimension. For example, if we distort the SM by a nonlinear transformation of one unit the dimension does not change but we do not know which LE have to be omitted in this case. Also, in the case of generalized synchronization the dynamics is restricted to a low dimensional manifold which rules out the majority of LEs. But again, we do not know in advance which LEs have to be omitted from the definition of the KY dimension.

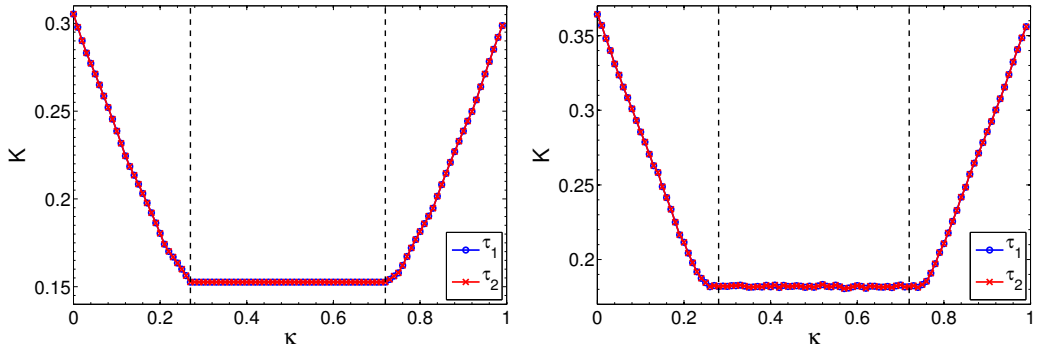

(a) Bernoulli maps (b) Tent maps

FIGURE 5.6: Kolmogorov entropy K vs. coupling strength κ for a system of two mutually coupled units with delay $\tau_1 = 10$ and $\tau_2 = 20$, respectively. K is independent of τ and thus both curves, τ_1 and τ_2, coincide. The vertical dashed lines indicate κ_c. The parameters are $\epsilon = 0.6$, $a = 1.5$ for the Bernoulli map and $a = 0.4$ for the tent map, respectively.

Kolmogorov Entropy

The Kolmogorov entropy, computed from equation (5.5), is continuous at the synchronization transition. In the synchronized region, only the γ_1 band has positive LEs which contribute to the Kolmogorov entropy. Whereas at the synchronization transition the LEs from the other bands suddenly contribute as well and cause a kink in the entropy as a function of feedback strength.

The Kolmogorov entropy for a pair of Bernoulli and tent maps, respectively, is shown in Figure 5.6 for two different delays. As one can see, the Kolmogorov entropy is independent of τ. In Section 3.5 we mentioned that the number of LEs scales with τ (and therefore the number of positive exponents also scales with τ) and that the magnitude of the LEs scales with $\frac{1}{\tau}$ (apart from the anomalous component in case of strong chaos). Both effects cancel each other such that the Kolmogorov entropy does not scale with τ.

In contrast, the KY dimension and therefore the jump of the attractor dimension at the synchronization transition scales with τ since the KY dimension mainly depends on the number of LEs. For more details see Section 5.4.

Cross Correlations

For both maps, Bernoulli and tent, the results for the attractor dimension as well as for the Kolmogorov entropy are very similar. But a qualitative difference between the two models is visible in the cross-correlations, C, and the synchronization probability, ϕ. Figure 5.7 shows C and ϕ with respect to the coupling strength κ for fixed ϵ. At the critical coupling κ_c, i.e., at the synchronization transition both quantities, C and ϕ, jump from a very low level to complete synchronization, $C = \phi = 1$, for a

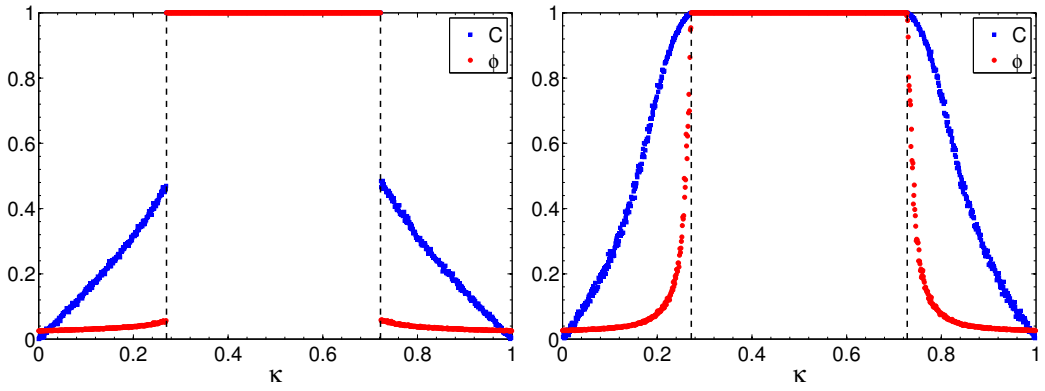

(a) Bernoulli maps (b) Tent maps

FIGURE 5.7: Cross-correlation C (blue squares) and synchronization probability ϕ (red dots) vs. coupling strength κ for a system of two mutually coupled units. The step size is $\Delta\kappa = 10^{-3}$ and the other parameters are $\tau = 20$, $\epsilon = 0.6$, $a = 1.5$ for the Bernoulli map and $a = 0.4$ for the tent map, respectively. The threshold for ϕ was set to $\Theta = 0.01$, i.e., the trajectories were assumed to be synchronized when they were closer together than 1% of their maximum distance.

system of Bernoulli maps, whereas for the tent map C and ϕ increase continuously to $C = \phi = 1$.

The numerical results indicate that the synchronization transition for the Bernoulli map is of subcritical type whereas for the tent map it is of supercritical type [1]. For the Bernoulli map there is at least one stable attractor a good distance away from the SM which becomes unstable at the synchronization transition when the SM becomes stable. For the tent map there is a stable trajectory close to the SM for the nearly synchronized case which merge into the SM at the synchronization transition. Thus, we observe a sudden transition for the Bernoulli map and a smooth transition for the tent map system. Figure 5.8 shows the system's attractor for both models very close to the synchronization transition to display the differences. Note that in both cases, a jump of the KY dimension is predicted due to the bands of LEs.

5.3 Coupled Lasers

An important application of equation (5.1) is the modeling of semiconductor lasers which are coupled by their mutual laser beams. The work presented in this section, in particular the simulations of the laser equations, was mainly performed by Thomas Dahms and is taken from reference [75] with only minor changes. It is a nice extension to the work on iterated maps and relates this work to more realistic systems.

The dynamics of the laser intensity can, to a good approximation, be described by the Lang-Kobayashi rate equations [31]. The Lang-Kobayashi equations describe

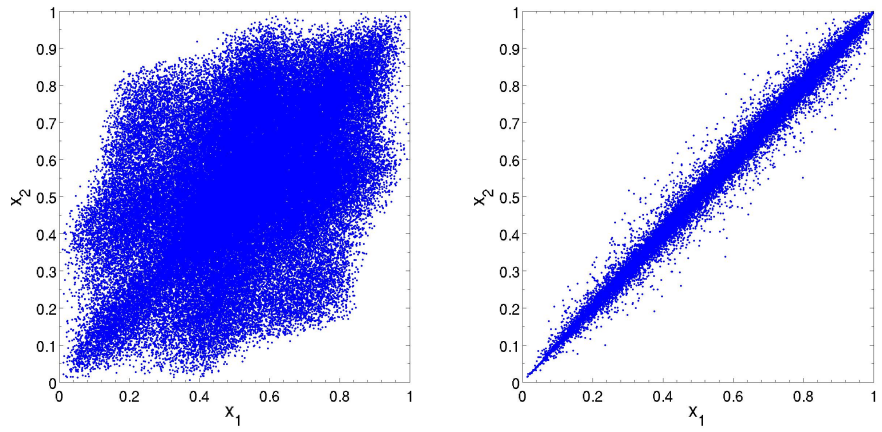

(a) Bernoulli maps (b) Tent maps

FIGURE 5.8: Attractor for a system of two mutually coupled units very close to the synchronization transition. The parameters are $\tau = 20$, $\epsilon = 0.6$, $\kappa = 0.73$, $a = 1.5$ for the Bernoulli map and $a = 0.4$ for the tent map, respectively.

Parameter	Symbol	Value
Linewidth enhancement factor	α	4
Time-scale separation of carrier and photon lifetimes	T	200
Injection current	p	0.1
Coupling strength	σ	0.12
Coupling delay time	τ	100

TABLE 5.1: Parameters for the simulation of the Lang-Kobayashi equations.

the dynamics of a laser with delayed feedback (or delayed coupling) in terms of a slowly varying complex electric field $E(t)$ and a population inversion $n(t)$. For our network of coupled lasers, the corresponding equations of Lang-Kobayashi type in dimensionless form are given by

$$\begin{aligned} \dot{E}^i(t) &= \frac{1}{2}(1+\mathrm{i}\alpha)n^i(t)E^i(t) + \sigma\sum_j G_{ij}E^j(t-\tau) \\ T\dot{n}^i(t) &= p - n^i(t) - \left[1+n^i(t)\right]\left|E^i(t)\right|^2, \end{aligned} \tag{5.10}$$

where $E^i(t)$ is the envelope of the complex electric field and $n^i(t)$ is the renormalized population inversion of the charge carriers of laser i. The model parameters are summarized in Table 5.1. The dimensionless delay time of $\tau = 100$ translates to a delay time of the order of magnitude 1 ns.

A network of coupled lasers modeled by the Lang-Kobayashi equations can be written in the form of equation (5.1), where $x^i(t) = (n^i, Re\left\{E^i\right\}, Im\left\{E^i\right\})$ is now

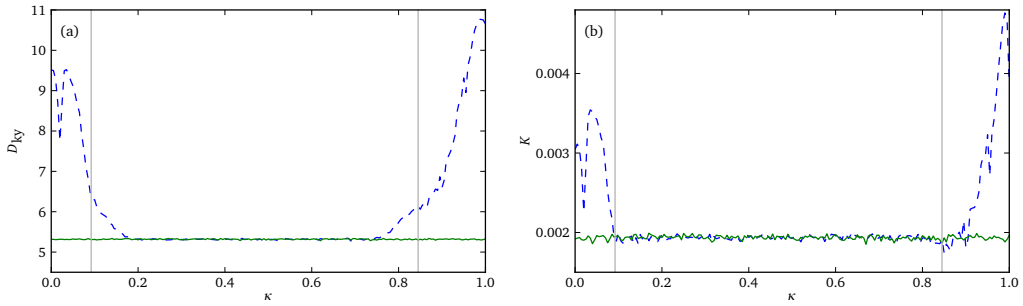

FIGURE 5.9: (a) KY dimension and (b) Kolmogorov entropy of two coupled semiconductor lasers with respect to the relative self-feedback strength κ. The dashed blue and solid green lines are obtained using the complete spectrum and only using the spectrum of the SM, respectively.

three-dimensional and contains the real and imaginary part of the electric field E^i and the charge carrier inversion n^i of the i-th laser. A single laser is not chaotic, but the delayed feedback and/or coupling renders the system chaotic. The linear coupling function H is represented by the matrix $\mathbf{H} = \left(\begin{smallmatrix} 0 & 0 & 0 \\ 0 & 1 & 0 \\ 0 & 0 & 1 \end{smallmatrix}\right)$, corresponding to all-optical coupling as in equation (5.10). In the following we consider a pair of lasers with overall coupling strength σ and self-feedback strength κ, such that the coupling matrix is given by

$$G = \begin{bmatrix} \kappa & 1-\kappa \\ 1-\kappa & \kappa \end{bmatrix} . \tag{5.11}$$

Similar to the iterated maps discussed before, the spectrum of LEs, from which the KY dimension and the Kolmogorov entropy can be computed, is obtained from a Gram-Schmidt orthonormalization procedure. Figure 5.9 shows the KY dimension and the Kolmogorov entropy as a function of κ. The dashed blue curve was obtained using the complete spectrum, while the solid green curve uses only the spectrum of the SM, given by equation (5.2). The vertical gray lines denote the boundary of stable synchronization of the two lasers with the given parameters; synchronization is stable between the two lines.

The results are very similar to the maps. The KY dimension also jumps from a high (dashed blue) to a lower value (solid green) at the synchronization transition.[1] Unfortunately, we are not able to calculate the correlation dimension of the laser rate equations. Due to the delay term which makes the system high-dimensional, the available algorithms do not produce reliable results, to our knowledge. As for the maps, the derivative of the Kolmogorov entropy $K(\kappa)$ is discontinuous at the transition. This is due to the fact that in the desynchronized region, the band of the

[1] Under the assumption that only the spectrum of the SM has to be used when computing the KY dimension for chaos synchronization, whereas outside the synchronization region the complete spectrum has to be used.

longitudinal LEs crosses zero and, hence, suddenly contributes to the Kolmogorov entropy.

5.4 Networks

In this section, we investigate the transition to chaos synchronization in large networks. We are particularly interested in the scaling of the jump in the KY dimension and in the scaling of the Kolmogorov entropy with system size N. For simplicity, we restrict the investigations to networks of N all-to-all coupled Bernoulli units without self-feedback ($\kappa = 0$). The system is described by equation (5.6) where the eigenvalues of the adjacency matrix G, for a network with all-to-all coupling, are degenerated. G has the eigenvalue $\gamma_1 = 1$ and the $N-1$ times degenerated eigenvalue $\gamma_l = -1/(N-1)$, with $l = 2, \ldots, N$. Thus the transversal LE spectrum is $N-1$ times degenerated.

The region of synchronization for an all-to-all coupled network changes with the number of units. In the limit of large delay times, $\tau \to \infty$, we find the critical value at which the transition to synchronization occurs to be (see equation (3.19))

$$\epsilon_c = (a-1)/[a(1-1/(N-1))] \,. \tag{5.12}$$

With increasing system size ϵ_c decreases monotonically towards its limit of $\epsilon = 1-1/a$ for $N \to \infty$, as it is depicted in Figure 5.12(a) by the dashed line. Note that without self-feedback an all-to-all coupled network must comprise at least three units in order for complete synchronization to occur.[2] It is not possible for two mutually coupled units to synchronize without self-feedback, as it is shown in Section 3.4. Figure 5.10 shows the spectrum of LEs as a function of ϵ for a system of three all-to-all coupled Bernoulli maps. The transversal spectrum is two-fold degenerated.

The transition from strong to weak chaos is independent of the number of units and occurs at $\epsilon_{crit} = 1 - 1/a$. It is defined by the scaling behavior of the maximum LE, as shown in Section 3.5.1. For $\epsilon < \epsilon_{crit}$ the system is in the regime of strong chaos, otherwise in the regime of weak chaos. Hence, the transition from strong to weak chaos does generally not coincide with the synchronization transition. The synchronization transition usually occurs for a larger coupling strength. Only in the limit of $N \to \infty$ both transitions coincide.

For strong chaos the maximum LE is of order one whereas for weak chaos it scales as $1/\tau$. Since each mode of the network has τ many LEs of the order of $1/\tau$, the KY dimension increases linearly with the delay time τ whereas the Kolmogorov entropy K is independent of τ. For an unsynchronized system the LEs of the degenerated transversal spectrum contribute to the KY dimension. By adding another all-to-all coupled unit to the system, another identical band of LEs is added which contributes to the KY dimension as well as to the Kolmogorov entropy. Hence, we expect the dimension and entropy to increase with the system size N. On the other hand, for a

[2] The synchronization depends of course on the coupling strength as well as on the chaoticity of the units.

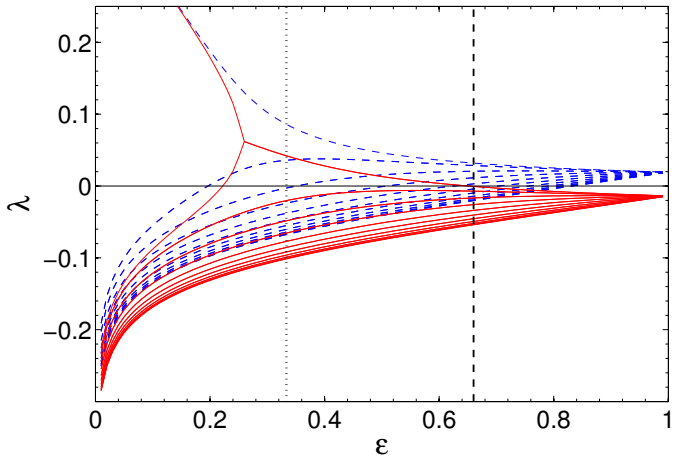

FIGURE 5.10: Lyapunov spectra vs. coupling strength ϵ for a system of three all-to-all coupled Bernoulli maps with the parameters $a = 1.5$ and $\tau = 20$. The blue dashed lines show the longitudinal spectrum associated with $\gamma_1 = 1$ and the red solid lines show the transversal spectrum associated with the two-fold degenerated eigenvalue $\gamma_2 = -1/2$. The vertical dotted line indicates the transition between strong and weak chaos and the vertical dashed line indicates ϵ_c where to its right the system is synchronized.

sufficient coupling strength ϵ such that the system is synchronized, the KY dimension and the Kolmogorov entropy are determined solely by the SM, i.e., only the γ_1 band contributes to the KY dimension and the entropy, and therefore both quantities are independent of the number of units. In particular, the KY dimension cannot exceed a value larger than the delay time of a single unit for the synchronized system.

Figure 5.11 shows the KY dimension and the Kolmogorov entropy as a function of the system size N in the regime of strong chaos for different delay times τ. It is clearly visible that for large delay times the different plots of $D_{KY}/\tau N$ corresponding to different delays nearly coincide. Thus the KY dimension scales linearly with τ whereas the Kolmogorov entropy is independent of τ. Both, entropy as well as dimension increase with system size N and it seems that for large N both quantities scale linearly with N.

Since the KY dimension scales with N for the desynchronized case but it is independent of N for the synchronized case, we expect the jump of the attractor dimension at the synchronization transition to be of the order N. Figure 5.12 shows the jump of the KY dimension at the transition as well as the critical coupling strength ϵ_c at which the jump occurs as a function of network size N for different delay times. The theoretical value for ϵ_c in the limit $\tau \to \infty$ is plotted as well (dashed line). For increasing τ the obtained results for ϵ_c move towards the limiting case. The jump ΔD has a nonmonotonic behavior since the critical coupling ϵ_c at which ΔD is evaluated depends on N. For large enough network sizes the jump ΔD scales indeed linearly with the number of units. The slope of this linear relation is

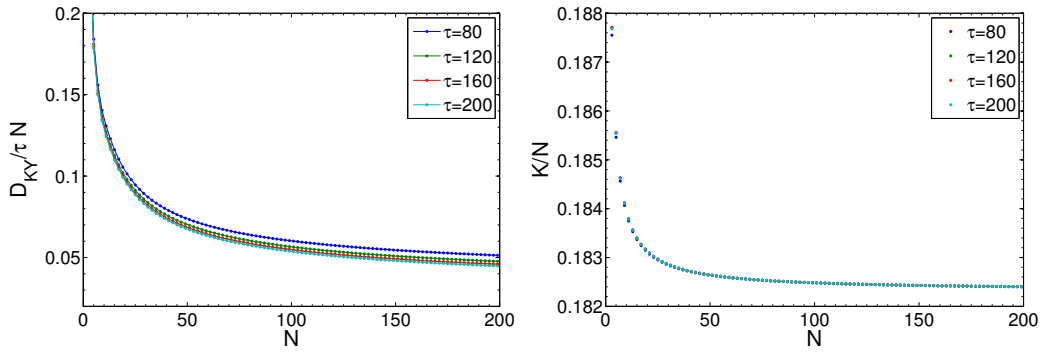

(a) KY dimension D_{KY}

(b) Kolmogorov entropy K

FIGURE 5.11: KY dimension and Kolmogorov entropy with respect to the number of all-to-all coupled Bernoulli maps N for different delay times τ. It starts from $\tau = 80$ (uppermost curve) and increases in steps of $\Delta\tau = 40$ up to $\tau = 200$ (lowermost curve). The other parameters are $a = 1.5$ and $\epsilon = 0.2$.

approximately two for small N, $\Delta D/N \approx 2$, and approximately one for large N, $\Delta D/N \approx 1$. The transition between the two different slopes is related to the dip in the critical coupling strength $\epsilon_c(N)$ which is due to the fact that the system is not yet in the limit $\tau \to \infty$. The slope $\Delta D/N$ depends on the order of limits. If we take the limit $\tau \to \infty$ first the jump ΔD scales linearly with the number of units N with a slope of two. If we however take the limit $N \to \infty$ first it scales with a slope of one for any value of τ. In Figure 5.12(c) the same data as in panel (b) is plotted as $\Delta D/N$ versus N/τ leading to data-collapse. This shows that the jump in the Kaplan-Yorke dimension is in the limit of large τ determined by the scaling law

$$\Delta D \approx N\psi(N/\tau)\,, \tag{5.13}$$

where ψ is the scaling function depicted in panel (c).

5.5 Parameter mismatch

In this section we investigate systems of two mutually coupled non-identical units. These units are either Bernoulli or tent maps with a small parameter mismatch Δa. The system's equations are similar to equation (5.9) and read

$$x^i_{t+1} = (1-\epsilon)f_i(x^i_t) + \epsilon\kappa f_i(x^i_{t-\tau}) + \epsilon(1-\kappa)f_j(x^j_{t-\tau})\,, \tag{5.14}$$

with $i, j \in \{1, 2\}$. Due to the parameter mismatch the dynamics of the two units, given by $f(x_t)$, differ slightly. Hence, identical synchronization is impossible.

A parameter mismatch destroys the SM such that the dynamics of the system is, in contrast to a synchronized system with identical units, never restricted solely to the SM. It does not make sense to speak of a longitudinal and a transversal LE

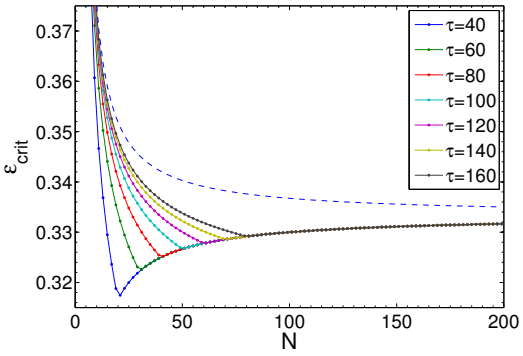

(a) Critical coupling ϵ_c

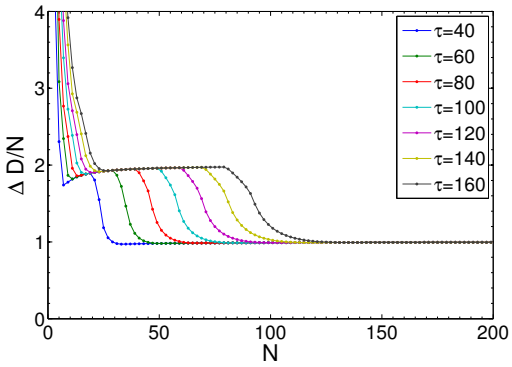

(b) Jump of the KY dimension I

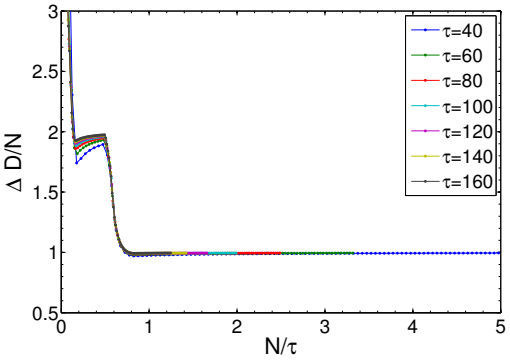

(c) Jump of the KY dimension II

FIGURE 5.12: (a) Critical coupling strength ϵ_c and (b,c) jump of the KY dimension ΔD_{KY} with respect to the system size N of all-to-all coupled Bernoulli maps. The different curves correspond to different delay times, τ. Lowest curve is for $\tau = 40$ and increases by steps of $\Delta\tau = 20$ up to $\tau = 160$ (upper curve). For ϵ_c the theoretical value in the limit of $\tau \to \infty$ is plotted as well (upper dashed line). The parameter of the Bernoulli map is $a = 1.5$.

spectrum anymore. For systems with parameter mismatch we always need to take the full spectrum into account when computing the KY dimension from equation (5.4). Hence, the dimension should not show any discontinuity. Although we cannot group the LEs, they may nevertheless still be clustered in different bands, similar to a desynchronized network of identical units, as discussed earlier. In this case the Kolmogorov entropy shows kinks when some band of negative LEs crosses zero.

The parameter mismatch prevents the system from synchronizing perfectly and gives rise to attractor bubbling, intermittent bursting or basin riddling [60–64, 78, 79]. Depending on the strength of the mismatch, the former synchronized trajectories are usually still nearly synchronized, i.e., they are very close together (in the order of the size of the mismatch), although not identical. But for short periods of time there occur bursts where the system becomes completely desynchronized. The difference of

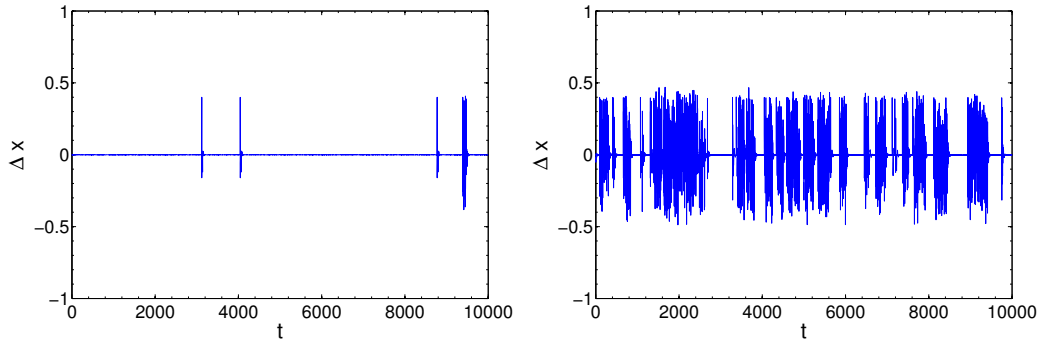

(a) $\Delta a = 0.001$ (b) $\Delta a = 0.01$

FIGURE 5.13: Time series of the difference $\Delta x = x_1 - x_2$ for a system of two mutually coupled Bernoulli maps with parameter mismatch Δa. The parameters are $a = 1.5$, $\epsilon = 0.6$, $\kappa = 0.4$ and $\tau = 20$.

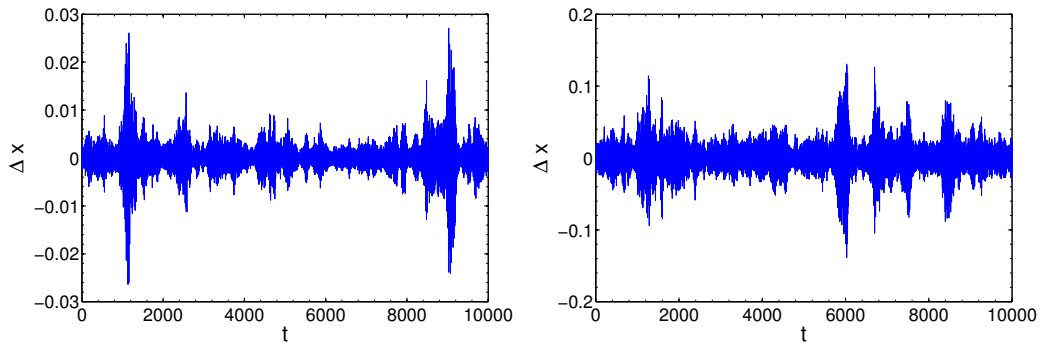

(a) $\Delta a = 0.001$ (b) $\Delta a = 0.01$

FIGURE 5.14: Time series of the difference $\Delta x = x_1 - x_2$ for a system of two mutually coupled tent maps with parameter mismatch Δa. The parameters are $a = 0.4$, $\epsilon = 0.6$, $\kappa = 0.3$ and $\tau = 20$. Note the different scaling of the Δx axis.

the trajectories, $\Delta x_t = x_t^j - x_t^i$, shows an intermittent behavior. The period length between successive bursts decreases with increasing parameter mismatch, i.e., the stronger the mismatch the more frequently bursts occur.

We find that for a Bernoulli system the amplitude of the bursts is independent of the strength of the mismatch whereas for the tent map the amplitude scales with the strengths of the mismatch, in the region where the system with identical units is synchronized. Bernoulli maps show a hard transition whereas tent maps show a soft transition, similar to the super-critical and sub-critical behavior at the synchronization transition of a system without parameter mismatch, as discussed in Section 5.2. A typical time series of a Bernoulli and tent map system is shown in Figure 5.13 and 5.14, respectively, for a set of parameters such that the system without parameter mismatch is completely synchronized.

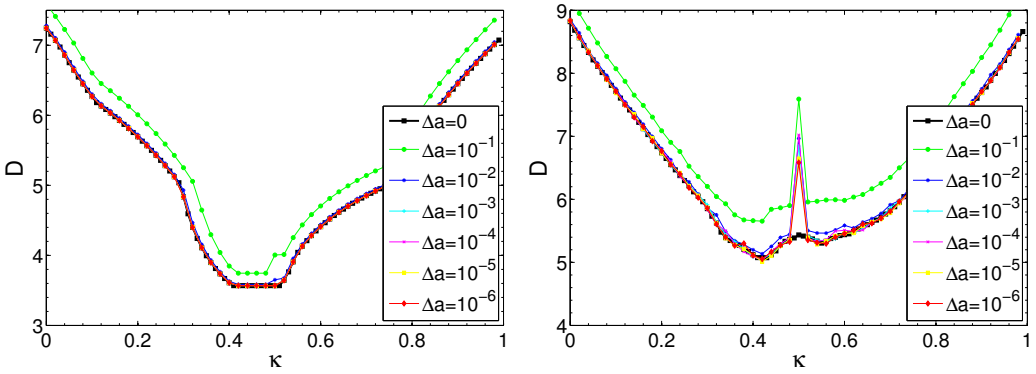

(a) Bernoulli maps, $a = 1.5$

(b) Tent maps, $a = 0.4$

FIGURE 5.15: KY dimension with respect to the coupling strength κ for a system of two mutually coupled maps for various parameter mismatches Δa. The parameters are $a = 1.5$, $\epsilon = 0.45$ and $\tau = 5$.

The parameter mismatch does not change the system's LE spectrum significantly. The KY dimension and the Kolmogorov entropy of a system with parameter mismatch are obtained from the full LE spectrum and are very similar to a system with identical units (when using the full LE spectrum). Only for an extreme parameter mismatch, such as $\Delta a = 0.1$, the dimension and the entropy deviate distinctly. The KY dimension for two mutually coupled Bernoulli and tent maps, respectively, is shown in Figure 5.15 for various parameter mismatches. We find the KY dimension of the system with parameter mismatch to be slightly higher than of a system without parameter mismatch, with the difference depending on the strengths of the mismatch. But the overall shape remains similar. Note that there occurs an outlier in the attractor dimension for coupled tent maps at the symmetric coupling $\kappa = 0.5$ which is due to numerical artifacts. The Kolmogorov entropy for the two systems is shown in Figure 5.16. For Bernoulli maps the Kolmogorov entropy is slightly higher for the system with parameter mismatch, similar to the KY dimension, but follows closely the behavior of the system without mismatch. In particular, the kink in the entropy is still clearly visible. However, for the tent map system the results are not as smooth. The entropy shows quite some fluctuations and can surprisingly, for some parameters, be smaller for a system with mismatch than without mismatch. This behavior is not yet understood. It seems very peculiar since it means that a system with mismatch is more predictable. Most likely the data points which are smaller than the reference system without mismatch are due to random fluctuations caused by the mismatch and numerical inaccuracies. A closer investigation of this problem should be done in the future. The kink in the Kolmogorov entropy is not as distinct as for Bernoulli maps and vanishes for larger parameter mismatches, so that the transition to synchronization is no longer visible.

Figure 5.17 shows the correlation dimension for two mutually coupled maps for various parameter mismatches. The correlation dimension changes drastically for a

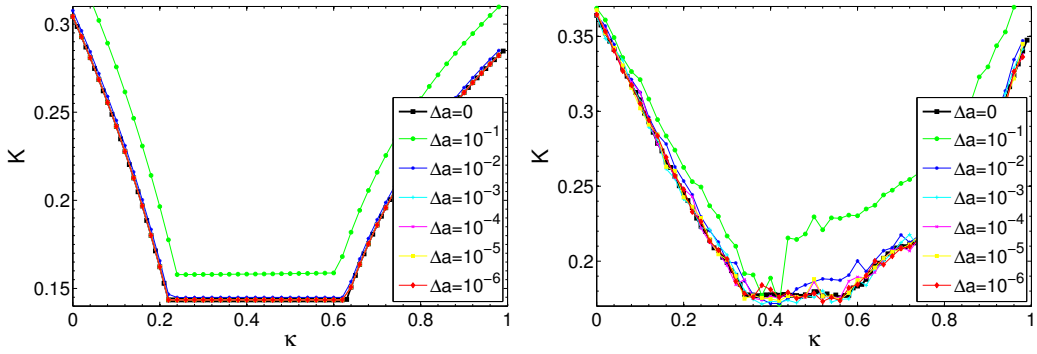

(a) Bernoulli maps, $a = 1.5$ (b) Tent maps, $a = 0.4$

FIGURE 5.16: Kolmogorov entropy with respect to the coupling strength κ for a system of two mutually coupled maps for various parameter mismatches Δa. The parameters are $\epsilon = 0.45$ and $\tau = 5$.

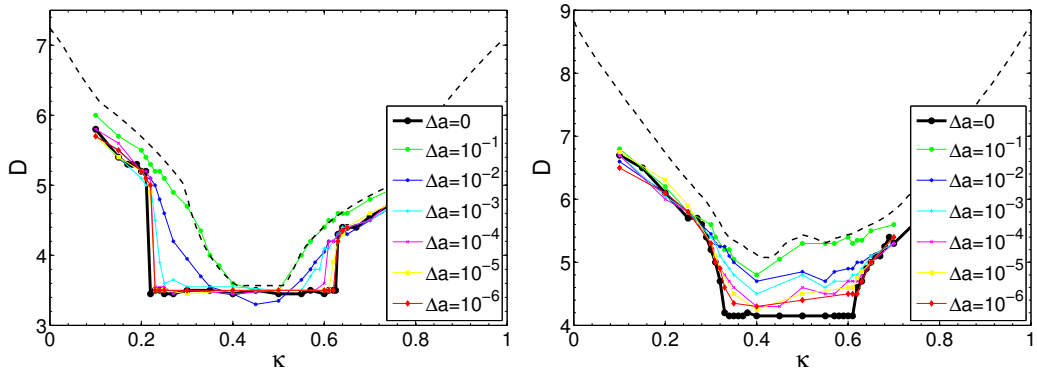

(a) Bernoulli maps, $a = 1.5$ (b) Tent maps, $a = 0.4$

FIGURE 5.17: Correlation dimension with respect to the coupling strength κ for a system of two mutually coupled maps for various parameter mismatches Δa. The parameters are $\epsilon = 0.45$ and $\tau = 5$. The dashed line shows the KY dimension of a system without parameter mismatch, for a better comparison of the correlation dimension with the KY dimensions.

system with parameter mismatch. Without parameter mismatch it follows the KY dimension of the SM in the regime of synchronization, but for an increasing parameter mismatch it more and more follows the KY dimension of the full system (and not the SM). In particular the discontinuity in the correlation dimension vanishes. As we reasoned above, the system with parameter mismatch cannot completely synchronize and hence the dimension of the attractor is determined by the full spectrum.

Chapter 6

Linear Response of Synchronized Chaotic Systems

In this chapter the linear response of synchronized time-delayed chaotic systems to small external perturbations is investigated for iterated maps. We mainly focus on a phenomenon from chaos communication called "chaos pass filter". The external perturbation causes the dynamics of the synchronized chaotic units to deviate leading to a distribution of distances. This distribution is analyzed by means of its moments and is used as a measure of the linear response. The linear response is also quantified by the bit error rate of a transmitted binary message which perturbs the synchronized system.

In the first section the effect of chaos pass filter is explained and the model of two coupled chaotic units is introduced. This model and its response to noisy signals is studied extensively in the following sections. The moments of the distribution of distances are defined and investigated in the second section. In the third section the bit error rate of a transmitted signal is analyzed. In the following two sections we discuss the response of the system to harmonic signals and the relation of the system's Lyapunov spectrum to its response. Finally the linear response of small networks, such as a chain of three units and a ring of four units, is investigated.

Most of the research presented in this chapter has been published in reference [80] and the presentation here follows closely this paper but also contains some additional results and figures.

6.1 Chaos Pass Filter

We showed in Chapter 3 that coupled chaotic systems can synchronize completely without any time shift even if the couplings, i.e., the exchanged signals, have a large time delay. This phenomenon can be applied for chaos based cryptography [81]. Communication by synchronized chaotic electronic circuits [25–27] as well as by synchronized chaotic lasers [28] have been demonstrated in the laboratory. Even in a commercial fiber-optic network, secure communication has been realized with

synchronized chaotic semiconductor lasers over a distance of 120 km [30].

Secure chaos communication is based on the fact that the secret message is encoded in the exchanged chaotic signal such that only the synchronized receiver can reconstruct the message from the transmitted signal. Several methods have been suggested, e.g. chaos modulation where the message modulates the dynamics of the sender or chaos masking where the message is added on top of the transmitted signal [18]. Chaos masking utilizes a phenomenon which was coined "chaos pass filter" and hence is also sometimes referred to as chaos pass filter [82, 83]. A chaotic receiver which is driven by the chaotic trajectory of a sender plus a (small) message responds essentially to the trajectory but not to the message. Thus the chaotic system filters out any perturbation and it is possible for the receiver to recover the message by subtracting its own dynamics from the incoming chaotic signal.

Chaos pass filter is observed in experiments on electronic circuits and lasers and in simulations of chaotic systems. But the underlying physical process is still not well understood. The dynamics of a stable completely synchronized state is restricted to the SM and any random perturbation perpendicular to the manifold exponentially decays to zero. However, the added secret message represents a permanent perturbation of the system which is not necessarily damped but potentially destroys the synchronization. In the following we investigate the phenomenon of chaos pass filter, i.e. the linear response of synchronized chaotic systems to an external perturbation. The linear response is analyzed by means of the moments of the distribution of distances, i.e., the deviations between two synchronized chaotic units, the bit error rate of a transmitted random message and resonances of harmonic perturbations.

Research on linear response of general chaotic systems has been done before, mainly in the context of linear stochastic systems with multiplicative and additive noise [84, 85]. Here, we use iterated maps in order to derive analytical results. Many of the effects discussed in this chapter are also observed in numerical simulations of chaotic differential equations.

6.1.1 The Model

The simplest model for the chaos masking setup is a system of two chaotic units which are either uni- or bi-directionally coupled by a function of their internal variables, similar to the system presented in Section 3.4. The secret message m, which represents an external perturbation, is added to the transmitted chaotic signal at the sender as depicted in Figure 6.1. These setups have been realized with chaotic semiconductor lasers in a laboratory [48, 86, 87]. The message is small compared to the carrier signal and for our purpose its content may be considered as random noise. Hence we are, in the following, interested in the linear response of the receiver to noise.

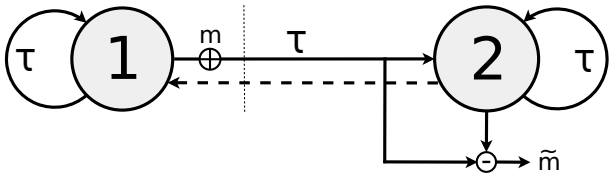

FIGURE 6.1: Setup of two coupled chaotic units with either uni- or bi-directional (dashed line) coupling. A perturbation m is added to the exchanged signal at unit 1, i.e., the sender, and is recovered as $\tilde{m}$ at the receiver. The transmitted signal has a time delay τ.

Uni-directional Setup

The dynamics of the uni-directional setup is given by

$$\begin{aligned} x^1_{t+1} &= (1-\epsilon) f(x^1_t) + \epsilon f(x^1_{t-\tau}) \\ x^2_{t+1} &= (1-\epsilon) f(x^2_t) + \epsilon\kappa f(x^2_{t-\tau}) + \epsilon(1-\kappa) f(x^1_{t-\tau} + m_{t-\tau}) \,, \end{aligned} \tag{6.1}$$

where the parameters have the usual meaning and the chaotic dynamics $f(x)$ is either given by a Bernoulli, tent or logistic map.

The effect of small noise can be calculated by linearizing equation (6.1) in the vicinity of the SM $s_t = x^1_t = x^2_t$. The noise leads to a small deviation $d_t = x^2_t - x^1_t$ which is determined by the linear equation

$$d_{t+1} = (1-\epsilon) f'_t d_t + \epsilon\kappa f'_{t-\tau} d_{t-\tau} + \epsilon(1-\kappa) f'_{t-\tau} m_{t-\tau} \,, \tag{6.2}$$

where f'_t is the derivative of $f(x)$ at the synchronized trajectory s_t.

This equation determines the region of synchronization. Without noise d_t decays to zero for stable synchronization and increases exponentially otherwise. Note that without any noise present, $m_t = 0$, this equation can be solved analytically for Bernoulli units, where $f'_t = a = const$, in the limit of large delay, $\tau \to \infty$, similar to Section 3.4.1. One obtains the system's LE spectrum and hence the phase diagram of synchronization can be determined. The parameter range for which the Bernoulli system in the stationary state synchronizes completely, i.e., $x^1_t = x^2_t$, is given by the inequality

$$\kappa < \frac{1 - a(1-\epsilon)}{a\epsilon} \,, \tag{6.3}$$

and is shown in Figure 6.2. For the uni-directional setup stable synchronization exists in region II and III.

Bi-directional Setup

The system's equations of the bi-directional setup are very similar to the uni-directional one. The only difference is that the receiver's dynamics is injected into

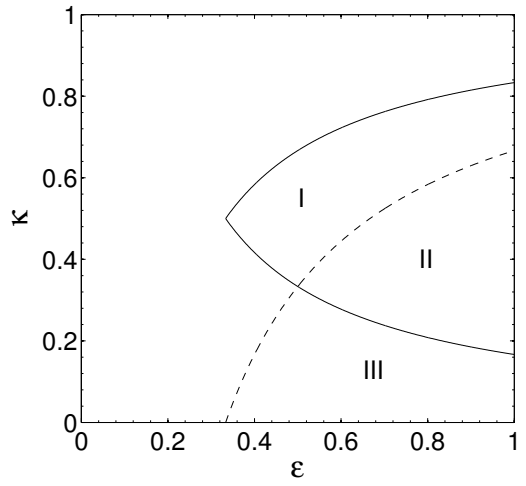

FIGURE 6.2: Phase diagram for two coupled Bernoulli units with $a = 1.5$. The uni-directional setup synchronizes completely in regions II + III (- -) and the bi-directional setup in regions I + II (-), see equation (6.3) and (6.6).

the sender. The equations read

$$\begin{aligned} x^1_{t+1} &= (1-\epsilon) f(x^1_t) + \epsilon\kappa f(x^1_{t-\tau}) + \epsilon(1-\kappa) f(x^2_{t-\tau}) \\ x^2_{t+1} &= (1-\epsilon) f(x^2_t) + \epsilon\kappa f(x^2_{t-\tau}) + \epsilon(1-\kappa) f(x^1_{t-\tau} + m_{t-\tau}) \,, \end{aligned} \tag{6.4}$$

and the linearized equations for a small deviation is given by

$$\begin{aligned} d_{t+1} &= (1-\epsilon) f'_t d_t + \epsilon\kappa f'_{t-\tau} d_{t-\tau} + \epsilon(1-\kappa) f'_{t-\tau} \left(m_{t-\tau} - d_{t-\tau}\right) \\ &= (1-\epsilon) f'_t d_t + (2\kappa - 1)\epsilon f'_{t-\tau} d_{t-\tau} + \epsilon(1-\kappa) f'_{t-\tau} m_{t-\tau} \,. \end{aligned} \tag{6.5}$$

Without noise, $m_t = 0$, we can also compute the synchronization region for a Bernoulli system analytically and obtain the following inequality

$$\frac{a-1}{2a\epsilon} < \kappa < \frac{1 + 2a\epsilon - a}{2a\epsilon} \,. \tag{6.6}$$

This region is shown in Figure 6.2, where stable synchronization for the bi-directional setup exists in region I and II.

6.1.2 Recovering a Secret Message

As explained earlier, for chaos masking the message m is modulated onto the chaotic carrier signal. The combined signal $c_t = x^1_t + m_t$ is finally transmitted. The chaos masks the secret message such that a potential eavesdropper only sees a random signal. Only the receiver which is synchronized to the sender can recover the message by subtracting its own state from the received signal. The recovered message $\tilde{m}_t$ is then given by

$$\tilde{m}_t = c_t - x^2_t = m_t - d_t \,, \tag{6.7}$$

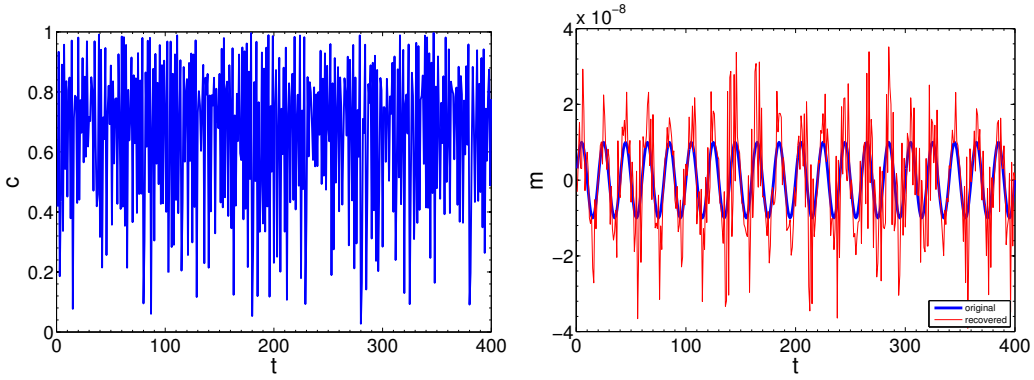

(a) Transmitted signal $c_t = x_t^1 + m_t$ (b) Original and recovered message, m and $\tilde{m}$

FIGURE 6.3: Encoding and decoding of a message in a chaotic signal using chaos masking. System consists of two bi-directionally coupled logistic maps with $a = 4$, $\epsilon = 0.6$, $\kappa = 0.4$ and $\tau = 100$. The message m is modeled as a periodic signal with amplitude $M = 10^{-8}$ and frequency $\omega = 5 \cdot 2\pi/\tau$.

where x_t^1 and x_t^2 denotes the sender's and the receiver's dynamics, respectively. If both units were perfectly synchronized, i.e., $d_t = 0$, the original message would be perfectly recovered by the receiver.

To illustrate the principle of chaos masking, Figure 6.3 shows a typical transmitted signal, i.e., the chaotic carrier signal with a message added, and the original periodic message of the form $m_t = M \sin \omega t$ together with the recovered message. The periodic structure of the message is not apparent in the transmitted signal, which looks like random noise, but is clearly visible in the recovered message.

Note that for the security of the communication it is crucial that the system is high dimensional. For low dimensional chaotic systems tools have been developed to analyze the chaotic signal and extract information from it, such as the technique of return maps [88] or parameter estimation of chaotic equations [89, 90]. Even for high dimensional chaos tools for reconstructing the chaotic attractor exist [91–93]. In particular a uni-directional setup is not secure since an eavesdropper who, for example, knows all the details can use an identical copy of the receiver, synchronize it as well and extract the message. In contrast, two chaotic units which interact by bi-directional transmission have an advantage over an attacker driven by a uni-directional signal [94–98].

6.1.3 Numerical Difficulties

The additional noise in the argument of $f(x)$ in the system equations (6.1) and (6.4), for example in the term $f(x_{t-\tau} + m_{t-\tau})$, can cause the argument, and hence the system's dynamics, to leave the allowed range $[0, 1]$. But the system with its coupling constants is constructed such that the dynamics must be restricted to the range $[0, 1]$. If a unit is not restricted to the unit interval the system's dynamics

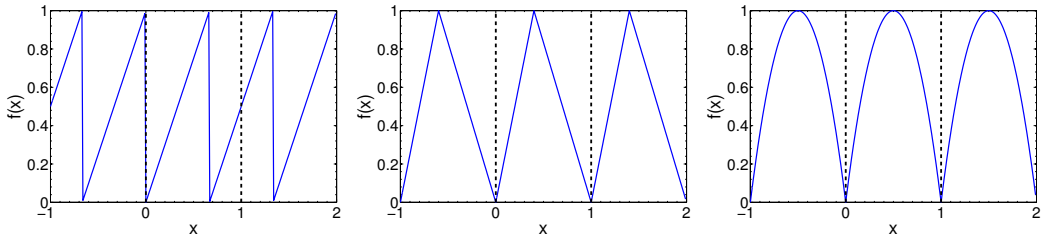

(a) Bernoulli map, $a = 1.5$ (b) Tent map, $a = 0.4$ (c) Logistic map, $a = 4$

FIGURE 6.4: Periodic continuation of the maps.

can quickly diverge to infinity. There are different possibilities to circumvent the problem that the argument can take on values outside the allowed unit interval. To name a few: reflecting boundaries, periodic boundaries, periodic continuation or arguments which are not in the desired range can be rejected and a new random number can be drawn instead, until it finally is in the desired range. In the following periodic continuation was chosen, as it is shown in Figure 6.4. If the argument exceeds the allowed range, the function $f(x)$ is periodically repeated such that the unit's dynamics is restricted to the unit interval.

6.2 Moments of the Distribution of Distances

The linear response of the synchronized system to a small perturbation m, such as noise or a transmitted message, can be studied by investigating the stationary distribution of the distance d_t which develops after a transient time and which is caused by the transversal LEs. Without an external perturbation the coupled system, equation (6.1) and (6.4), can synchronize completely, see Figure 6.2. However, for a slightly perturbed system the deviation from the SM d_t does not decay to zero but has a distribution $\rho(d)$ around zero. This distribution is characterized by its moments which are defined as

$$\chi_n = \lim_{\langle|m|\rangle \to 0} \frac{\langle |d|^n \rangle}{\langle |m|^n \rangle} , \tag{6.8}$$

where $\langle \ldots \rangle$ means an average over the distribution of m and d, respectively and n denotes the order of the moment. In the following we will mainly focus on the second moment χ_2 which is also known as susceptibility. The susceptibility is a measure for the response of the synchronized system to an external perturbation. The larger the system's susceptibility, the stronger is its response to a perturbation.

For our general investigations of the moments of $\rho(d)$ we model the perturbation m_t as random numbers with a uniform distribution in the interval $[-M, M]$. If not stated otherwise, the presented results were obtained using a maximum noise strength of $M = 10^{-8}$. Simulations have also been performed for other maximum noise strengths. We found that the linear response does not change much up to

$M = 10^{-2}$. In particular, all observed phenomena which are presented in this work occur up to this maximum noise strength.

6.2.1 Systems without Time Delay

We start by discussing systems without time delay, $\tau = 0$, in order to obtain analytical results. In particular, we can derive an expression for the second moment for such systems. In contrast, systems with time delay are much more complex and we have to rely on numerical simulations.

Uni-directional Setup

Let us consider the simplest of all cases, the uni-directional setup without time delay. Using the substitution $\alpha = \epsilon(1-\kappa)$ the system reduces to a simple master-slave setup without self-feedback and the linearized equation (6.2) takes the form

$$d_{t+1} = (1-\alpha) f'_t \, d_t + \alpha f'_t \, m_t \, . \tag{6.9}$$

From this equation we see immediately that the perturbed system cannot synchronize completely since the noise term prevents d from decaying to zero. But the perturbed system can still synchronize approximately (having a distance of around the strength of the noise) if the first term in equation (6.9) decays to zero exponentially fast, i.e., when the largest transversal LE of the unperturbed system, λ_{mt}, becomes negative. This LE is given by

$$\lambda_{mt} = \ln(1-\alpha) + \langle \ln |f'| \rangle \, , \tag{6.10}$$

and, hence, the critical coupling for the synchronization transition is

$$\alpha_c = 1 - e^{-\langle \ln |f'| \rangle} \, . \tag{6.11}$$

The linear response can also be derived from equation (6.9). Squaring this equation and using the fact that d, m and f' are uncorrelated, one finds for the second moment

$$\frac{\langle d^2 \rangle}{\langle m^2 \rangle} = \frac{\alpha^2 \langle f'^2 \rangle}{1 - (1-\alpha)^2 \langle f'^2 \rangle} \, . \tag{6.12}$$

The second moment diverges when the denominator becomes zero which occurs at the critical coupling

$$\alpha_2 = 1 \pm \sqrt{\frac{1}{\langle f'^2 \rangle}} \, . \tag{6.13}$$

A distribution with diverging moments has typically a power law tail. This implies, in our case, that rare but large excursions from the SM occur. If the factor $(1-\alpha)|f'_t|$ in equation (6.9) takes on values larger than one d_t can temporarily explode, such

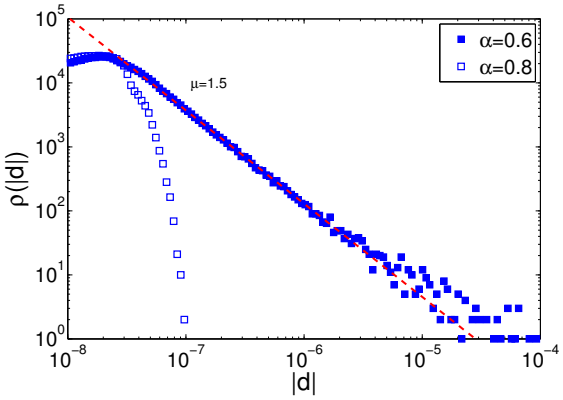

FIGURE 6.5: Distribution of $|d|$ for two uni-directionally coupled logistic maps without time delay $\tau = 0$. $\rho(|d|)$ is shown for two different coupling strengths $\alpha = 0.6$ and $\alpha = 0.8$, respectively, in a log-log plot. The other parameters are $a = 4$ and $M = 10^{-8}$. The dashed red line shows a power law fit with $\mu = 1.5$. The additive noise prevents the system from perfectly synchronizing and therefore the distributions have a maximum at $d \approx 10^{-8}$.

that a nearly synchronized system can indeed have short periods of extreme desynchronization. For example, let us consider logistic maps with $a = 4$, for which the distribution of f' is given by

$$\rho(f') = \frac{1}{\pi\sqrt{16 - f'^2}} \,. \tag{6.14}$$

The maximum slope is $|f'| = 4$ and hence we expect to find large excursions of d_t for $\alpha < \frac{3}{4}$.

The simulations show that the distance $|d|$ indeed follows a power law of the form

$$\rho(|d|) \sim \frac{1}{|d|^{\mu}} \,, \tag{6.15}$$

for a small enough coupling strength. For logistic maps two typical distributions $\rho(|d|)$ are shown in Figure 6.5. Both distributions have a peak at values slightly larger than the maximum noise strength M, since the additive noise in the systems prevents it from being perfectly synchronized. For $\alpha = 0.6$ the distribution follows, to a good approximation, a power law, whereas for $\alpha = 0.8$ the distance $|d|$ is distributed differently.

For the logistic and the tent map the second moment diverges already inside the region of synchronization. For the logistic map with $a = 4$ and the mean values $\langle f'^2 \rangle = 8$ and $\langle \ln |f'| \rangle = \ln 2$, which can be analytically computed from the distribution given by equation (6.14), we find the synchronization transition to be at $\alpha_c = \frac{1}{2}$ and the second moment to diverge at $\alpha_2 = 1 - \frac{1}{\sqrt{8}} \approx 0.646$. For the tent map with $a = 0.4$ where $\langle f'^2 \rangle = 1/a + 1/(1-a) = \frac{25}{6}$ and $\langle \ln |f'| \rangle = -a \ln |a| - (1-a) \ln |1-a| \approx$

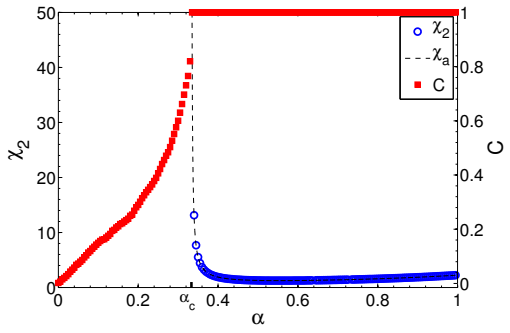

(a) Bernoulli maps, $a = 1.5$

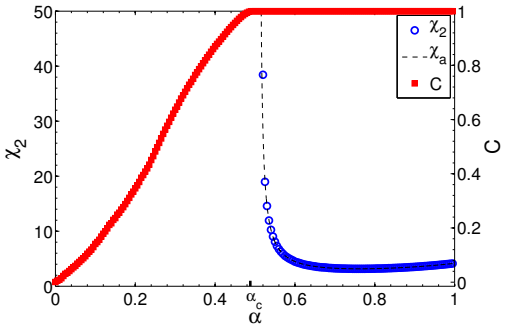

(b) Tent maps, $a = 0.4$

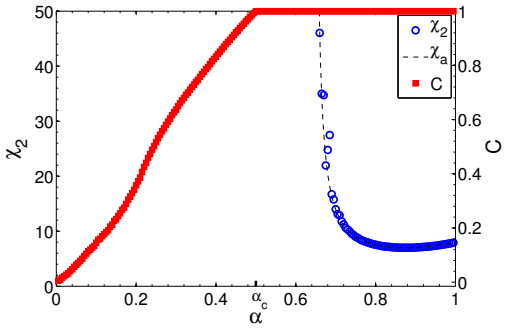

(c) Logistic maps, $a = 4$

FIGURE 6.6: Second moment χ_2 (blue points) and cross correlation C (red squares) for two uni-directionally coupled maps without time delay $\tau = 0$ as a function of the coupling strength α. The maximum noise strength is $M = 10^{-8}$. Dashed curve shows analytical results for χ_2 whereas other results were obtained from simulations.

0.67, we find $\alpha_c \approx 0.49$ and $\alpha_2 = 1 - \sqrt{\frac{6}{25}} \approx 0.51$. In contrast, for Bernoulli maps, where the coefficients f' in equation (6.9) are constant, the transition from a finite to a diverging second moment coincides with the synchronization transition, which takes place at $\alpha_c = \alpha_2 = \frac{1}{3}$ for $a = 1.5$.

The second moment χ_2 is shown in Figure 6.6 together with the cross-correlation C for a system of coupled Bernoulli, tent and logistic maps as a function of the coupling strength. The numerically obtained results for the second moment and the synchronization transition agree well with the analytical results obtained from equation (6.10) and (6.12). For Bernoulli maps the second moment diverges at the synchronization transition whereas for tent as well as logistic maps the second moment already diverges in the region of synchronization.

Figure 6.7 shows a trajectory of d_t for tent maps where the coupling parameters are once chosen such that the second moment exists and once that it diverges. In both cases the system is synchronized, i.e., $C = 1$, but in case of a diverging second moment large excursions from the SM occur. The trajectory shows an intermittent behavior similar to the one in Section 5.5 where systems with parameter mismatch

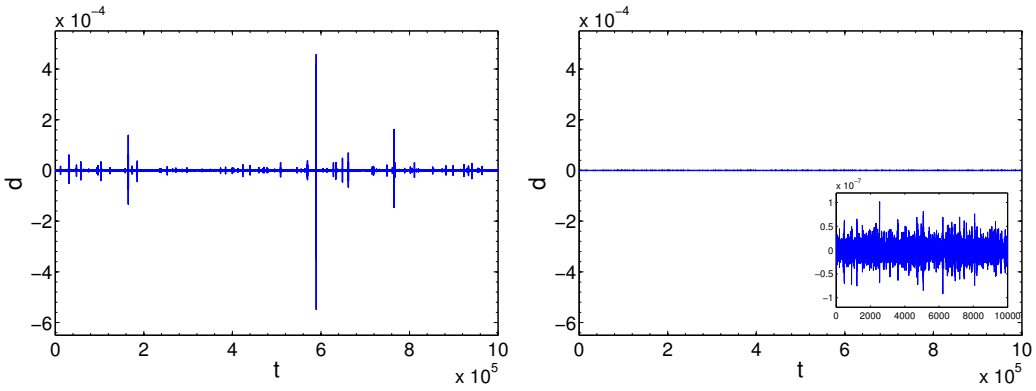

(a) $\alpha = 0.5$ (b) $\alpha = 0.55$

FIGURE 6.7: Trajectory of d_t for two uni-directionally coupled tent maps without time delay $\tau = 0$ and two different coupling strengths α. Other parameters are $a = 0.4$ and $M = 10^{-8}$. In both cases the cross-correlation is $C = 1$ but for (a) large excursions from the SM occur and the second moment diverges, $\chi_2 = 275127$, whereas for (b) the second moment is finite, $\chi_2 = 8$. Inset in (b) shows that the deviations from the SM is in the order of the magnitude of the noise.

were discussed. On the contrary, for a finite second moment the deviations from synchronization are mainly determined by the additive noise term in equation (6.9) and are of the magnitude of M. Note that when plotting the distribution $\rho(|d|)$ of the trajectories we obtain similar results to Figure 6.5. The intermittent trajectory has a power law distribution whereas the other trajectory is distributed differently. On the other hand, we find similar results to Figure 6.7 for typical trajectories of a logistic map setup.

The linear equation (6.9) also determines higher moments of $\rho(d)$. By taking the nth power of equation (6.9) we find that χ_n diverges at a coupling α_n given by

$$1 = (1 - \alpha_n)^n \langle f'^n \rangle \, . \tag{6.16}$$

Hence, for Bernoulli maps all moments diverge at the synchronization threshold α_c, whereas for tent and logistic maps all moments diverge at different coupling strengths α_n. In case of logistic maps this critical coupling is given by

$$\alpha_n = 1 - \frac{1}{4} \left(\frac{n\sqrt{\pi}\,\Gamma(\frac{n}{2})}{2\,\Gamma(\frac{n+1}{2})} \right)^{\frac{1}{n}} \, , \tag{6.17}$$

and it is shown in Figure 6.8. Starting from a highly synchronized state and decreasing α the distribution $\rho(d)$ broadens and eventually follows a power law. The different moments of the distribution successively start to diverge starting with the highest one χ_∞ and continuing with lower and lower ones until finally for $n \to 0$ the synchronization threshold is reached, where $\langle \ln |d| \rangle$ diverges.

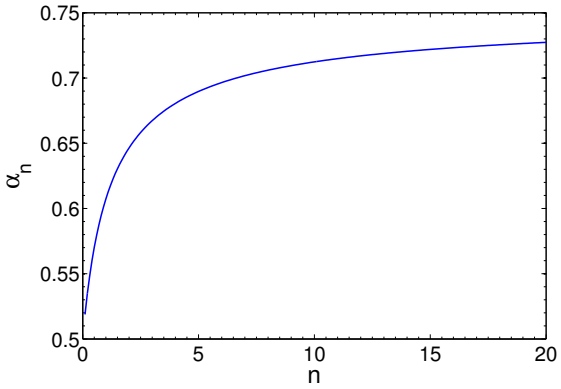

FIGURE 6.8: The threshold α_n below which χ_n diverges for two uni-directionally coupled logistic maps without time delay $\tau = 0$ and $a = 4$, see equation (6.17).

The broadening of the distribution with decreasing α is related to a decreasing power law exponent μ. The linear equation (6.9) can approximately be related to a stochastic equation with multiplicative and additive noise. For chaotic maps, such as the logistic and the tent map, and without time delay present, we can approximately assume f'_t to be an uncorrelated random number. Using this assumption, equation (6.9) becomes a discrete linear stochastic equation with multiplicative and additive noise of the form

$$x_{t+1} = \gamma_t x_t + \eta_t \,. \tag{6.18}$$

In the theory of discrete linear stochastic equation it is well known that such an equation may lead to stationary distributions which have a power law of the form given by equation (6.15) and the exponent μ being determined by [85, 99, 100]

$$\langle \gamma^{\mu-1} \rangle = 1 \,. \tag{6.19}$$

Comparing equation (6.16) and (6.19) we see that μ is related to the order of the moment n by $\mu = n + 1$. This relation determines the smallest value n_c for which all higher moments $n > n_c$ diverge. Note that the zero correlation assumption only holds approximately. When comparing the exponent μ obtained from simulations (see Figure 6.5) with equation (6.19) we find small deviations. But the approximation of uncorrelated random numbers shows qualitatively how power law tails emerge from time dependent chaotic coefficients and, in particular, illustrates that large excursions from the SM are closely related to multiplicative noise. The zero correlation assumption and the stochastic equation approximation is discussed further in Section 6.2.3.

Power law tails of the distribution of a stochastic process with multiplicative and additive noise have been discussed in the context of chaos synchronization, before [1]. In the vicinity of the synchronization transition this phenomenon has been called "on-off intermittency". Here the phenomenon is triggered by the message transmitted

via the chaotic signal, and it is observed deep inside the region of synchronization. Similar to a parameter mismatch, external noise leads to attractor bubbling which prevents the system from synchronizing perfectly and gives rise to an intermittent bursting [61, 101].

Bi-directional Setup

So far we have discussed the uni-directional setup only. The linearized equations for the bi-directionally coupled system without time delay are very similar. With the substitution $\alpha = \epsilon(1-\kappa)$, they read

$$d_{t+1} = (1-2\alpha) f'_t d_t + \alpha f'_t m_t \,. \tag{6.20}$$

From this equation the second moment can be derived and it yields

$$\frac{\langle d^2 \rangle}{\langle m^2 \rangle} = \frac{\alpha^2 \langle f'^2 \rangle}{1-(1-2\alpha)^2 \langle f'^2 \rangle} \,, \tag{6.21}$$

which only differs by the factor of 2 in the denominator compared to the second moment of the uni-directional setup (compare equation (6.12)). For the critical coupling at which the second moment diverges we obtain the following expression

$$\alpha_2 = \frac{1}{2}\left(1 \pm \sqrt{\frac{1}{\langle f'^2 \rangle}}\right) \,. \tag{6.22}$$

The maximum transversal LE of the unperturbed system, which determines the stability of synchronization, is given by

$$\lambda_{mt} = \ln|1-2\alpha| + \langle \ln|f'| \rangle \,. \tag{6.23}$$

Due to the additional factor of 2 in $\ln|1-2\alpha|$ we have to distinguish the two cases, $\alpha < 0.5$ and $\alpha > 0.5$. We find for the critical coupling at which the synchronization transition occurs

$$\alpha_c = \frac{1}{2}\left(1 \pm e^{-\langle \ln|f'| \rangle}\right) \,. \tag{6.24}$$

In the synchronized case, the system's dynamics is restricted to the SM and corresponds to the dynamics of a single unit. Hence, for the synchronized system without time delay the distribution of a single isolated unit can be used for computing the mean values $\langle f'^2 \rangle$ and $\langle \ln|f'| \rangle$. They yield the same values as for the uni-directional setup. A typical distribution $\rho(f')$ for the receiver of two synchronized bi-directionally coupled logistic maps without time delay is shown in Figure 6.9(a). It indeed agrees with the distribution of a single logistic map given by equation (6.14).

The second moment for a Bernoulli, tent and logistic maps system is shown in Figure 6.10. Plotted are results obtained from numerical simulations together with analytical results which were obtained using $\rho(f')$ of a single unit. Only for logistic

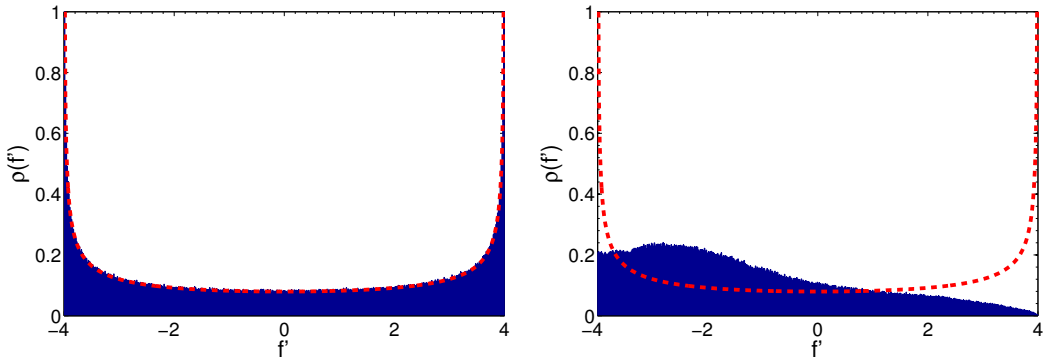

(a) Undelayed bi-directional setup (b) Delayed uni-directional setup

FIGURE 6.9: Probability distribution $\rho(f')$ of the receiver of coupled synchronized logistic maps for an undelayed bi-directional setup (a) with $\epsilon = 0.4$ and $\tau = 0$ and a time-delayed uni-directional setup (b) with $\epsilon = 0.7$ and $\tau = 100$. Other parameters are $a = 4$, $\kappa = 0$ and $M = 10^{-8}$. Dashed red line shows the distribution of a single logistic map given by equation (6.14).

maps, the simulations deviate slightly from the analytical results at the transition from finite to diverging second moments. The deviation can be explained by the fact, that for the simulations there is a cut off at the maximum distance of $d = 1$, whereas for the analytical expressions the distance d can be arbitrarily large.

As for the uni-directional setup, the second moment already diverge within the region of synchronization for logistic and tent maps whereas for Bernoulli maps the second moment diverges at the synchronization transition. With increasing coupling, the influence of the noise term becomes stronger and, hence, the susceptibility is not symmetric around $\alpha = 0.5$.

6.2.2 Systems with Time Delay

In the general case described by the linear equations (6.2) and (6.5) for the uni and bi-directional setup, respectively, a time delay τ is present. The trajectory d_t exhibits distinct auto-correlations at integer multiples of τ, as it is exemplary shown in Figure 6.11 for a uni-directional setup. Hence d_t and $d_{t-\tau}$ cannot be considered independent but are related by the auto-correlation factor A_τ such that

$$\langle d_t d_{t-\tau} \rangle = A_\tau \langle d^2 \rangle \,. \tag{6.25}$$

Using this factor the second moment yields

- uni-directional setup

$$\frac{\langle d^2 \rangle}{\langle m^2 \rangle} = \frac{\epsilon^2 (1-\kappa)^2 \langle f'^2 \rangle}{1 - 2\kappa(\epsilon - \epsilon^2) A_\tau \langle f' \rangle^2 - \left((1-\epsilon)^2 + \epsilon^2 \kappa^2\right) \langle f'^2 \rangle} \,, \tag{6.26}$$

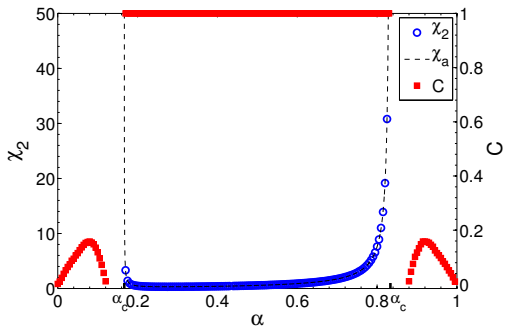

(a) Bernoulli maps, $a = 1.5$

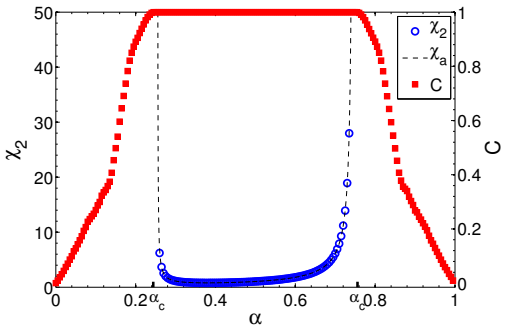

(b) Tent maps, $a = 0.4$

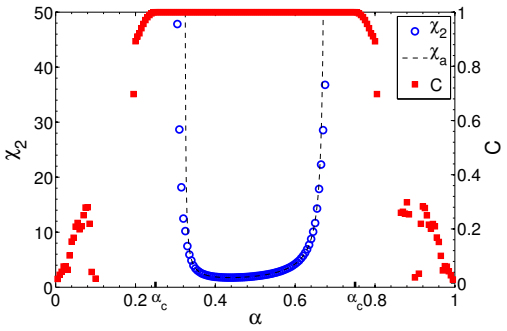

(c) Logistic maps, $a = 4$

FIGURE 6.10: Second moment χ_2 (blue points) and cross correlation C (red squares) for two bi-directionally coupled maps without time delay $\tau = 0$ as a function of α. The maximum noise strength is $M = 10^{-8}$. Dashed curve shows analytical results for χ_2 where the single unit approximation has been used. Other results were obtained from simulations.

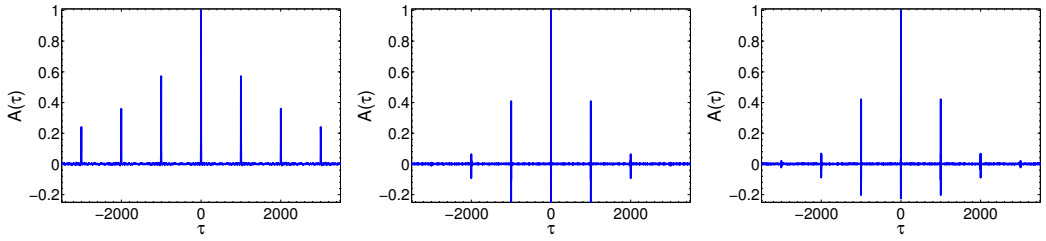

(a) Bernoulli map, $a = 1.5$ (b) Tent map, $a = 0.4$ (c) Logistic map, $a = 4$

FIGURE 6.11: Auto correlation $A(\tau)$ of d_t for two uni-directionally coupled maps with $\epsilon = 0.7$, $\kappa = 0.4$, $\tau = 1000$ and $M = 10^{-8}$.

- bi-directional setup

$$\frac{\langle d^2 \rangle}{\langle m^2 \rangle} = \frac{\epsilon^2 (1-\kappa)^2 \langle f'^2 \rangle}{1 - 2(2\kappa - 1)(\epsilon - \epsilon^2) A_\tau \langle f' \rangle^2 - \left((1-\epsilon)^2 + \epsilon^2 (2\kappa - 1)^2\right) \langle f'^2 \rangle} \,. \tag{6.27}$$

Unfortunately, we generally do not know the factor A_τ, i.e., the magnitude of the correlation between d_t and $d_{t-\tau}$, which also changes for varying coupling parameters. Additionally, the distribution of f' is altered tremendously for a time delayed system compared to the distribution of a single unit, see Figure 6.9(b). Hence, we cannot evaluate equations (6.26) and (6.27) further (not even for Bernoulli maps) but have to rely on numerical simulations for computing the second moment.

A numerical investigation of the time delayed system shows that the behavior of the moments is similar to a system without time delays. For Bernoulli maps all moments diverge at the synchronization threshold whereas for logistic and tent maps the second moment already diverges inside the region of synchronization. Numerical results for systems of two uni-directionally and bi-directionally coupled Bernoulli, tent and logistic maps, respectively, are shown in Figure 6.12. The results are presented in a binary plot, where the system is assumed to be synchronized when the cross correlation exceeds some threshold θ_c, and the second moment is assumed to be finite when it is smaller than some threshold θ_2.

6.2.3 Simulations of the Linearized Equations with Logistic Distributed Noise

In the previous sections we approximately assumed the variable f' in the linearized equations (6.2) and (6.5) to be an uncorrelated random number with a specific probability distribution. Using this approximation the linearized equations become stochastic equations with multiplicative and additive noise, see equation (6.18), which can lead to a power law behavior. Rare but large events, which scale according to a power law, are indeed observed for a certain range of coupling strengths.

The simplest coupling scheme, a uni-directionally coupled system without self-feedback, is a master-slave setup. In case of synchronization the receiver follows the

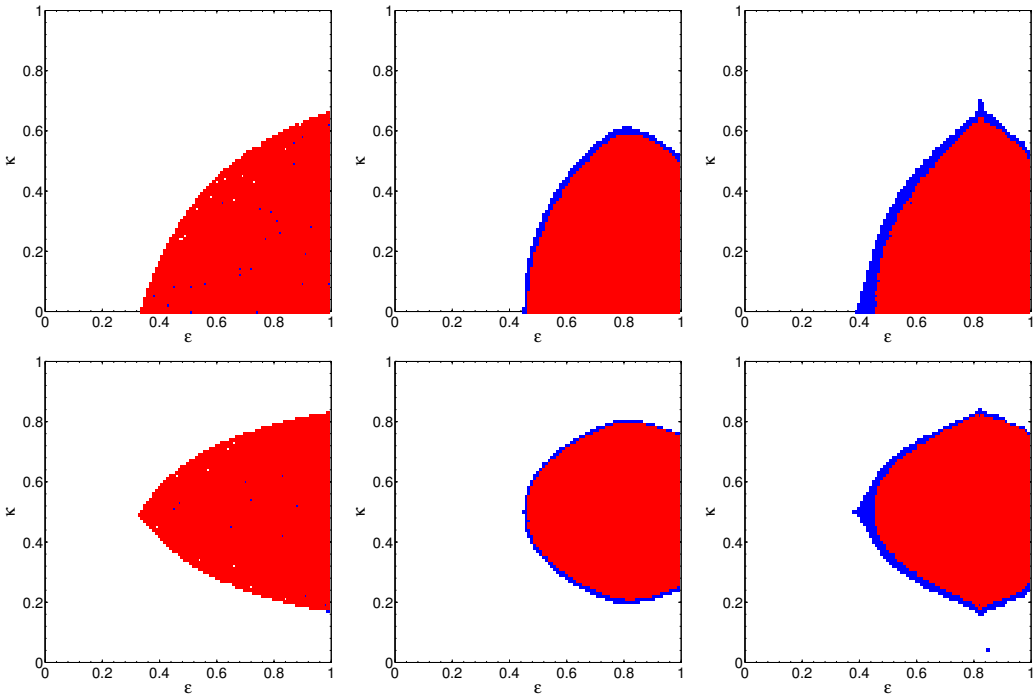

(a) Bernoulli map, $a = 1.5$ (b) Tent map, $a = 0.4$ (c) Logistic map, $a = 4$

FIGURE 6.12: Phase diagram for two uni-directionally (upper row) and bi-directionally (lower row) coupled maps with $\tau = 100$ and $M = 10^{-8}$. Red shows the region where the system is synchronized and has a finite second moment, i.e., C is larger than a threshold $\theta_c = 0.999$ and χ_2 smaller than a threshold $\theta_2 = 50$. Blue shows the region where the system is synchronized but has a diverging second moment, i.e., $C > \theta_c$ and $\chi_2 > \theta_2$.

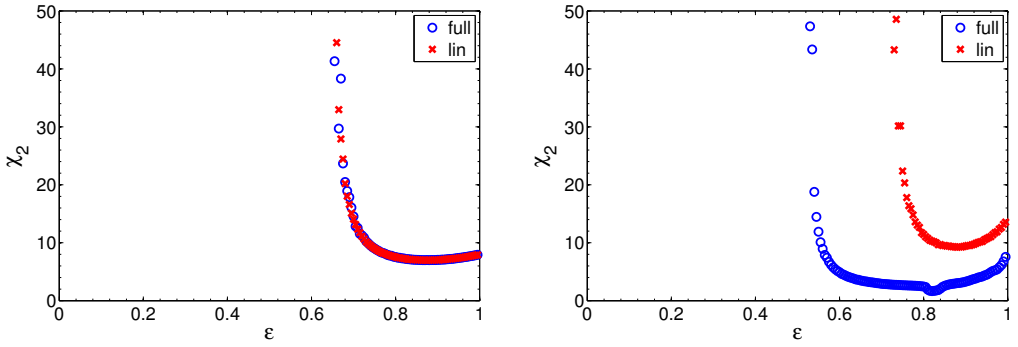

(a) $\kappa = 0$, $\tau = 0$ (b) $\kappa = 0.3$, $\tau = 100$

FIGURE 6.13: Second moment χ_2 for two uni-directionally coupled logistic maps obtained from simulations of the full systems equations and of the linearized equations. For the linearized equations f' was approximated as a random number with the distribution $\rho(f')$ according to equation (6.14). The parameters are $a = 4$ and $M = 10^{-8}$.

dynamics of the sender whereas for the unsynchronized case both units are hardly correlated. Thus, the distribution of f' of both units is essentially the one of a single isolated unit. For a single logistic unit the distribution $\rho(f')$ is known and is given by equation (6.14).

In this section we simulate the linearized equations (6.2) and (6.5) but substitute f' by random numbers which are distributed according to equation (6.14). For more information on how to obtain random numbers with a desired distribution see Appendix A. The results of these simulations are compared to results from simulations of the full system. If our assumption, that the variable f' in the linearized equations is an uncorrelated random number, holds we expect the results of the different simulations for the master-slave setup to coincide perfectly. For the general case where the units are influenced by a delayed (mutual) interaction we expect the results of the simulations to deviate, since in this case the distribution $\rho(f')$ is altered and does not correspond to the one of a single isolated unit.

Figure 6.13 shows results for a uni-directional setup. For $\tau = 0$ the results from simulations of the linearized equation match well with the results from the full equations whereas for a system with delayed feedback the curves deviate, as we expected.

Figure 6.14 shows results for a bi-directional setup. As stated earlier and as it is shown in Figure 6.9, the distribution $\rho(f')$ of an undelayed synchronized bi-directionally coupled system corresponds to the distribution of a single unit. As the plots show, for $\tau = 0$ the results from simulations of the linearized equation match reasonably well with the results from the full equations. However for a time delayed system the distribution is altered completely and the zero correlation assumption is no longer valid. For $\tau \neq 0$ the results of the simulations deviate strongly, similar to the uni-directional setup.

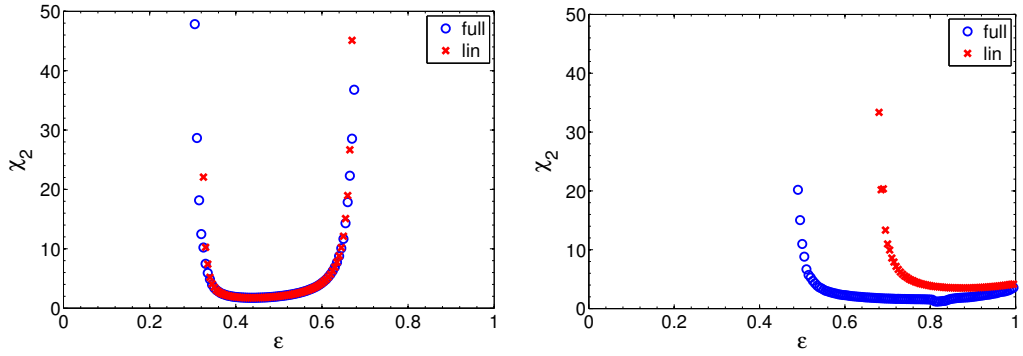

(a) $\kappa = 0$, $\tau = 0$ (b) $\kappa = 0.4$, $\tau = 100$

FIGURE 6.14: Second moment χ_2 for two bi-directionally coupled logistic maps obtained from simulations of the full systems equations and of the linearized equations. For the linearized equations f' was approximated as a random number with the distribution $\rho(f')$ according to equation (6.14). The parameters are $a = 4$ and $M = 10^{-8}$.

6.3 Bit Error Rate

In this section we mainly focus on the external perturbation being a transmitted message. Hence, it is not modelled as uniform distributed noise but as discrete binary noise of the form $m_t = \pm M$ with $M \ll 1$ and $\langle m \rangle = 0$. The quality of the transmission and reconstruction of a binary message is measured by the bit error rate (BER).

As mentioned in Section 6.1.2, for a proper reconstruction of the transmitted message it is crucial that the system is synchronized. However, the message is an external perturbation to the system that potentially destroys the synchronization. Hence the BER tells us how an external perturbation influences the synchronization, i.e., it is an indirect measure of the linear response.

The BER r is defined as the the number of incorrectly recovered bits normalized by the total number of received bits,

$$r = \frac{\#\text{ incorrectly recovered bits}}{\#\text{ received bits}} . \tag{6.28}$$

In order to reconstruct a binary message successfully it is sufficient that the recovered messages $\tilde{m}_t$ has the same sign as the original message, i.e., $m_t \tilde{m}_t > 0$. Note that by just guessing the bits we would be correct in half of the cases on average and hence obtain $r = 0.5$.

The BER is related to the distance d by an integral over the distribution $\rho(d)$,

according to

$$r = \frac{1}{2}\left(\int_{-\infty}^{-M} \rho(d)\,\mathrm{d}d + \int_{M}^{\infty} \rho(d)\,\mathrm{d}d\right) = \frac{1}{2}\left(1 - \int_{-M}^{M} \rho(d)\,\mathrm{d}d\right) . \tag{6.29}$$

It is the probability for the absolute value of the distance to be larger than the binary signal, i.e., $|d| > M$, normalized by the factor $1/2$. If $|d| > M$, the distance will be in the direction of M in half of the cases and in the opposite direction in the other half. Thus the sign of the recovered signal is changed in half of the cases. This amounts for the factor $1/2$. If the distance is smaller than M, the sign is not changed and thus the signal can be recovered correctly with probability 1.

Note that this definition of the BER assumes that the system has relaxed to a stationary distribution $\rho(d)$. In fact, this definition may be only an upper bound since lower BERs may be achievable if one uses additional information about the transmitted signals [102].

For computing the BER analytically by evaluating equation (6.29) we need to know the probability distribution of the distances, $\rho(d)$. Unfortunately $\rho(d)$ is only known in a few special cases. In general we have to rely on computer simulations to determine the BER.

6.3.1 Systems without Time Delay

The BER for systems without time delay is shown in Figure 6.15. It shows results obtained from simulations of Bernoulli, tent and logistic maps for the uni- as well as the bi-directional setup.

For an unsynchronized system the BER is at its maximum $r = 0.5$. In contrast to the second moment which becomes finite at the synchronization transition only for Bernoulli maps, the BER drops down to smaller values for all maps as soon as the system synchronizes. That means that the BER is smaller than $r = 0.5$ although d has large excursions from the SM and the second moment diverges. Hence the sign of the deviation has correlations to the original message even though its amplitude has still a broad distribution. In this parameter range information can already be successfully transmitted. Although the BER is very high, one may apply methods from information theory to derive the message. For the bi-directional Bernoulli setup without time delay it is shown in Appendix B that the absolute values of the distances are smaller than the message amplitude, $|d| < M$, in the interval $\frac{1}{3} \leq \epsilon \leq \frac{5}{9}$ and hence the BER becomes zero, see Figure 6.15 (a).

In case of Bernoulli as well as tent maps the BER shows a staircase structure for some couplings. As derived in Appendix B this devil's staircase is related to a fractal structure of the distribution $\rho(d)$.

Distribution $\rho(d)$

The distribution $\rho(d)$ is generally not know analytically and in the following it is investigated by means of computer simulations. The obtained distributions for the

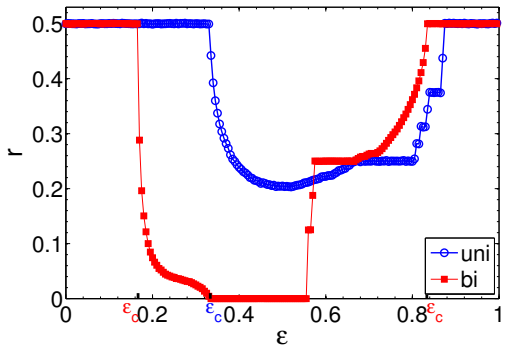

(a) Bernoulli maps, $a = 1.5$

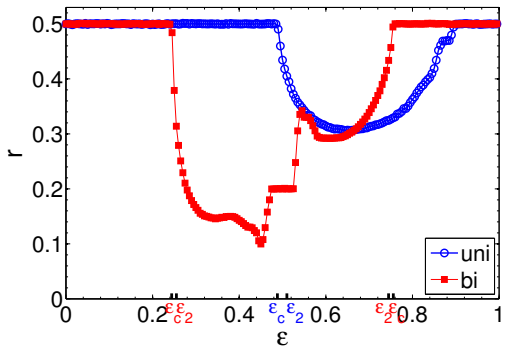

(b) Tent maps, $a = 0.4$

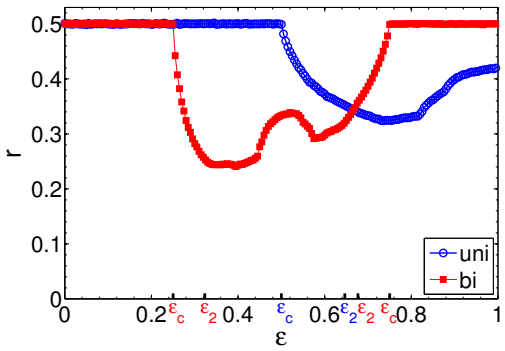

(c) Logistic maps, $a = 4$

FIGURE 6.15: Bit error rate r for uni- and bi-directionally coupled maps. Parameters are $\tau = 0$, $\kappa = 0$ and $M = 10^{-8}$. The synchronization transition is indicated by ϵ_c and the transition to a finite second moment by ϵ_2.

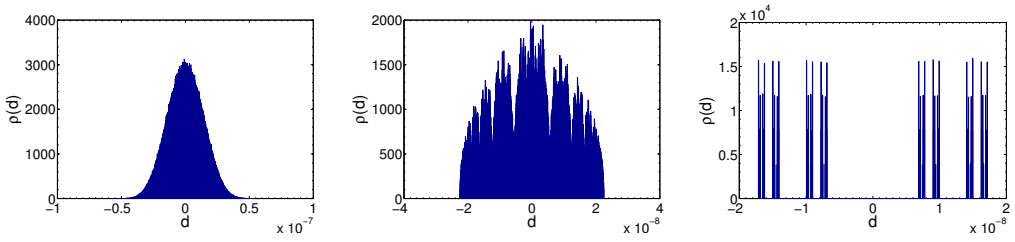

(a) $\epsilon = 0.4$ (b) $\epsilon = 0.6$ (c) $\epsilon = 0.8$

FIGURE 6.16: Probability distribution $\rho(d)$ for uni-directionally coupled Bernoulli maps for different couplings ϵ. Parameters are $a = 1.5$, $\tau = 0$, $\kappa = 0$ and $M = 10^{-8}$.

uni- and bi-directional setup have very similar properties. Therefor we restrict the presented graphs for Bernoulli, tent and logistic maps to either one of the setups in the following.

For Bernoulli maps, the simulations show that close to the synchronization transition $\rho(d)$ is rather broad with a Gaussian-like shape, see Figure 6.16(a). Changing the coupling ϵ such that the system move towards a more strongly synchronized regime, the distribution obtains a fractal structure, see Figure 6.16(b), until it eventually becomes heavily peaked, see Figure 6.16(c). As it is derived in Appendix B, for the uni-directional setup the peaked distribution occurs for $\epsilon > \frac{2}{3}$ whereas for the bi-directional setup the distribution is peaked for $\frac{1}{3} \leq \epsilon \leq \frac{2}{3}$. For a peaked distribution the BER locks into rational values $r = \frac{k}{2^q}$ with k and q being natural numbers. Note that the fractal properties of the distribution $\rho(d)$ are related to the theory of iterated function systems [103]. For Bernoulli maps, equation (6.9) and (6.20) give iterations of two linear functions due to $m_t = \pm 1$. Iterating a few randomly chosen functions can lead to fractal distribution, see Appendix B for more details.

In contrast to Bernoulli maps, the distribution for the tent map system can have very long tails, see Figure 6.17(a). As discussed in the previous section the distribution can follow a power law. We find these long tails in the parameter range where the system is synchronized but the second moment diverges. The time series d_t shows an intermittent behavior with occasional bursts. For Bernoulli maps there is no such parameter range since both transitions take place at the same point. Slightly increasing the coupling such that the moments become finite, the distribution shows a Gaussian-like shape and it drops to zero at a few multiples of the noise strength, see Figure 6.17(b). Apart from the heavy tails close to the synchronization transition, the distribution $\rho(d)$ for coupled tent maps has a similar behavior as the one for Bernoulli maps. It also shows a peaked structure which is related to a staircase in the BER, see Figure 6.17(c).

For logistic maps the distribution $\rho(d)$ also has power law tails, as long as there exists diverging moments, see Figure 6.18(a). Once all moments are finite the heavy tails vanish, see Figure 6.18(b). But unlike to Bernoulli and tent maps $\rho(d)$ does not show a strongly peaked structure. The distribution has always a connected support

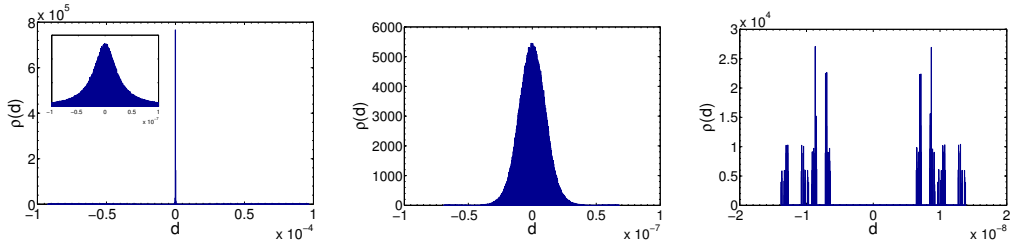

(a) $\epsilon = 0.25$ (b) $\epsilon = 0.3$ (c) $\epsilon = 0.47$

FIGURE 6.17: Probability distribution $\rho(d)$ bi-directionally coupled Tent maps for different couplings ϵ. Parameters are $a = 0.4$, $\tau = 0$, $\kappa = 0$ and $M = 10^{-8}$.

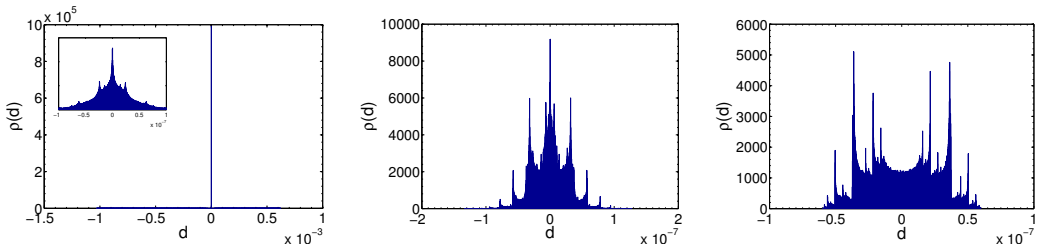

(a) $\epsilon = 0.6$ (b) $\epsilon = 0.8$ (c) $\epsilon = 0.9$

FIGURE 6.18: Probability distribution $\rho(d)$ uni-directionally coupled Logistic maps for different couplings ϵ. Parameters are $a = 4$, $\tau = 0$, $\kappa = 0$ and $M = 10^{-8}$.

due to the broad distribution of the multiplicative noise f', see Figure 6.18(b) and 6.18(c). Note that when zooming in around the peak of the heavy tailed distribution, we find its shape to be similar to the one of the distribution for finite moments.

6.3.2 Systems with Time Delay

The BER for systems with large time delays are obtained from numerical simulations. Results for uni- as well as the bi-directionally coupled Bernoulli, tent and logistic maps are shown in Figure 6.19. The synchronization transition is also indicated in the plots and illustrates that the BER, similar as for the undelayed system, is reduced as soon as the system synchronizes.

Note that our results show that the integral over the distribution of distances, equation (6.29), which determines the BER, is insensitive to long tails of $\rho(d)$. Although the responses χ_n diverge at different coupling strengths ϵ_n, the BER is smooth as a function of ϵ.

In our model the BER is rather high compared to reported values of analog and other digital systems. Hence our investigation just gives a qualitative explanation of chaos pass filter. But note, that we are using bits of length $L = 1$ for our investigation. The BER can be exponentially reduced by increasing L.

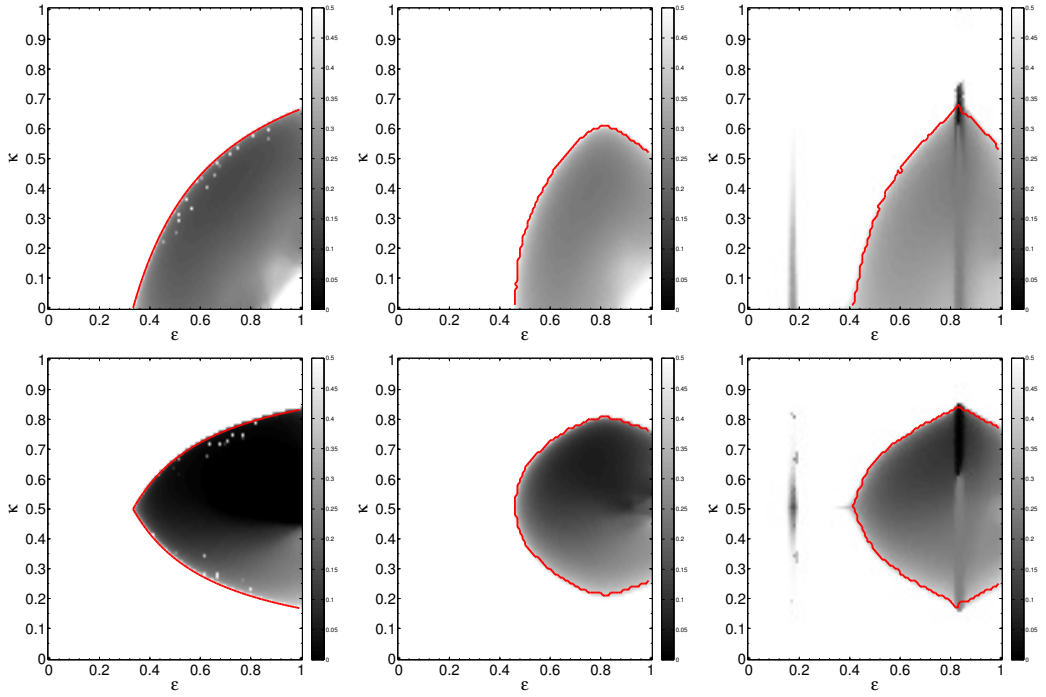

(a) Bernoulli map, $a = 1.5$ (b) Tent map, $a = 0.4$ (c) Logistic map, $a = 4$

FIGURE 6.19: Bit error rate r for two uni-directionally (upper row) and bi-directionally (lower row) coupled maps with delay $\tau = 100$ as a function of the couplings ϵ and κ. The solid red line indicates the synchronization transition, i.e., the boundary for which all cross correlations are larger than a threshold, $C \geq \theta_c = 0.999$. The maximum noise strength is $M = 10^{-8}$.

6.4 Resonances – Response to Harmonic Perturbations

In the previous sections we investigated the linear response of a synchronized chaotic system to an external perturbation by means of the BER and the moments of the distribution of the distance. The distance d is given by the linearized equations (6.2) and (6.5) for the uni and bi-directional setup, respectively.

For Bernoulli maps these linear equations have constant coefficients and hence any arbitrary perturbation can be decomposed into its Fourier modes. In this special case it is sufficient to investigate the linear response of the system to a harmonic perturbation of the form $m_t = M \exp(-i\omega_0 t)$. The system responds with the identical frequency $d_t = D \exp(-i\omega_0 t)$ and the amplitude of the recovered signal $\tilde{m} = m_t - d_t$ is given by

$$|\tilde{m}| = |M - D| \,. \tag{6.30}$$

The complex amplitude D can be derived analytically and we obtain the following results

- uni-directional case

$$D = M \frac{\epsilon(1-\kappa)a}{e^{-i\omega_0(\tau+1)} - (1-\epsilon)ae^{-i\omega_0\tau} - \epsilon\kappa a} \tag{6.31}$$

- bi-directional case

$$D = M \frac{\epsilon(1-\kappa)a}{e^{-i\omega_0(\tau+1)} - (1-\epsilon)ae^{-i\omega_0\tau} - \epsilon(2\kappa-1)a} \,. \tag{6.32}$$

Figure 6.20 shows $|\tilde{m}|$ as a function of ω_0 close to the phase boundary of synchronization. The amplitude of the reconstructed signal shows peaks (resonances) separated by a distance $2\pi/(\tau+1)$ which are caused by the first term of the denominator in equation (6.31). If the external perturbation matches these specific system's eigen frequencies, the response can be very large. The magnitude of the peaks is modulated due to the discrete nature of the system's equations. The resonances diverge at the synchronization boundary.

For the logistic and tent map the coefficients of the linear equations (6.2) and (6.5) depend on time. Thus an exact Fourier decomposition of the transmitted signal is not possible. But we can numerically investigate the response of these systems to a harmonic perturbation by means of the power spectrum $S(\omega)$ of the recovered message $\tilde{m}_t$. $S(\omega)$ exhibits a clear peak at the frequency ω_0 of the harmonic perturbation but, surprisingly, it shows no higher harmonics, see Figure 6.21. Hence, the system essentially responds with the excitatory frequency only.

These results show that a chaotic system can function as a sharp harmonic filter. The transmitted signal is irregular and the harmonic perturbation is arbitrarily small. Nevertheless, the receiver can filter out this perturbation with high precision. This is a surprising result which deserves further investigation. In particular, it would be

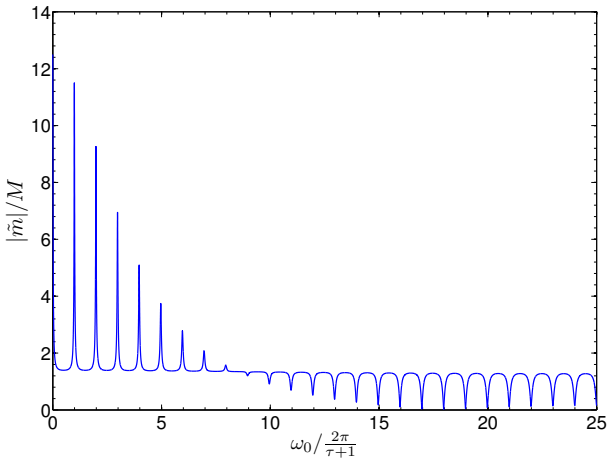

FIGURE 6.20: Amplitude of the reconstructed signal $\tilde{m}$ for different signal frequencies ω_0. Bernoulli map, uni-directional coupling with $a = 1.5$, $\epsilon = 0.8$, $\kappa = 0.55$ and $\tau = 50$.

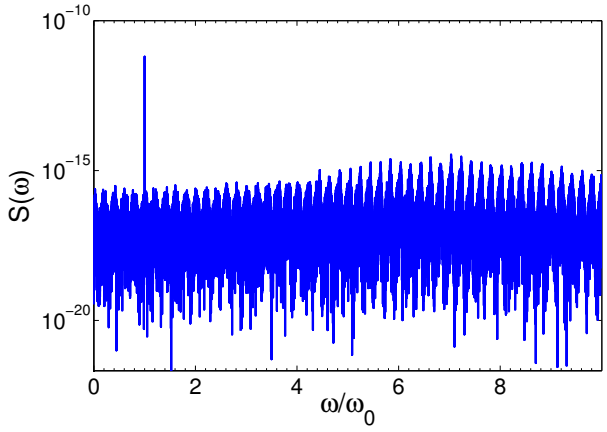

FIGURE 6.21: Power spectrum $S(\omega)$ of a reconstructed message $\tilde{m}$ in a semilogarithmic plot. Original message is of form $m_t = M \sin \omega_0 t$ with $M = 10^{-8}$ and $\omega_0 = 5 \cdot 2\pi/\tau$. Tent map, uni-directional coupling with $a = 0.4$, $\epsilon = 0.6$, $\kappa = 0.4$ and $\tau = 100$. Note that the underlying periodic structure is due to the sampling frequency.

interesting to examine this harmonic filter with respect to secret communication. The response of synchronized chaotic semiconductor lasers to a harmonic perturbation has been investigated in reference [104].

6.5 The Transversal Lyapunov Spectra

For stable chaos synchronization the distance d_t decays to zero such that the system's dynamics is restricted to the SM. An external perturbation, however, drives the system away from this manifold. The competition between these two mechanisms results in the linear response investigated in the previous sections.

The relaxation to the SM is described in terms of transversal LEs. For stable synchronization all transversal exponents are negative whereas in the unsynchronized case positive exponents exist. Close to the transition the maximum transversal exponent becomes very small until it eventually crosses zero at the transition. This results in a slowing down of the relaxation to synchronization and in a divergence of the response close to the transition. Diverging moments and power law tails are in particular related to local positive transversal LEs. Although the transversal exponents are negative in the synchronized case there can occur positive local ones which lead to temporary large excursions away from the SM. These positive transversal finite-time exponents may be caused by unstable periodic orbits or invariant subjects of the chaotic manifold [79, 105].

The Lyapunov spectrum, as well as the response functions χ_n and the BER r are average quantities describing the system. The maximum LE of the transversal spectrum, λ_{mt}, determines the synchronization properties of the system and one might expect that the qualitative behavior of χ_n and r is related to this exponent. However, it is not as simple as that. The response of the system is determined by the full Lyapunov spectrum in a non-trivial way and not only by the maximum transversal exponent.

For example, consider the driven system without delay nor feedback, equation (6.9), for which the transversal LE is given by equation (6.10), $\lambda_{mt} = \ln(1-\epsilon) + \langle \ln|f'| \rangle$. It decreases monotonically with increasing coupling strength ϵ, whereas the bit error rate r first decreases with ϵ to a minimum value before it increases again, see Figure 6.15.

For a Bernoulli system with delay τ the spectra of LEs can be calculated by solving polynomial equations of order τ, as it was explained in Section 3.4. We can group the LEs according to the eigenvalues of the adjacency matrix into a transversal and a longitudinal spectrum. For chaotic maps which do not have constant coefficients in the master stability function, such as the tent and logistic map, it is not possible to solve the polynomial equation but we have to rely on numerical simulations, see Section 3.5. Figure 6.22 shows the Lyapunov spectrum as a function of ϵ for a Bernoulli as well as a tent map system. The qualitative behavior of the maximum transversal LE and the BER is in both cases, apart from the synchronization transition, not obviously related. At the synchronization transition the maximum transversal LE

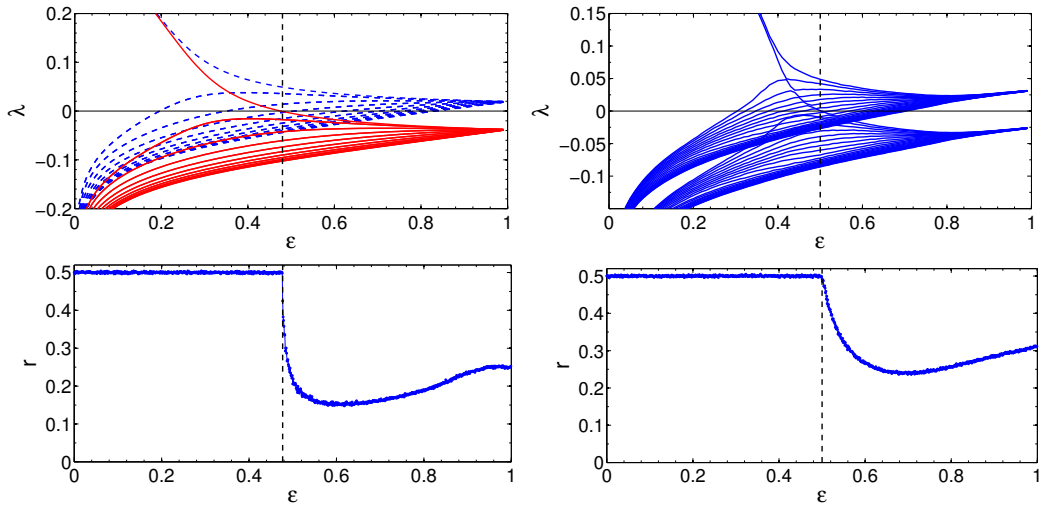

(a) Bernoulli map, $a = 1.5$

(b) Tent map, $a = 0.4$

FIGURE 6.22: Lyapunov spectrum and bit error rate for uni-directionally coupled maps with $\kappa = 0.3$, $\tau = 20$ and binary noise $M = 10^{-8}$. Note that the Lapunov exponent spectrum for the Bernoulli maps were obtained by solving polynomial equations, such that we can divide the spectrum in its transversal (red solid line) and longitudinal (dashed blue line) part. For tent maps we have to rely on numerical simulation where we cannot group the spectrum. Vertical dashed line indicates the synchronization transition.

becomes negative and the BER starts to decrease from its maximum of $r = 0.5$.

6.6 Small Networks

Having discussed the linear response of a coupled two units system at length in the previous sections, we investigate the linear response of more complicated setups such as a chain of three units and a network of four units in this section. As before the linear response is investigated by means of the second moment χ_2 of the distribution $\rho(d)$ and the BER r. The motivation stems again from chaos communication. Hence, in all setups the external perturbation is added to the signal of the sender and can be thought of as a secret message which shall securely be transmitted to the other units - the receivers.

The systems in this section are generally too complicated for an analytical discussion of the moments χ_n or the BER r. Hence we mainly rely on numerical simulations in the following.

We define the second moment for different units by χ_{ij} where the index stands for the combination of unit i and j, i.e., the distance $d_{ij} = x_t^j - x_t^i$ is used when evaluating equation (6.8). Similar, for the BER r_{ij} the signals of units i and j are compared. Due to the zero-lag synchronization the signals should be compared at

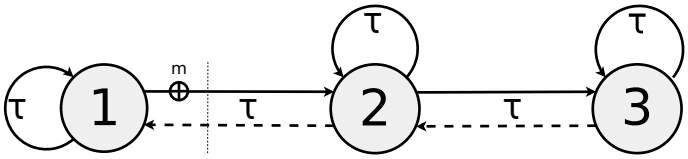

FIGURE 6.23: Setup of three coupled chaotic units with either uni- or bi-directional (dashed line) coupling. A perturbation m is added to the exchanged signal at unit 1, i.e., the sender. The transmitted signal has a time delay τ between adjacent units.

the same time t when evaluating χ_{ij} or r_{ij}, although the exchanged signals generally have different time delays for different receivers.

6.6.1 Chain of Three Units

We start by investigating a chain of three chaotic units. The units are arranged in a line such that the first unit is coupled to the second and the second to the third. The coupling can either be uni- or bi-directional and has a time delay. Optionally the units are subjected to a self-feedback with the same delay time. This setup is depicted in Figure 6.23.

Uni-directional Setup

For the uni-directional setup the system's equations read

$$\begin{aligned} x^1_{t+1} &= (1-\epsilon) f(x^1_t) + \epsilon f(x^1_{t-\tau}) \\ x^2_{t+1} &= (1-\epsilon) f(x^2_t) + \epsilon\kappa f(x^2_{t-\tau}) + \epsilon(1-\kappa)\, f(x^1_{t-\tau} + m_{t-\tau}) \\ x^3_{t+1} &= (1-\epsilon) f(x^3_t) + \epsilon\kappa f(x^3_{t-\tau}) + \epsilon(1-\kappa) f(x^2_{t-\tau})\,, \end{aligned} \tag{6.33}$$

where the parameters have the usual meaning.

For Bernoulli units without noise, $m_t = 0$, the synchronization properties can be analyzed analytically by a master stability function method, as explained in Section 3.4. In the limit of large delays we find that for this setup only complete synchronization between the three units can occur. Unit 1 imposes its chaotic behavior onto unit 2 which in turn imposes its behavior onto unit 3. The region of stable synchronization in the parameter space (ϵ, κ) is identical to the one of two uni-directionally coupled units. It is the region II + III in the phase diagram shown in Figure 6.2.

Simulations show that, similar to Bernoulli maps, for tent as well as for logistic maps only complete synchronization is possible. All three units synchronize with each other at the same coupling strength ϵ, although in the unsynchronized case the cross correlations are highest between unit 1 and 2. Numerical results for the cross correlation together with the second moment and the BER, respectively, are shown in Figure 6.24 for systems of Bernoulli, tent and logistic maps. χ_2 was obtained using uniformly distributed noise and r using binary noise. As we expect, the response,

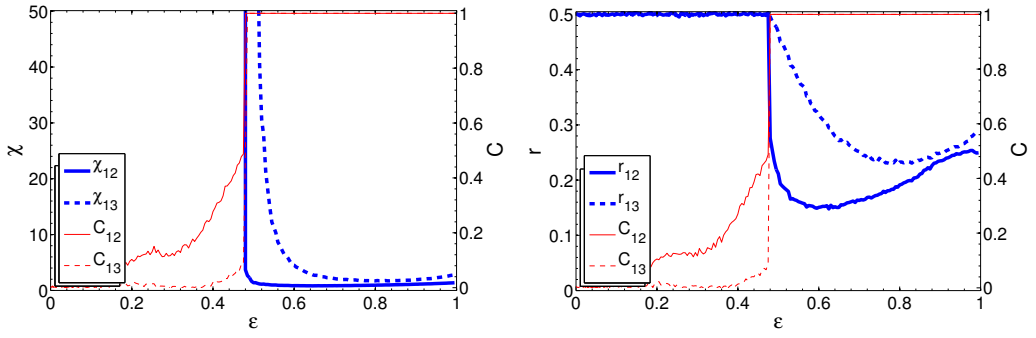

(a) Bernoulli maps, $a = 1.5$

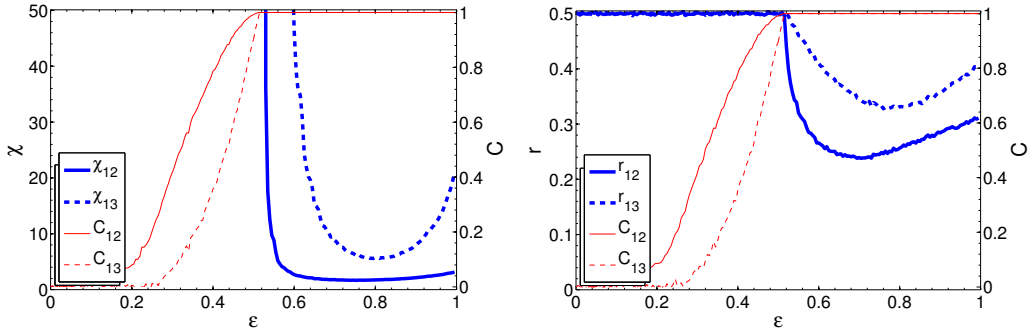

(b) Tent maps, $a = 0.4$

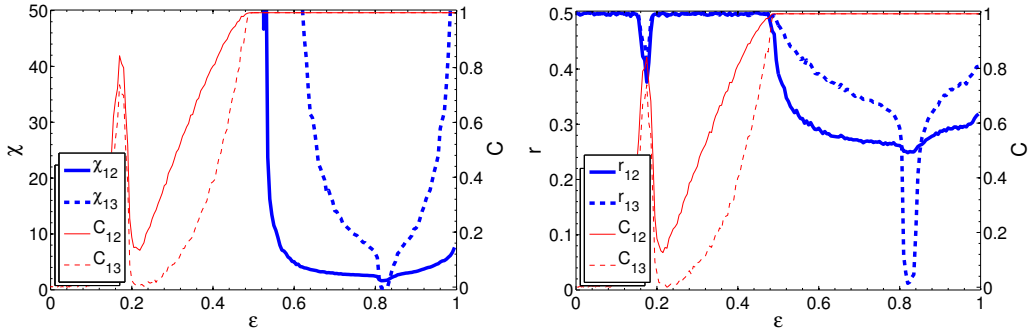

(c) Logistic maps, $a = 4$

FIGURE 6.24: Chain of three uni-directionally coupled chaotic maps with parameters $\kappa = 0.3$, $\tau = 100$ and $M = 10^{-8}$. Left hand side shows second moment χ_{ij} (thick blue curves) and cross correlation C_{ij} (thin red curves) for uniformly distributed random noise, right hand side shows bit error rate r_{ij} (thick blue curves) and cross correlation C_{ij} (thin red curves) for binary random noise as a function of ϵ. Solid (dashed) line shows the respective results for the combination of units $ij = 12$ (ij=13).

i.e., χ as well as r, is generally smallest for the combination of unit 1 and 2. Similar to the two units setup, the BER decreases for both combinations, r_{12} and r_{13}, at the synchronization transition. The second moments χ_{12} and χ_{13} diverge at different coupling strengths: in general χ_{12} diverges closer to the synchronization transition. For Bernoulli maps we find, in contrast to the two units setup, that the second moment χ_{13} diverges already inside the synchronized region. Note that the logistic maps system shows for small coupling ϵ strong correlation which are most likely due to some periodic windows, compare Figure 3.5 where these strong correlations can also be seen for the two units setup. In the synchronized region, we find a dip in χ_{13} as well as in r_{13} for logistic maps which we cannot explain and which deserves further investigation.

Bi-directional Setup

For the bi-directional setup the system's equations read

$$\begin{aligned} x^1_{t+1} &= (1-\epsilon) f(x^1_t) + \epsilon\kappa f(x^1_{t-\tau}) + \epsilon(1-\kappa) f(x^2_{t-\tau}) \\ x^2_{t+1} &= (1-\epsilon) f(x^2_t) + \epsilon\kappa f(x^2_{t-\tau}) + \epsilon(1-\kappa) \left(1/2\, f(x^1_{t-\tau} + m_{t-\tau}) + 1/2\, f(x^3_{t-\tau})\right) \\ x^3_{t+1} &= (1-\epsilon) f(x^3_t) + \epsilon\kappa f(x^3_{t-\tau}) + \epsilon(1-\kappa) f(x^2_{t-\tau})\,. \end{aligned} \tag{6.34}$$

As for the uni-directional setup, we can analyze the synchronization properties analytically for Bernoulli maps without noise. In the limit of large delays we find that complete and sub-lattice synchronization exists [67]. The region of complete synchronization is denoted by II in Figure 6.2, whereas in region III only unit 1 and 3 are synchronized.

The sub-lattice synchronization for a bi-directional setup is a generic phenomenon which also occurs in simulations of tent and logistic maps. We find unit 1 and 3 to synchronize perfectly and, hence, the distance d_{13} and also the second moment χ_{13} to be zero. A perturbation of the signal which unit 1 sends to unit 2 is completely filtered out and does not affect unit 3. This can easily be seen in the system's equations (6.34). Unit 1 and 3 obtain the same external input from unit 2 and since the units are identical they synchronize perfectly. Note that unit 2 does not necessarily need to be synchronized in order for perfect synchronization between unit 1 and 3 to occur. It acts as a relay which transmits the signals between the two units such that they can synchronize. Comparing the outgoing signal of unit 1, i.e. its internal dynamics plus the message m, with the outgoing signal of unit 3, the message can be recovered perfectly without any errors, thus the BER is $r_{13} = 0$.

Figure 6.25 shows the second moment and the BER together with the cross correlations for systems of Bernoulli, tent and logistic maps as a function of the coupling ϵ. The coupling constant κ was chosen such that sub-lattice synchronization occurs for some values of ϵ. Sub-lattice synchronization exists in the region where $C_{13} = 1$ but $C_{12}, C_{23} < 1$. At the transition to sub-lattice synchronization χ_{13} and r_{13} becomes zero. At the transition to complete synchronization the BER r_{12} decreases whereas the second moment χ_{12} still diverges close to the boundary (except for

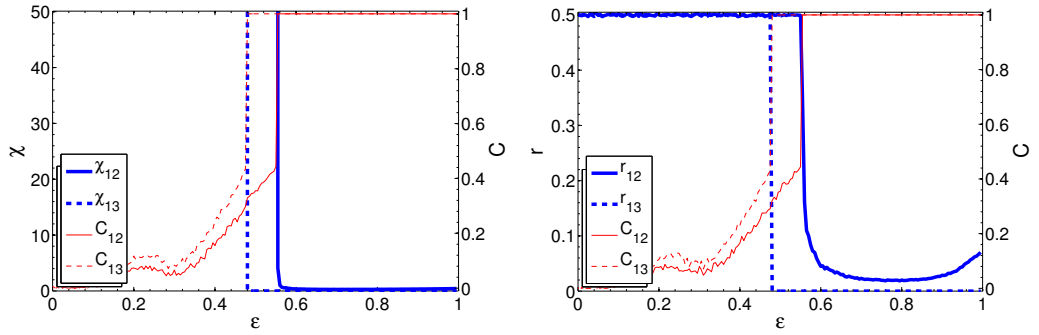

(a) Bernoulli maps, $a = 1.5$

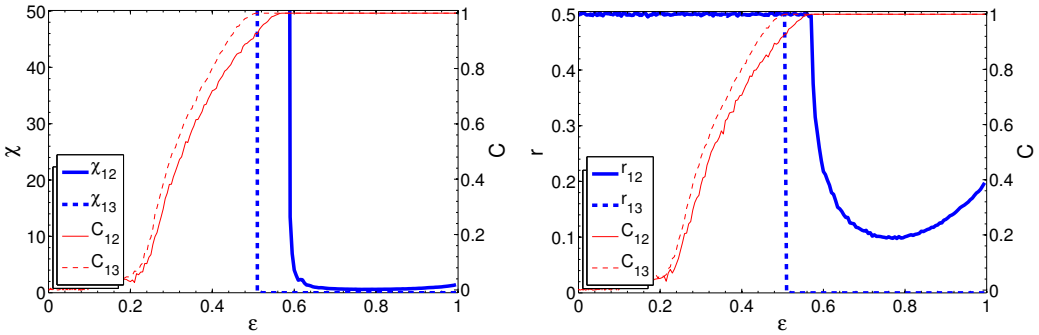

(b) Tent maps, $a = 0.4$

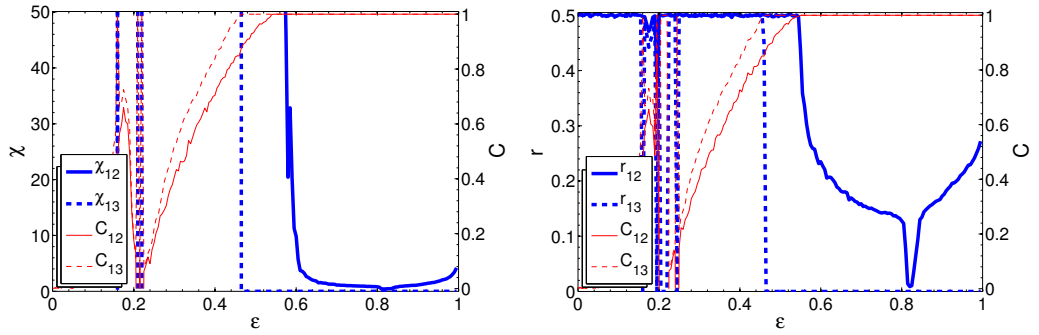

(c) Logistic maps, $a = 4$

FIGURE 6.25: Chain of three bi-directionally coupled chaotic maps with parameters $\kappa = 0.3$, $\tau = 100$ and $M = 10^{-8}$. Left hand side shows second moment χ_{ij} (thick blue curves) and cross correlation C_{ij} (thin red curves) for uniformly distributed random noise, right hand side shows bit error rate r_{ij} (thick blue curves) and cross correlation C_{ij} (thin red curves) for binary random noise as a function of ϵ. Solid (dashed) line shows the respective results for the combination of units $ij = 12$ (ij=13).

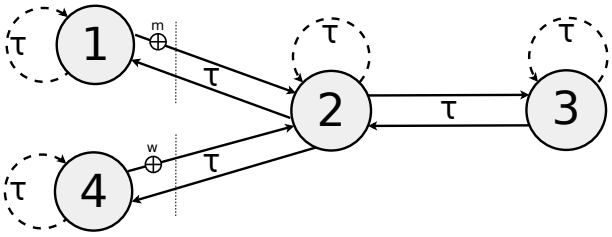

FIGURE 6.26: Setup of a star like configuration with unit 2 in the middle. Unit 2 obtains the unperturbed signal of unit 3, and the signal of unit 1 and 4 where a message m and w, respectively, is added. Unit 1, 3 and 4 can synchronize perfectly. Hence unit 2 can obtain m and w by subtracting the (unperturbed) signal of unit 3 from the signal of unit 1 and 4, respectively.

Bernoulli maps where χ_{12} diverges directly at the synchronization transition). But neither the BER r_{12} nor the second moment χ_{12} become zero. The external noise prevents the trajectories, $x_1 = x_3$ and x_2, of perfectly synchronizing. It causes the trajectories to deviate by a factor of the noise strength. Note that the logistic maps system shows strong correlations for small coupling ϵ and exhibits a dip in χ_{13} for a larger coupling ϵ, similar to the uni-directional setup.

In terms of chaos communication, unit 2 which obtains the signal of unit 1 and 3 can recover a message, which is added on top of the transmitted signal of unit 1, without any errors. In the same fashion more units can be added to the system in a star like setup with unit 2 being the relay. The additional units can also add a secret message on top of their transferred signals. Figure 6.26 shows the setup for a system with four units, but in principle an arbitrary number of units can be added. All units of the star, apart from unit 2, synchronize perfectly since they receive an identical driving signal. Unit 2 compares the signal from unit 3 with the incoming signals of units 1 and 4 and perfectly recovers both secret messages. Thus the hub of the star can simultaneously decode any number of secret messages.

Effect of Parameter Mismatch

In contrast to simulations, in experiments the units are never perfectly identical. In general there is some parameter mismatch present which could in principle destroy complete synchronization between unit 1 and 3 in the bi-directionally coupled chain discussed before, hence increasing the BER rate.

We investigated the effect of a parameter mismatch on the BER for this setup by detuning the parameter of all units by a factor of Δa. We find that the BER rate is very insensitive towards a parameter mismatch, as long as it is smaller than the amplitude of the transmitted message by approximately an order of magnitude, i.e., $\Delta a \leq 0.1M$. The deviations from perfect synchronization are of the order of the parameter mismatch and hence the message can be recovered almost perfectly if it is larger than the typical distance d from the SM. The BER as a function of $\Delta a/M$ is exemplarily shown for a tent map system in Figure 6.27. The BER is plotted for

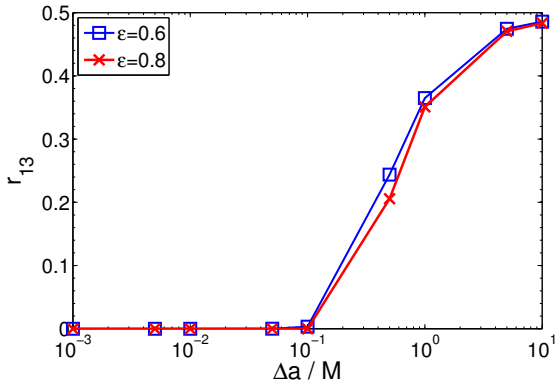

FIGURE 6.27: Bit error rate r_{13} vs. parameter mismatch of the units Δa for a chain of bi-directionally coupled tent maps shown for two different couplings ϵ. The parameters are $a = 0.4$, $\kappa = 0.3$, $\tau = 100$ and $M = 10^{-3}$.

two different couplings ϵ. Closer to the synchronizations transition, i.e. for $\epsilon = 0.6$, the BER is slightly more sensitive to a parameter mismatch.

6.6.2 Four Units Network

In the following we investigate a ring of four coupled units. For Bernoulli maps the synchronization properties for the unperturbed system can be calculated analytically. The stability of synchronization is determined by the eigenvalues of the adjacency matrix which describes the coupling of the units. For an adjacency matrix with row sum equals one, meaning that all incoming signals are normalized, and in the limit of large delays one finds that a spectral gap between the largest eigenvalue of $\gamma_1 = 1$ and the second largest eigenvalue γ_2 is crucial for the stability. Complete synchronization is only possible in the limit of weak chaos if the spectral gap is nonzero (compare Section 3.4). For a simple ring network without any self-feedback, where all eigenvalues are $\gamma = 1$, no eigenvalue gap exists and it cannot synchronize. Adding an additional link with the coupling strength σ changes the eigenvalues such that a gap occurs so that the system is able to synchronize [106].

The perturbed system, where a noise m is added onto all outgoing signals of unit 1, is depicted in Figure 6.28 and is described by following equations

$$\begin{aligned} x^1_{t+1} &= (1-\epsilon) f(x^1_t) + \epsilon f(x^4_{t-\tau}) \\ x^2_{t+1} &= (1-\epsilon) f(x^2_t) + \epsilon f(x^1_{t-\tau} + m_{t-\tau}) \\ x^3_{t+1} &= (1-\epsilon) f(x^3_t) + \epsilon \left(\sigma\, f(x^1_{t-\tau} + m_{t-\tau}) + (1-\sigma)\, f(x^2_{t-\tau})\right) \\ x^4_{t+1} &= (1-\epsilon) f(x^4_t) + \epsilon f(x^3_{t-\tau})\,. \end{aligned} \tag{6.35}$$

For such a network the eigenvalue gap in the unperturbed case, and therefor the synchronization ability, is maximal for $\sigma \approx 5/8 = 0.625$. But even for an optimal eigenvalue gap complete synchronization in this network is, without any additional

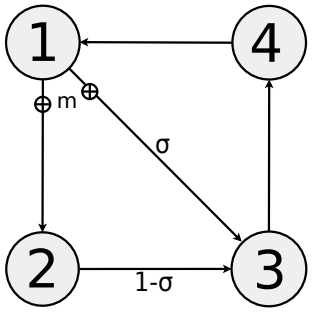

FIGURE 6.28: Ring network of four units plus an additional link of strength σ in order for the network to synchronize. A perturbation m is added to the outgoing signals of unit 1.

self-feedback, only possible if the chaoticity of the single units is very small, i.e. if each isolated unit has a small LE. For tent as well as logistic maps the network hardly synchronize completely and therefor we restrict the discussion to Bernoulli maps in the following.

For Bernoulli maps we find for the critical coupling at which synchronization occurs

$$\epsilon_c \geq \frac{1 - 1/a}{1 - |\gamma_2|}\,, \tag{6.36}$$

with a the parameter of the Bernoulli map, see equation (3.19). Thus for the maximum eigenvalue gap with $\sigma = 0.625$, the system synchronizes for $a \leq 1.16$. For Bernoulli maps with $a = 1.1$, the second moment χ_{1j} and the BER r_{1j} for combination of unit 1 with unit $j = 2, 3, 4$ are shown in Figure 6.29 together with the respective cross-correlations. Surprisingly the combination of unit 1 and 2 has the highest second moment and BER, whereas unit 4, which is only indirectly driven by unit 1, has the lowest second moment and BER.

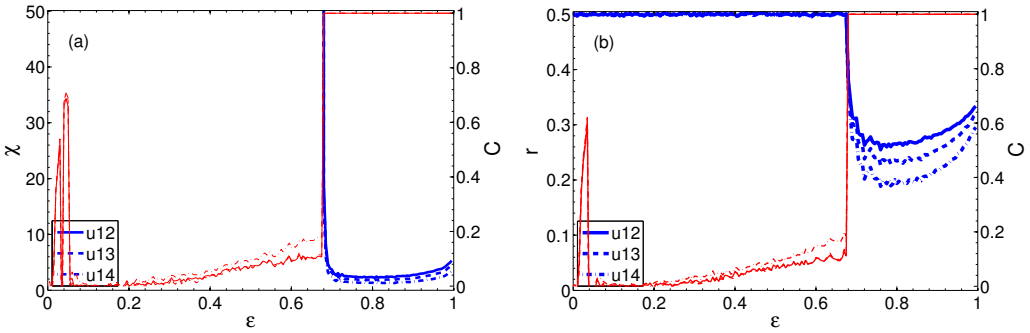

FIGURE 6.29: Panel (a) shows second moment χ_{1j} (thick blue curves) and cross correlation C_{1j} (thin red curves) for uniformly distributed random noise, panel (b) shows bit error rate r_{1j} (thick blue curves) and cross correlation C_{1j} (thin red curves) for binary random noise as a function of ϵ. Combination of units ij as indicated in the legend. Network of four coupled Bernoulli maps with parameters $a = 1.1$, $\tau = 100$, $\sigma = 0.625$ and $M = 10^{-8}$.

Chapter 7

Conclusion

7.1 Summary and Discussion

A system of time-delayed coupled chaotic units can synchronize to a collective chaotic behavior with zero time lag. In this thesis we studied the synchronization properties of networks of chaotic maps and looked into different aspects of chaos synchronization with the focus on time-delayed interaction. In particular, we investigated systems with multiple delays, where we could relate the scaling of the Lyapunov spectrum to the synchronization ability of hierarchical networks. Additionally, we studied the transition to chaos synchronization and the change in the attractor dimension at the transition. Finally, the effect of a perturbation onto the synchronization was analyzed, where we particularly investigated the linear response of synchronized systems to a small perturbation.

In Chapter 4 we studied systems with multiple delays on different time scales. These time scales appear in the Lyapunov spectrum and characterize its scaling. Depending on the scaling of the leading component of the spectrum with one of the delays, one can distinguish strong chaos or τ_k-chaos. We showed the different scaling behavior for a single unit with multiple delays. For a Bernoulli unit it was possible to derive analytical results whereas for a tent map system the scaling behavior was obtained numerically.
The results and insights obtained from studying a single unit system were finally applied to a network of networks, where time delays within a subnetwork are shorter than the time delays between the different subnetworks. We showed by means of numerical simulations of tent map systems, that in such a case, chaos synchronization is only possible if strong chaos is absent. Depending on the scaling of the maximum exponent either complete or subnetwork synchronization occurs. If the maximum Lyapunov exponent scales with the shorter delay, i.e., the delay of the intra-network connection, only the elements within a subnetwork can synchronize. If, however, the whole spectrum (including the maximum Lyapunov exponent) scales with the longer delay, i.e., the delay of the inter-network connection, complete synchronization of all elements of all subnetworks is possible.

The synchronization transition of networks with focus on the attractor dimension was studied in Chapter 5. We argued that for a synchronized system not all exponents of the total Lyapunov spectrum contribute to the Kaplan-Yorke dimension. This argument predicts a jump in the attractor dimension when the network synchronizes. In addition, the Kolmogorov prediction entropy should show a discontinuous slope. We tested these general predictions for a setup of two coupled iterated maps and compared the Kaplan-Yorke dimension to the correlation dimension. For Bernoulli maps, our numerical results show a clear discontinuous behavior of the attractor dimension. The Kaplan-Yorke as well as the correlation dimension jump to a low value at the synchronization transition. For tent maps, the numerical results of the correlation dimension are not so clear due to large statistical fluctuations caused by limited computational power. Nevertheless, our results indicate a jump in the attractor dimension, too. In both cases the Kolmogorov entropy shows a discontinuous slope.
For networks of Bernoulli maps we numerically calculated the Kaplan-Yorke dimension as a function of system size N and delay time τ in the region of strong chaos. We found that the dimension scales with $N\tau$ and the jump of the dimension at the synchronization transition scales with N.
Our argument of omitting bands of negative transversal Lyapunov exponents for the calculation of the Kaplan-Yorke dimension relies on the fact that the dynamics is restricted to the synchronization manifold. A tiny detuning of the nonlinear units leads to imperfect synchronization and our argument is no longer valid. We studied the effect of parameter mismatch and found that the correlation dimension continuously increases, towards the Kaplan-Yorke dimension which we would expect when taking all Lyapunov exponents into account, for an increasing mismatch.

In Chapter 6 we investigated the linear response of a time-delayed chaotic system to small external perturbations. This investigation is motivated by chaos communication, where a secret message is added on top of an exchanged signal between synchronized chaotic units, thus perturbing the system. This mechanism has been named chaos pass filter since the receiver is able to filter out any external perturbation. Thus, the receiver can recover the secret message by subtracting its own chaotic trajectory from the incoming signal.
We studied the linear response of iterated maps analytically as well as numerically and found that the mechanism of chaos pass filter is very complex. Perturbations are not just damped, instead the response of the receiver to the perturbation of the sender can be very large. Close to the synchronization transition it diverges. Even deep inside the region of synchronization huge excursions away from the synchronization manifold occur. The external perturbation causes attractor bubbling and gives rise to an intermittent bursting. This results in a power law behavior and diverging moments of the distribution of deviations between the sending and receiving unit. Mathematically, this is a consequence of multiplicative and additive noise appearing in the equations of linear response.
The bit error rate of a transmitted binary message is used as an additional quantity to investigate the linear response. It is given by an integral over the distribution of

deviations between the trajectories of sender and receiver. For the unsynchronized system the bit error rate is at its maximum of 50%. Directly at the synchronization transition the bit error rate decreases and inside the region of synchronization it shows a complex nonmonotonic behavior which cannot be related to the properties of the maximum transversal Lyapunov exponent. The bit error rate was computed numerically for Bernoulli, tent and logistic map systems. For Bernoulli as well as tent maps the bit error rate shows a devil's staircase as a function of model parameters related to a fractal distribution of deviations.
The linear response to a periodic perturbation was also investigated. It shows resonances due to the delayed feedback of the sending unit. Depending on parameters and frequency, those resonances can be very large but the response can also be suppressed.
Finally, we studied the linear response of a chain of three units and of a network of four units. We found that for a bi-directionally coupled chain of three units the perturbation is completely filtered out by the unit in the middle and both outer units can synchronize perfectly. Thus the second moment and the bit error rate becomes zero. Applying these results to a star network we showed that the central element can receive simultaneously any number of secret messages without any error.

In this thesis we restricted our investigations to chaotic maps which in some respects have different properties than chaotic flows. But for the relevant aspects studied here, namely strong/weak chaotic behavior and complete as well as sublattice synchronization, maps and flows are very similar. Many of the presented results can also be observed in numerical simulations of chaotic differential equations. Hence we believe that our findings will contribute to a general understanding of chaos synchronization.

7.2 Future Directions

We only studied symmetric networks throughout this thesis, i.e., networks with a constant row sum in the adjacency matrix, in particular symmetric networks of networks. The symmetry is a necessary condition in order to have identical synchronization. But in a lot of cases the networks are of an asymmetric kind. It would be interesting to analyze which conclusions are still valid for these more general networks.

When studying systems with multiple delays, we restricted the investigations to delays of different order of magnitude. Another aspect would be to investigate the scaling behavior of the Lyapunov spectrum for systems with different delays of the same order of magnitude. Is it possible to find similar, general results for such systems?

The results for the discontinuity in the attractor dimension for the tent map system are not clear without ambiguity. The correlation dimension is determined from the correlation function $C(\xi)$. This function shows large statistical fluctuations for small distances ξ and an extrapolation of the slope to small values of ξ is difficult. One would need to analyze longer time series in order to have a better statistic and to

obtain a clear result whether the correlation dimension of a tent map system behaves continuously or discontinuously at the synchronization transition. Unfortunately, a longer time series increases the computational time and the needed memory capacity for its analysis enormously and was not doable with the computational power available. Besides a more thorough analysis of the tent map system, it would also be interesting to investigate other systems, for example the logistic map or chaotic flows. So far, only the Bernoulli map shows a clear discontinuity in the correlation dimension. This system is of a very special kind since the coefficients in the linearized equations are constant, whereas for the other systems they fluctuate.

While studying the linear response of synchronized systems we found that the response can be very large close to the synchronization transition. The distribution of deviations has a power law tail and its moments diverge. In reference [107] coupled chaotic oscillators that display extreme events were investigated. The authors found sharp peaks in the tails of the distribution which deviate from an exact power law behavior. They argue that "attractor bubbling in riddled basins of attraction is a generic mechanism" for these peaks which they coined dragon kings, and conjectured that this mechanism applies "to a large class of spatially extended deterministic and stochastic nonlinear systems". Attractor bubbling also occurs in the systems we investigated. It would be interesting to study the tail of the distribution of distances, as shown in Figure 6.5, more thoroughly to check whether such peaks occur in this system as well.

The linear response to a periodic perturbation shows a clear resonance at the frequency of the harmonic perturbation but, surprisingly, it shows no higher harmonics. The chaotic system acts as a sharp harmonic filter that can filter out the perturbation with high precision. This effect is still not understood and deserves further investigation.

For the linear response of a chain of three units and of a network of four units we only presented numerical results in this thesis. We also tried to derive an analytical formula for the second moment for these systems, in a similar way to the two units setup. Unfortunately we did not succeed in doing so, mainly because we end up with cross terms such as $\langle d_{12}d_{23}\rangle$. Assuming that in the synchronized state it is $d_{12} = -d_{23}$ yields incorrect results. Another way to evaluate expressions such as $\langle d_{12}d_{23}\rangle$ could be using a Laplace transformation. Due to time restraints we were not able to check this idea.

In general, it would be interesting to investigate the linear response of synchronized chaotic networks further. Of importance is particularly the problem how a (harmonic) signal travels through a network, and, related to it, the question whether the network structure can be deduced from the network's response.

Appendix A

Random Numbers with an Arbitrary Distribution

In Section 6.2 we could approximately relate the undelayed linearized system's equations (6.9) and (6.20) to stochastic equations with multiplicative and additive noise by assuming the variable f' in the linearized system's equations to be uncorrelated random numbers with a specific probability distribution. In Section 6.2.3 we checked the approximation for logistic maps, for which we know the distribution $\rho(f')$ of a single unit. We simulated the linearized equations (6.9) and (6.20) but substituted f' by random numbers distributed according to the desired $\rho(f')$.

There exists libraries for random numbers distributed according to commonly used distributions such as the uniform distribution. However, for random numbers with an desired arbitrary distribution there generally do not exist any libraries but we have to create it from existing distributions.

To create random numbers with a desired arbitrary distribution $\rho(x)$ from uniformly distributed random numbers $u \in [0, 1]$ we can use the so-called *transformation method*.

The distributions are related according to

$$|\rho(x)\,\mathrm{d}x| = |\delta(u)\,\mathrm{d}u|\,, \tag{A.1}$$

where $\delta(u)$ is the uniform distribution with

$$\delta(u)\,\mathrm{d}u = \begin{cases} \text{const} & 0 \leq 1 \\ 0 & \textit{otherwise} \end{cases} \tag{A.2}$$

Integrating equation (A.1) gives

$$\int_{-\infty}^{x} \rho(x)\,\mathrm{d}x = \int_{-\infty}^{u(x)} \delta(u)\,\mathrm{d}u\,, \tag{A.3}$$

which is

$$u(x) = \int_{-\infty}^{x} \rho(x)\,\mathrm{d}x = P(x)\,. \tag{A.4}$$

Now we are only left with finding the inverse of $u(x)$. The inverse $x(u)$ yields the desired transformation to obtain random numbers x with a distribution $\rho(x)$ from the uniformly distributed random number u.

Example Random numbers with a logistic distribution

The distribution of f' for the logistic map $f(x) = 4x(1-x)$ is given as

$$\rho(f') = \begin{cases} \frac{1}{\pi\sqrt{16-f'^2}} & -4 \leq f' \leq 4 \\ 0 & otherwise \end{cases} \tag{A.5}$$

Thus

$$u(x) = \int_{-4}^{x} \frac{1}{\pi\sqrt{16-f'^2}}\,\mathrm{d}f' = \frac{1}{\pi}\left[\arcsin\frac{f'}{4}\right]_{-4}^{x} = \frac{1}{\pi}\arcsin\frac{x}{4} + \frac{1}{2}\,. \tag{A.6}$$

The inverse is

$$x(u) = 4\sin\left(\pi\left(u - \frac{1}{2}\right)\right)\,. \tag{A.7}$$

This is the desired transformation in order to obtain random numbers x, from uniformly distributed random numbers u, distributed according to equation A.5.

Appendix B

Analytic Results For The Bit Error Rate

In Section 6.3 the BER was introduced as a way to quantify the quality of the reconstruction of a binary message and as an indirect measure of the linear response of a synchronized system to an external perturbation.

In general we cannot compute the BER analytically but have to rely on numerical simulations. Only for some special cases it can be calculated analytically. These analytic calculations are shown in the following. They were performed by Johannes Kestler and have been published in [80].

B.1 Logistic map, uni-directional setup, $\tau = 0$, $\epsilon = 1$, $\kappa = 0$

In the case of the uni-directional setup with logistic maps and no time delay the BER can be calculated for the point $\epsilon = 1$. The dynamics is given by

$$x_{t+1} = f(x_t) \tag{B.1}$$

$$y_{t+1} = f(x_{t-1} + m_{t-1})\,, \tag{B.2}$$

from which follows that

$$d_{t+1} = f'_t m_t\,. \tag{B.3}$$

From the facts that (1) f'_t and m_t are uncorrelated, (2) the probability distribution of f' is symmetric about $f' = 0$ and (3) $m_t = \pm M$, follows that d has basically the same probability distribution as f'. Therefore, the BER can easily be calculated, see equation (6.29) and (6.14):

$$r = \frac{1}{2}\left(1 - \int_{-M}^{M} p(d)\,\mathrm{d}d\right) = \frac{1}{2}\left(1 - \int_{-1}^{1} \rho(f')\mathrm{d}f'\right) = \frac{\operatorname{arcsec}(4)}{\pi} \approx 0.4196\,. \tag{B.4}$$

This is in agreement with the numerical simulations.

B.2 Logistic map, bi-directional setup, $\tau = 0$, $\epsilon = \frac{1}{2}$, $\kappa = 0$

Similarly, in the bi-directional case the BER can be calculated for $\epsilon = \frac{1}{2}$. The dynamics is given by

$$x_{t+1} = \frac{1}{2} f(x_t) + \frac{1}{2} f(y_t) \tag{B.5}$$

$$y_{t+1} = \frac{1}{2} f(y_t) + \frac{1}{2} f(x_t + m_t)\,, \tag{B.6}$$

from which follows that

$$d_{t+1} = \frac{1}{2} f_t' m_t\,. \tag{B.7}$$

Comparing this with equation (B.3) leads to

$$r = \frac{1}{2}\left(1 - \int_{-2}^{2} \rho(f')\mathrm{d}f'\right) = \frac{1}{3}\,, \tag{B.8}$$

which is also in agreement with the numerical simulations.

B.3 Bernoulli map, $\tau = 0$

In Figure 6.15(a) one can discover a staircase structure for the BER. For the uni-directional setup this is true for $\epsilon \geq \frac{2}{3}$, while for the bi-directional setup this is valid for $\frac{1}{3} \leq \epsilon \leq \frac{2}{3}$. For these regions the BER can be calculated analytically. If one takes a closer look at the staircases, Figure B.1, it becomes apparent that they have infinitely many steps, i.e., they are a kind of devil's staircase.

B.3.1 Uni-directional coupling

This staircase structure should be explained here for the case of uni-directional coupling. The equation for the distance can be written in the following way, see also equation 6.9:

$$d_t = \begin{cases} d_t^- = \frac{3}{2}(1-\epsilon)d_{t-1} - \frac{3}{2}\epsilon M \\ d_t^+ = \frac{3}{2}(1-\epsilon)d_{t-1} + \frac{3}{2}\epsilon M \end{cases} \tag{B.9}$$

The two equations represent the two different bits. If d_t is plotted versus d_{t-1}, then d_t^- and d_t^+ are two parallel straight lines, see Figure B.2. The values of this iteration $d_t(d_{t-1})$ generate the distribution $p(d)$ from which, in principle, the BER

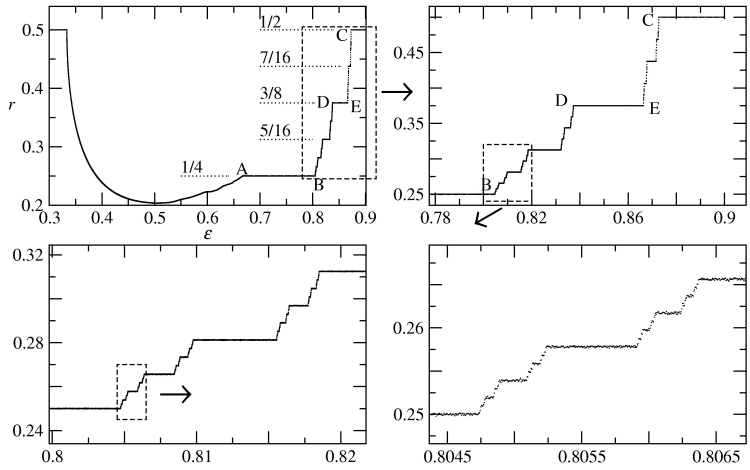

FIGURE B.1: Bit error rate r for uni-directionally coupled Bernoulli maps with $\tau = 0$ and $\kappa = 0$. Zooming in the staircase structure reveals more and more steps.

can be calculated. The dashed boxes (– –) in Figure B.2 represent the interval which d_t is bounded to (due to the attracting fixed points). For $\epsilon < \frac{2}{3}$ the two maps d_t^- and d_t^+ have a certain overlap in their co-domain, see Figure B.2(a) (the co-domains are indicated by gray stripes). This fact makes the distribution $p(d)$ complicated. However, for $\epsilon > \frac{2}{3}$ the two maps have no overlap, see Figure B.2(c), and the distribution is manageable analytically. As a result of the gap in the co-domain (indicated by a zigzag pattern), a gap in the domain emerges in the next time step. The latter gap produces two further gaps in the co-domain which become gaps in the domain in the next time step. The result of this iterative process is that the distribution $p(d)$ has a fractal support. The first and largest gaps are shown in Figure B.3. The first gap is called G. The gaps produced by G are G^- and G^+. The gaps coming from G^+ are called G^{-+} and G^{++}; the gaps coming from G^- are called G^{--} and G^{+-} and so on.

Now we want to calculate the exact position of the gaps. The fixed points of d^- and d^+ are called d_*^- and d_*^+. One can easily calculate that

$$d_*^- = -\frac{3\epsilon M}{3\epsilon - 1} \qquad \text{and} \qquad d_*^+ = +\frac{3\epsilon M}{3\epsilon - 1}\,. \tag{B.10}$$

From Figure B.2(c) it can be seen that

$$G = \left]\, d^-(d_*^+), d^+(d_*^-) \,\right[= \left]\, -\frac{3\epsilon(3\epsilon-2)M}{3\epsilon-1}, \frac{3\epsilon(3\epsilon-2)M}{3\epsilon-1} \,\right[\,, \tag{B.11}$$

which is about $]-0.19M, 0.19M[$ for $\epsilon = 0.7$, see Figure B.3.

The gap G^+ is generated by applying d^+ to G, i.e.

$$\begin{aligned} G^+ &= \left]\, d^+(d^-(d_*^+)), d^+(d^+(d_*^-)) \,\right[\\ &= \left]\, \frac{3\epsilon(5-12\epsilon+9\epsilon^2)M}{2(3\epsilon-1)}, -\frac{3\epsilon(5-12\epsilon+9\epsilon^2)M}{2(3\epsilon-1)} \,\right[\,, \end{aligned} \tag{B.12}$$

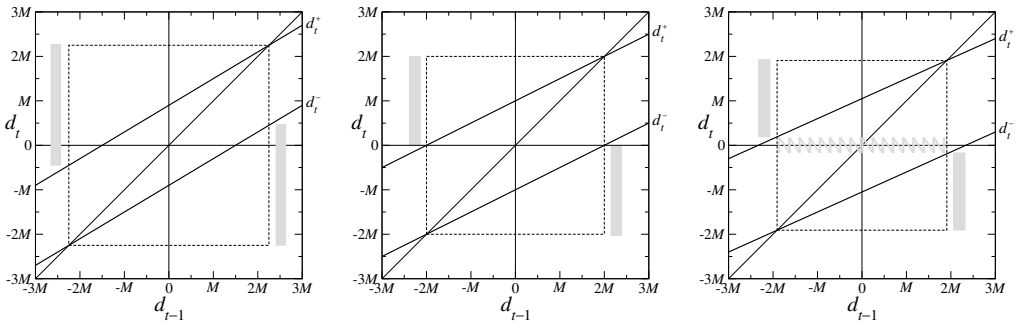

(a) $\epsilon = 0.6$; d^- and d^+ have an overlap in their co-domains.

(b) $\epsilon = \frac{2}{3}$

(c) $\epsilon = 0.7$; d^- and d^+ have no overlap in their co-domains.

FIGURE B.2: The iteration $d_t(d_{t-1}) = d_t^{\pm}(d_{t-1})$ of the distances for different coupling parameters ϵ. The dashed boxes represent the interval which d is bounded to due to the fixed points. Additionally, the bisecting line $d_t(d_{t-1}) = d_{t-1}$ is plotted. The gray stripes show the co-domains of d^- and d^+.

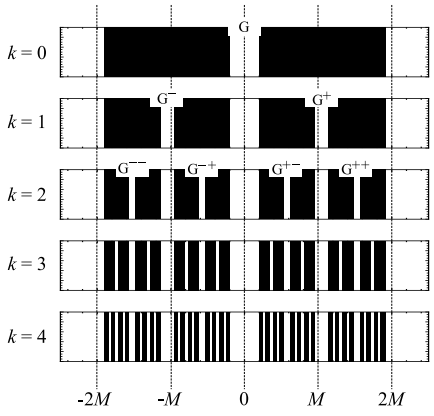

FIGURE B.3: Gaps in the domain/co-domain/distribution of d^- and d^+ for different recursion depths k. $\epsilon = 0.7$.

which is about $]0.96M, 1.14M[$ for $\epsilon = 0.7$, see Figure B.3.

Then the gap G^{-+}, for example, is generated by applying d^- to G^+, i.e.

$$G^{-+} = \left]d^-(d^+(d^-(d_*^+))), d^-(d^+(d^+(d_*^-)))\right[\,, \tag{B.13}$$

and so on.

Due to the constant and equal slope of d^- and d^+, and due to the fact that there is no overlap between the co-domains of d^- and d^+, the relative frequency of all distances d which occur (i.e. which are not inside a gap) are equal. This means that Figure B.3 can also be seen as the corresponding histogram; all bars have the same height.

The BER is related to the integral from $-M$ to $+M$ over the distribution of the distances, see equation (6.29). FromFigure B.3 it can be seen that for $\epsilon = 0.7$ this integral exactly equals $\frac{1}{2}$; thus, the BER equals $\frac{1}{4}$, which is in agreement with Figure B.1.

If ϵ is changed, then the positions of the gaps are changed, too. As long as the gap G^+ contains the value $+M$ (= as long as the gap G^- contains the value $-M$), the integral yields $\frac{1}{2}$ and the BER is $\frac{1}{4}$. This explains the plateau AB in Figure B.1. With the aid of equation B.12 we can calculate the exact position of this plateau:

$$\text{A: } \epsilon = \frac{2}{3} = 0.\overline{6} \qquad \text{and} \qquad \text{B: } \epsilon = \frac{1}{3}(1+\sqrt{2}) \approx 0.804738\,. \tag{B.14}$$

Similarly, one gets the point C of Figure B.1. The BER becomes $\frac{1}{2}$ when the integral starts to be 0. This is when the gap G is as large as (or larger than) the interval $[-M, M]$. Considering equation B.11 yields:

$$\text{C: } \epsilon = \frac{1}{6}(3+\sqrt{5}) \approx 0.872678\,. \tag{B.15}$$

The plateau DE, which has the value $\frac{3}{8}$, can be calculated considering the gap G^{+-}. One gets:

$$\text{D: } \epsilon \approx 0.837266 \qquad \text{and} \qquad \text{E: } \epsilon \approx 0.866386\,, \tag{B.16}$$

All other plateaus can be calculated with the aid of smaller gaps.

B.3.2 Bi-directional coupling

The calculations for the case of bi-directional coupling are very similar to the ones for the uni-directional case. Here, only few results should be shown.

For

$$0.\overline{3} = \frac{1}{3} \leq \epsilon \leq \frac{5}{9} = 0.\overline{5}\,, \tag{B.17}$$

the BER is 0.

For

$$0.5749 \approx \frac{1}{6} + \frac{1}{\sqrt{6}} \leq\leq \frac{2}{3} = 0.\overline{6}\,, \tag{B.18}$$

the BER is $\frac{1}{4}$.

Bibliography

[1] Arkady Pikovsky, Michael Rosenblum, and Jürgen Kurths. *Synchronization: A Universal Concept in Nonlinear Sciences.* Cambridge University Press, 2001.

[2] Steven H. Strogatz. Exploring complex networks. *Nature*, 410:268–276, 2001.

[3] Réka Albert and Albert-László Barabási. Statistical mechanics of complex networks. *Rev. Mod. Phys.*, 74:47–97, 2002.

[4] M. Newman. The structure and function of complex networks. *SIAM Review*, 45:167–256, 2003.

[5] Duncan J. Watts. The "new" science of networks. *Annual Review of Sociology*, 30:243–270, 2004.

[6] S. Boccaletti, V. Latora, Y. Moreno, M. Chavez, and D.-U. Hwang. Complex networks: Structure and dynamics. *Physics Reports*, 424:175 – 308, 2006.

[7] Alex Arenas, Albert Díaz-Guilera, Jurgen Kurths, Yamir Moreno, and Changsong Zhou. Synchronization in complex networks. *Physics Reports*, 469:93 – 153, 2008.

[8] Heinz Georg Schuster and Wolfram Just. *Deterministic Chaos: An Introduction.* John Wiley & Sons, 4 edition, 2005.

[9] S. Boccaletti, J. Kurths, G. Osipov, D. L. Valladares, and C. S. Zhou. The synchronization of chaotic systems. *Physics Reports*, 366:1–2, 2002.

[10] E. N. Lorenz. Deterministic Nonperiodic Flow. *Journal of Atmospheric Sciences*, 20:130–148, 1963.

[11] June Barrow-Green. *Poincare and the Discovery of Chaos.* Icon Books, 2005.

[12] L. M. Pecora and T. L. Carroll. Synchronization in chaotic systems. *Phys. Rev. Lett.*, 64:821–824, 1990.

[13] K. Aihara, T. Takabe, and M. Toyoda. Chaotic neural networks. *Physics Letters A*, 144(6–7):333 – 340, 1990.

[14] Junji Ohtsubo. *Semiconductor Lasers: Stability, Instability and Chaos.* Springer, 2 edition, 2007.

[15] Leon O. Chua and Maciej J. Ogorzalek. *Chaos and Complexity in Nonlinear Electronic Circuits.* World Scientific Pub Co, 1997.

[16] G. Orosz, R. E. Wilson, R. Szalai, and G. Stépan. Exciting traffic jams: Nonlinear phenomena behind traffic jam formation on highways. *Phys. Rev. E*, 80(4):046205, 2009.

[17] L. Chen and K. Aihara. Stability of genetic regulatory networks with time delay. *IEEE Trans. Circuits Syst. I*, 49:602, 2002.

[18] W. Kinzel and I. Kanter. Secure communication with chaos synchronization. In E. Schöll and H.G. Schuster, editors, *Handbook of Chaos Control.* Wiley-VCH, Weinheim, second edition, 2008.

[19] S. Sivaprakasam, J. Paul, P. S. Spencer, P. Rees, and K. A. Shore. Nullified time-of-flight lead-lag in synchronization of chaotic external-cavity laser diodes. *Opt. Lett.*, 28:1397–1399, 2003.

[20] I. Fischer, R. Vicente, J. M. Buldu, M. Peil, C. R. Mirasso, M. C. Torrent, and J. García-Ojalvo. Zero-lag long-range synchronization via dynamical relaying. *Phys. Rev. Lett.*, 97:123902, 2006.

[21] M. W. Lee, J. Paul, C. Masoller, and K. A. Shore. Observation of cascade complete-chaos synchronization with zero time lag in laser diodes. *J. Opt. Soc. Am. B*, 23:846–851, 2006.

[22] T.E. Murphy, A.B. Cohen, B. Ravoori, K.R.B. Schmitt, A.V. Setty, F. Sorrentino, C.R.S. Williams, E. Ott, and Roy R. Complex dynamics and synchronization of delayed-feedback nonlinear oscillators. *Phil. Trans. R. Soc. A*, 368:343366, 2010.

[23] Bhargava Ravoori, Adam B. Cohen, Jie Sun, Adilson E. Motter, Thomas E. Murphy, and Rajarshi Roy. Robustness of optimal synchronization in real networks. *Phys. Rev. Lett.*, 107:034102, Jul 2011.

[24] L. Kocarev and S. Lian. *Chaos-based Cryptography: Theory, Algorithms and Applications.* Springer, 2011.

[25] U. Parlitz, L.O. Chua, Lj. Kocarev, K.S. Halle, and A. Shang. Transmission of digitial signals by chaotic syncrhonization. *International Journal of Bifurcation and Chaos*, 02:973–977, 1992.

[26] K. M. Cuomo and A. V. Oppenheim. Circuit implementation of synchronized chaos with applications to communications. *Phys. Rev. Lett.*, 71:65–68, 1993.

[27] K.M. Cuomo, A.V. Oppenheim, and S.H. Strogatz. Synchronization of lorenz-based chaotic circuits with applications to communications. *IEEE Transactions on Circuits and Systems II*, 40:626–633, 1993.

[28] G. D. VanWiggeren and R. Roy. Communication with chaotic lasers. *Science*, 279:1198–1200, 1998.

[29] Atsuchi Uchida. *Optical Communication with Chaotic Lasers.* Wiley-VCH, 2012.

[30] A. Argyris, D. Syvridis, L. Larger, V. Annovazzi-Lodi, P. Colet, I. Fischer, J. García-Ojalvo, C. R. Mirasso, L. Pesquera, and K. A. Shore. Chaos-based communications at high bit rates using commercial fibre-optic links. *Nature*, 438:343–346, 2005.

[31] R. Lang and K. Kobayashi. External optical feedback effects on semiconductor injection laser properties. *Quantum Electronics, IEEE Journal of*, 16:347 – 355, 1980.

[32] Steven H. Strogatz. *Nonlinear Dynamics And Chaos: With Applications To Physics, Biology, Chemistry, And Engineering.* Westview Press, 1 edition, 2000.

[33] J. Doyne Farmer. Chaotic attractors of an infinite-dimensional dynamical system. *Physica D: Nonlinear Phenomena*, 4:366 – 393, 1982.

[34] Valentin Flunkert. *Delayed Complex Systems and Applications to Lasers.* PhD thesis, Technische Universität Berlin, 2010.

[35] Giancarlo Benettin, Luigi Galgani, Antonio Giorgilli, and Jean-Marie Strelcyn. Lyapunov Characteristic Exponents for smooth dynamical systems and for hamiltonian systems; a method for computing all of them. Part 1: Theory. *Meccanica*, 15:9–20, 1980.

[36] John Guckenheimer and Philip Holmes. *Nonlinear Oscillations, Dynamical Systems, and Bifurcations of Vector Fields* . Springer, 1983.

[37] John Milnor. On the concept of attractor. *Comm. Math. Phys.*, 99:177–195, 1985.

[38] David Ruelle and Floris Takens. On the nature of turbulence. *Comm. Math. Phys.*, 20:167–192, 1971.

[39] J.Doyne Farmer, Edward Ott, and James A. Yorke. The dimension of chaotic attractors. *Physica D: Nonlinear Phenomena*, 7:153 – 180, 1983.

[40] Peter Grassberger and Itamar Procaccia. Measuring the strangeness of strange attractors. *Physica D: Nonlinear Phenomena*, 9:189 – 208, 1983.

[41] Peter Grassberger and Itamar Procaccia. Characterization of strange attractors. *Phys. Rev. Lett.*, 50:346–349, 1983.

[42] J. Kaplan and J. Yorke. Chaotic behavior of multidimensional difference equations. In H. O. Peitgen and H. O. Walther, editors, *Functional Differential Equations and Approximation of Fixed Points*. Springer, Heidelberg-New York, 1979.

[43] Paul Frederickson, James L. Kaplan, Ellen D. Yorke, and James A. Yorke. The liapunov dimension of strange attractors. *Journal of Differential Equations*, 49:185 – 207, 1983.

[44] P. Grassberger and I. Procaccia. Dimensions and entropies of strange attractors from a fluctuating dynamics approach. *Physica D: Nonlinear Phenomena*, 13:34 – 54, 1984.

[45] John Argyris, Gunter Faust, Maria Haase, and Rudolf Friedrich. *Die Erforschung des Chaos*. Springer, 2 edition, 2010.

[46] J. Kestler. Synchronisation chaotischer Bernoulli-Einheiten in einfachen Netzwerken mit zeitverzögerter Kopplung. Master's thesis, Universität Würzburg, 2007.

[47] Carl D. Meyer. *Matrix analysis and applied linear algebra*. Society for Industrial and Applied Mathematics, 2000.

[48] Einat Klein, Noam Gross, Michael Rosenbluh, Wolfgang Kinzel, Lev Khaykovich, and Ido Kanter. Stable isochronal synchronization of mutually coupled chaotic lasers. *Phys. Rev. E*, 73:066214, 2006.

[49] W. Kinzel, A. Englert, G. Reents, M. Zigzag, and I. Kanter. Synchronization of networks of chaotic units with time-delayed couplings. *Phys. Rev. E*, 79:056207, 2009.

[50] M. Zigzag, M. Butkovski, A. Englert, W. Kinzel, and I. Kanter. Zero-lag synchronization of chaotic units with time-delayed couplings. *EPL (Europhysics Letters)*, 85:60005, 2009.

[51] Meital Zigzag, Maria Butkovski, Anja Englert, Wolfgang Kinzel, and Ido Kanter. Zero-lag synchronization and multiple time delays in two coupled chaotic systems. *Phys. Rev. E*, 81:036215, 2010.

[52] A. Englert, W. Kinzel, Y. Aviad, M. Butkovski, I. Reidler, M. Zigzag, I. Kanter, and M. Rosenbluh. Zero lag synchronization of chaotic systems with time delayed couplings. *Phys. Rev. Lett.*, 104:114102, 2010.

[53] Louis M. Pecora and Thomas L. Carroll. Master stability functions for synchronized coupled systems. *Phys. Rev. Lett.*, 80:2109–2112, 1998.

[54] Mukeshwar Dhamala, Viktor K. Jirsa, and Mingzhou Ding. Enhancement of neural synchrony by time delay. *Phys. Rev. Lett.*, 92:074104, 2004.

[55] J. Sun, E. M. Bollt, and T. Nishikawa. Master stability functions for coupled nearly identical dynamical systems. *EPL (Europhysics Letters)*, 85:60011, 2009.

[56] Juan G. Restrepo, Edward Ott, and Brian R. Hunt. Spatial patterns of desynchronization bursts in networks. *Phys. Rev. E*, 69:066215, 2004.

[57] V. Flunkert, S. Yanchuk, T. Dahms, and E. Schöll. Synchronizing distant nodes: A universal classification of networks. *Phys. Rev. Lett.*, 105:254101, 2010.

[58] A. Englert, S. Heiligenthal, W. Kinzel, and I. Kanter. Synchronization of chaotic networks with time-delayed couplings: An analytic study. *Phys. Rev. E*, 83:046222, 2011.

[59] Sven Heiligenthal, Thomas Dahms, Serhiy Yanchuk, Thomas Jüngling, Valentin Flunkert, Ido Kanter, Eckehard Schöll, and Wolfgang Kinzel. Strong and weak chaos in nonlinear networks with time-delayed couplings. *Phys. Rev. Lett.*, 107:234102, 2011.

[60] A S Pikovsky and P Grassberger. Symmetry breaking bifurcation for coupled chaotic attractors. *Journal of Physics A: Mathematical and General*, 24:4587, 1991.

[61] Peter Ashwin, Jorge Buescu, and Ian Stewart. Bubbling of attractors and synchronisation of chaotic oscillators. *Physics Letters A*, 193:126 – 139, 1994.

[62] Shankar C. Venkataramani, Brian R. Hunt, Edward Ott, Daniel J. Gauthier, and Joshua C. Bienfang. Transitions to bubbling of chaotic systems. *Phys. Rev. Lett.*, 77:5361–5364, 1996.

[63] Shankar C. Venkataramani, Brian R. Hunt, and Edward Ott. Bubbling transition. *Phys. Rev. E*, 54:1346–1360, 1996.

[64] Yu. L. Maistrenko, V. L. Maistrenko, A. Popovich, and E. Mosekilde. Role of the absorbing area in chaotic synchronization. *Phys. Rev. Lett.*, 80:1638–1641, 1998.

[65] Michael G. Rosenblum, Arkady S. Pikovsky, and Jürgen Kurths. Phase synchronization of chaotic oscillators. *Phys. Rev. Lett.*, 76:1804–1807, 1996.

[66] Johannes Kestler, Wolfgang Kinzel, and Ido Kanter. Sublattice synchronization of chaotic networks with delayed couplings. *Phys. Rev. E*, 76:035202, 2007.

[67] Johannes Kestler, Evi Kopelowitz, Ido Kanter, and Wolfgang Kinzel. Patterns of chaos synchronization. *Phys. Rev. E*, 77:046209, 2008.

[68] S. Lepri, G. Giacomelli, A. Politi, and F. T. Arecchi. High-dimensional chaos in delayed dynamical systems. *Physica D: Nonlinear Phenomena*, 70:235 – 249, 1994.

[69] O. D'Huys, S. Zeeb, T. Jüngling, S. Yanchuk, and W. Kinzel. Synchronization and scaling properties of chaotic networks with multiple delays. *ArXiv e-prints*, 2013. Paper accepted for publication at EPL.

[70] Matthias Wolfrum and Serhiy Yanchuk. Eckhaus instability in systems with large delay. *Phys. Rev. Lett.*, 96:220201, 2006.

[71] Arturo C. Martí, Marcelo Ponce C., and Cristina Masoller. Chaotic maps coupled with random delays: Connectivity, topology, and network propensity for synchronization. *Physica A: Statistical Mechanics and its Applications*, 371:104 – 107, 2006.

[72] C. Masoller and A. C. Martí. Random delays and the synchronization of chaotic maps. *Phys. Rev. Lett.*, 94:134102, 2005.

[73] Fatihcan M. Atay. Distributed delays facilitate amplitude death of coupled oscillators. *Phys. Rev. Lett.*, 91:094101, 2003.

[74] M. Escalona-Morán, G. Paredes, and M. G. Cosenza. Complexity, information transfer and collective behavior in chaotic dynamical networks. *Int. J. App. Math. Stat.*, 26:58, 2012.

[75] Steffen Zeeb, Thomas Dahms, Valentin Flunkert, Eckehard Schöll, Ido Kanter, and Wolfgang Kinzel. Discontinuous attractor dimension at the synchronization transition of time-delayed chaotic systems. *Phys. Rev. E*, 87:042910, 2013.

[76] R. Hegger, H. Kantz, and T. Schreiber. Practical implementation of nonlinear time series methods: The TISEAN package. *CHAOS*, 9:413, 1999.

[77] Holger Kantz and Thomas Schreiber. *Nonlinear Time Series Analysis*. Cambridge University Press, 2 edition, 2005.

[78] J. F. Heagy, N. Platt, and S. M. Hammel. Characterization of on-off intermittency. *Phys. Rev. E*, 49(2):1140–1150, Feb 1994.

[79] J. F. Heagy, T. L. Carroll, and L. M. Pecora. Desynchronization by periodic orbits. *Phys. Rev. E*, 52:R1253–R1256, 1995.

[80] Steffen Zeeb, Johannes Kestler, Ido Kanter, and Wolfgang Kinzel. Chaos pass filter: Linear response of synchronized chaotic systems. *Phys. Rev. E*, 87:042923, 2013.

[81] L. Kocarev and U. Parlitz. General approach for chaotic synchronization with applications to communication. *Phys. Rev. Lett.*, 74:5028–5031, 1995.

[82] A. Murakami and K. A. Shore. Chaos-pass filtering in injection-locked semiconductor lasers. *Phys. Rev. A*, 72:053810, 2005.

[83] I. Fischer, Y. Liu, and P. Davis. Synchronization of chaotic semiconductor laser dynamics on subnanosecond time scales and its potential for chaos communication. *Phys. Rev. A*, 62:011801, 2000.

[84] Bruno Cessac and Jacques-Alexandre Sepulchre. Linear response, susceptibility and resonances in chaotic toy models. *Physica D*, 225:13–28, 2007.

[85] Hiroya Nakao. Asymptotic power law of moments in a random multiplicative process with weak additive noise. *Phys. Rev. E*, 58:1591–1600, 1998.

[86] Michael Rosenbluh, Yaara Aviad, Elad Cohen, Lev Khaykovich, Wolfgang Kinzel, Evi Kopelowitz, Pinhas Yoskovits, and Ido Kanter. Spiking optical patterns and synchronization. *Phys. Rev. E*, 76:046207, 2007.

[87] Ido Kanter, Noam Gross, Einat Klein, Evi Kopelowitz, Pinhas Yoskovits, Lev Khaykovich, Wolfgang Kinzel, and Michael Rosenbluh. Synchronization of mutually coupled chaotic lasers in the presence of a shutter. *Phys. Rev. Lett.*, 98(15):154101, 2007.

[88] Gabriel Pérez and Hilda A. Cerdeira. Extracting messages masked by chaos. *Phys. Rev. Lett.*, 74:1970–1973, 1995.

[89] U. Parlitz. Estimating model parameters from time series by autosynchronization. *Phys. Rev. Lett.*, 76:1232–1235, 1996.

[90] John B. Geddes, Kevin M. Short, and Kelly Black. Extraction of signals from chaotic laser data. *Phys. Rev. Lett.*, 83:5389–5392, 1999.

[91] Rainer Hegger, Martin J. Bünner, Holger Kantz, and Antonino Giaquinta. Identifying and modeling delay feedback systems. *Phys. Rev. Lett.*, 81:558–561, 1998.

[92] Kevin M. Short and Andrew T. Parker. Unmasking a hyperchaotic communication scheme. *Phys. Rev. E*, 58:1159–1162, 1998.

[93] Changsong Zhou and C.-H. Lai. Extracting messages masked by chaotic signals of time-delay systems. *Phys. Rev. E*, 60:320–323, 1999.

[94] E. Klein, , R. Mislovaty, I. Kanter, and W. Kinzel. Public-channel cryptography using chaos synchronization. *Phys. Rev. E*, 72:016214, 2005.

[95] Einat Klein, Noam Gross, Evi Kopelowitz, Michael Rosenbluh, Lev Khaykovich, Wolfgang Kinzel, and Ido Kanter. Public-channel cryptography based on mutual chaos pass filters. *Phys. Rev. E*, 74:046201, 2006.

[96] I. Kanter, E. Kopelowitz, J. Kestler, and W. Kinzel. Chaos synchronization with dynamic filters: Two-way is better than one-way. *Europhys. Lett.*, 83:50005, 2008.

[97] Ido Kanter, Evi Kopelowitz, and Wolfgang Kinzel. Public channel cryptography: Chaos synchronization and hilbert's tenth problem. *Phys. Rev. Lett.*, 101:084102, 2008.

[98] W. Kinzel, A. Englert, and I. Kanter. On chaos synchronization and secure communication. *Philosophical Transactions of the Royal Society A: Mathematical,Physical and Engineering Sciences*, 368:379–389, 2010.

[99] Didier Sornette. Multiplicative processes and power laws. *Phys. Rev. E*, 57:4811–4813, 1998.

[100] Yoshiki Kuramoto and Hiroya Nakao. Scaling properties in large assemblies of simple dynamical units driven by long-wave random forcing. *Phys. Rev. Lett.*, 78:4039–4042, 1997.

[101] V. Flunkert, O. D'Huys, J. Danckaert, I. Fischer, and E. Schöll. Bubbling in delay-coupled lasers. *Phys. Rev. E*, 79:065201, 2009.

[102] Liat Ein-Dor and Ido Kanter. Confidence in prediction by neural networks. *Phys. Rev. E*, 60:799–802, 1999.

[103] M.F. Barnsley. *Fractals Everywhere*. Academic Press, San Diego, 1988.

[104] T. Heil, I. Fischer, W. Elsässer, J. Mulet, and C. R. Mirasso. Chaos synchronization and spontaneous symmetry-breaking in symmetrically delay-coupled semiconductor lasers. *Phys. Rev. Lett.*, 86:795–798, 2001.

[105] Daniel J. Gauthier and Joshua C. Bienfang. Intermittent loss of synchronization in coupled chaotic oscillators: Toward a new criterion for high-quality synchronization. *Phys. Rev. Lett.*, 77:1751–1754, 1996.

[106] I. Kanter, M. Zigzag, A. Englert, F. Geissler, and W. Kinzel. Synchronization of unidirectional time delay chaotic networks and the greatest common divisor. *EPL (Europhysics Letters)*, 93:60003, 2011.

[107] H. L. D. de Souza Cavalcante, M. Oria, D. Sornette, and D. J. Gauthier. Predictability and control of extreme events in complex systems. *ArXiv e-prints*, 2013.

Acronyms

KY Kaplan Yorke

LE Lyapunov exponent

SM synchronization manifold

BER bit error rate